Alma Mater Studiorum - Università di Bologna

DOTTORATO DI RICERCA IN INGEGNERIA CIVILE, CHIMICA, AMBIENTALE E DEI MATERIALI

Ciclo XXVIII

Settore Concorsuale di afferenza: 08/A4
Settore Scientifico disciplinare: ICAR/06

REMOTE SENSING TECHNIQUES
FOR CHANGE DETECTION ANALYSIS
IN ARID AND SEMI-ARID AREAS

Candidata: **ANNA ZANCHETTA**

Coordinatore: **VITTUARI LUCA**   relatori: **BITELLI GABRIELE**
                                                  BONOLI ALESSANDRA

Esame finale anno 2017

Homo sum, humani nihil a me alienum puto

To Yoav

Contents

Introduction

Desertification constitutes a natural hazard that threatens human livelihood, wildlife and vegetation conditions worldwide. Arid and semi-arid areas are the most likely to undergo processes of desertification, and it is a concern of the international community to control, monitor and prevent such a phenomenon [UNCCD, 1994].

Water scarcity is a fundamental challenge to sustainable development in arid and semi-arid regions where renewable freshwater resources at the national level are insufficient to satisfy growing needs. As a mainly arid region, the Middle East and North Africa (MENA) is particularly vulnerable to climate-induced impacts on water resources, but still the promotion of a responsible water management remains a low priority for political leaderships [Sowers et al., 2010]. This factor contributes to exacerbate the political unrest and affects the economic development of the region, challenged by growing populations [Gleick, 2014; Sowers et al., 2010; UNESCO, 2012]. Worldwide, water use has been growing at more than twice the rate of population increase in the last century, with future scenarios foreseeing 1.8 billion people living in countries or regions with absolute water scarcity by 2025 *. In this scenario, MENA states are particularly hit, for the ongoing population growth rate and climate conditions couple with a water stressed situation, characteristic of the region [World Bank, 2007].

Shared water resources provide an essential source of freshwater, especially in water-scarce regions [UN-ESCWA and BGR, 2013]. In MENA region most of the surface groundwater resources are shared among neighboring countries, but not always the water withdrawal and management are subject to or respect international agreements between riparian countries, as it is the case of the Jordan River and the Tigris-Euphrates Basin. In this last case the situation emerged with evidence in the last decades with a disputed control over the watershed basin of the river Euphrates, shared among Turkey, Syria and Iraq [Beaumont, 1978].

The aim of the reasearch is to investigate Remote Sensing (RS) techniques for desertifi-

---

*http://www.unwater.org/publications/publications-detail/en/c/204294

cation studies, with a special focus on the Middle East region. RS is an efficient tool for environmental studies on wide areas of the Earth surface, allowing fast and reproducible analysis on regional and continental scales. This is a considerable advantage of RS over other techniques, given the spatial extension of a phenomenon such as desertification, both in spatial and temporal terms [Albalawi and Kumar, 2013; Bayarjargal et al., 2006]. The reproducibility of the analysis methods allows a constant monitoring of a region, giving the possibility of predictability of events and measures of prevention of the risk.

The task of detecting the surface change in RS is referred to as *change detection* analysis, often paired with Land Use and Land Cover Change (LULCC) analysis. LULCC detection techniques have been proven effective for the investigation of desert environments on long temporal scales [Dawelbait and Morari, 2011; Lin et al., 2011; Mouat et al., 1997; Palmer and van Rooyen, 1998].

For this research two mehods in particular have been examined and further implemented: Change Vector Analysis (CVA), applied to the Tasselled Cap Transform (TCT) outputs, and the Maximum Autocorrelation Factor (MAF) transformation of the Multivariate Alteration Detector (MAD) components (MAD/MAF).

While CVA has been used in LULCC studies both in vegetated and desert areas [Bayarjargal et al., 2006; Malila and Lafayette, 1980; Palmer and van Rooyen, 1998], TCT has been developed for forest areas [Ivits et al., 2008; Kauth and Thomas, 1976; Yarbrough et al., 2012]. The use of CVA on TCT coefficients suitable for drylands studies must be therefore investigated. In this research this issue will be addressed through the calculation of new TCT coefficients adapted to desert areas, for Landsat and SPOT satellites.

In the current research the usage of MAD/MAF in desert applications is also examined. A joint MAF/MAD analysis provides a statistically rigorous way to accurately determine the spatially coherent patterns of major change on the surface[Nielsen et al., 1998]. However the interpretation of the outputs of this technique is not univocal, therefore its application in combination with CVA is proposed and investigated, in order to find if their combined usage can overcome the downsides of both.

The thesis starts with the description of the phenomenon of desertification, its causes and impacts, discussing in particular the water situation in the Middle East region. Two case studies are here described: Al Azraq Oasis in Jordan, as a case of water depletion in arid areas, and the transboundary region of Jezira, at the border between Syria and Turkey, as a case of shared water management.

The second chapter lists and describes some RS techniques for change detection studies, focusing on the CVA, TCT and MAD/MAF techniques. An overview of the materials used

for the research is thus given in Chapter three, with the description of the satellites used for the images supply and the software employed for the analysis, part of Geographical Free and Open Source Software (GFOSS).

The fourth chapter outlines the research development, starting from the calculation of new desert-adapted TCT coefficients and the description of a new module for implementing CVA in a GFOSS software. The combination of CVA and TCT is then illustrated and validated in two selected areas in the Middle East.

Finally, Chapter five addresses the application of LULCC techniques to the two case studies. CVA is tested in Al Azraq Oasis (both in a short and a long term analysis), then the new combined technique is applied to compare the cross-border surface change in the Jezira region in a thirty years analysis.

Chapter 1

Desertification and Middle East

The present chapter addresses the causes and impacts of desertification and describes two case studies, which have been investigated for water related issues in arid and semi-arid areas in the Middle east region.

Desertification is a process which operates principally in arid, semi-arid (together *drylands*) and sub-humid environments, involving excessive pressure of human use, changes in land use or changes in natural processes. It is associated with long-term changes in ecosystems function and results in reduced productivity, biodiversity and diminished economic viability [Mouat et al., 1997].

Water scarcity and desertification constitute a prominent issue in the Middle East region, where weather conditions and climate variations can affect a prone to stress environment [Sowers et al., 2010]. In the present research, RS capability to detect the change on the surface in this mostly arid to semi-arid region has been assessed through the analysis of two case, one in Jordan and one along the Syrian-Turkish border.

The first case, Al Azraq Oasis, in Jordan, constitutes an interesting subject of study due to the changes occurred to the Oasis in the last decades. In the early 1990s the springs underwent a complete drying out due to groundwater over-exploitation, and this make of it an exceptional case to test techniques for monitoring the desertification in the drylands. A second case study is along the Sirian-Turkish border, on the eastern side of both countries, the so called Jezira region. The relevance of this case study is given by the impressive difference visually recognizable along the border line by satellite pictures. This constitutes an outstanding circumstance to study the impact of droughts and political decisions on land cover development, in a context where the absence of international agreements exacerbates the situation. Political choices and human intervention, in fact, can play a considerable role in the water availability and in desertification mitigation, both with positive and negative

impacts.

1.1   Desertification

The phenomenon of desertification has been identified as a global environmental issue since the early 1920s [Albalawi and Kumar, 2013], and has received widespread attention in the 70s, leading to the creation of the United Nations Conference on Desertification (UNCOD) in Nairobi in 1977 [Karnieli and Dall'Olmo, 2003], mainly as a result of the impact of an extended drought in the West African Sahel in that decade [Glantz and Orlovsky, 1983]. In the XX century international community's concern about desertification led to the establishment, in 1994, of the the United Nations Convention to Combat Desertification (UNCCD), signed in Paris, France. Its adoption was a direct consequence of the recommendations from the Agenda 21 action plan ("21" refers to the 21st century), resulted from the Rio Earth Summit Conference, officially United Nations Conference on Environment and Development, held in Rio de Janeiro, Brazil, in 1992. Agenda 21 is an action agenda for the UN and individual governments addressing common issues such as fighting poverty and environmental concerns like climate change, biodiversity, water scarcity, alternative sources of energy, resilience, sustainability.

The UNCCD is the only internationally legally binding framework set up to address the problem of desertification. The Convention's 195 parties work together to improve the living conditions for people in the drylands, to maintain and restore land and soil productivity, and to mitigate the effects of drought [UNCCD, 1994].

Several definitions can be found about the desertification phenomenon [Albalawi and Kumar, 2013; Glantz and Orlovsky, 1983; Mouat et al., 1997], however UNCCD foundation document defines it as "land degradation in arid, semi-arid and dry sub-humid areas resulting from various factors, including climatic variations and human activities", whereas *land degradation*'s definition involves the loss of biological or economic productivity and complexity in rainfed croplands, pastures, and woodlands in arid, semi-arid and dry sub-humid areas [UNCCD, 1994]. Referring to the climate classification map, based on the work of Wladimir Köppen dating back to 1900 (see Fig. 1.1), arid areas are comprised in the climate type B, which includes desert and steppe climates, separated in hot and cold [Peel et al., 2007]. According to this classification, globally the dominant climate class by land area is Arid (B, 30.2%), while Arid desert hot climate constitute the most common individual climate type by land area (BWh, 14.2%), followed by Tropical Savanah (classified as Aw, 11.5%).
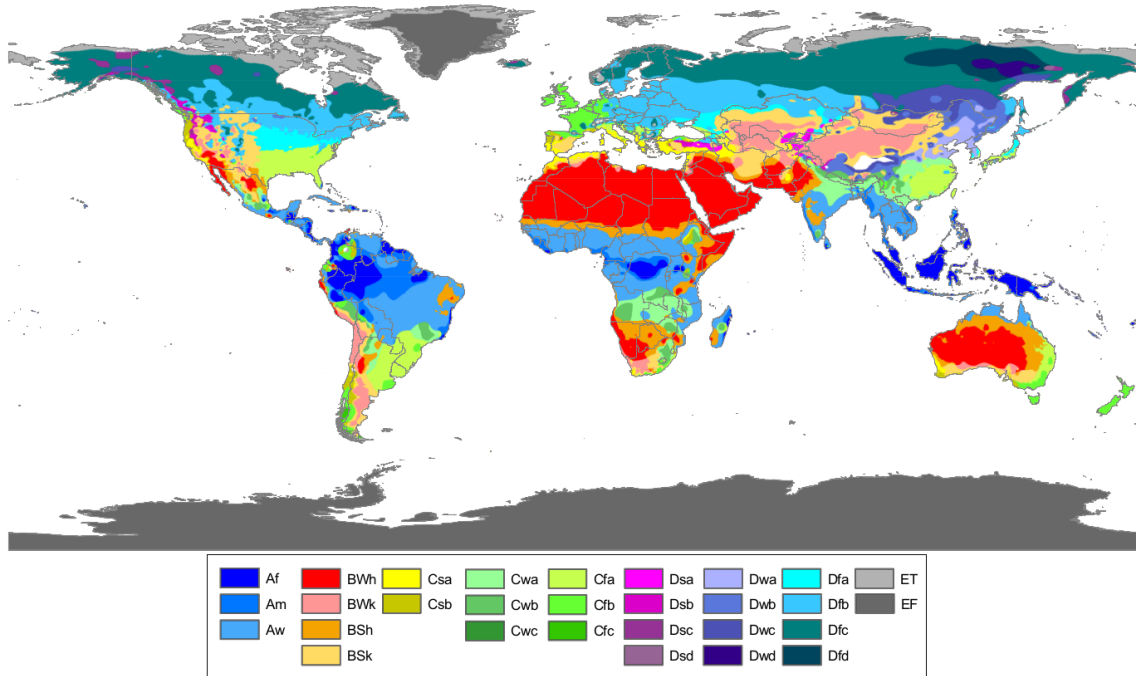
Figure 1.1: Köppen-Geiger climate type map of the World. The Arid class is denoted by the letter B. In red Arid desert hot climate (BWh). Source: Peel et al. [2007].

Desertification processes are well known but not fully understood [Albalawi and Kumar, 2013]. In many cases it's not just one single process but a combination of processes that can lead to desertification, and their nature is both of human and natural induced origin. The processes include:

(i) soil erosion caused by wind and/or water;

(ii) deterioration of the physical, chemical and biological or economic properties of soil;

(iii) long-term loss of natural vegetation [UNCCD, 1994].

Desertification is due mainly to climate variability, e.g. low rainfall and high temperatures, drought, and water or wind erosion, and unsustainable human activities, among these: overcultivation, overgrazing, deforestation, and poor irrigation practices [Albalawi and Kumar, 2013; UNCCD, 2008]. It occurs in all continents (except Antartide) affecting the livelihoods of millions of people, including a large proportion of the poor in drylands with over 250 million people directly affected by desertification, and one billion at risk [UNCCD, 2008]. Drylands occupy about 41% of the Earth's surface and 70% of these regions (excluding hyper-arid deserts), or some 3,600 million hectares, are degraded [UNCCD, 2008].

Desertification has environmental consequences which can seriuosly affect the economic and social status of a country, especially those who depend on agriculture, threatening the population of affected developing countries worldwide [Albalawi and Kumar, 2013; Sardinha, 2008]. Consequences of desertification processes hit both population and the environment, with triggers that feed one each other. Among these: desertification reduces the land's resilience to natural climate variability, soil becomes less productive, vegetation becomes damaged and food production is undermined, contributing to famine. It's clear then that desertification has enormous social costs and can become a huge source of depletion on a country's economic resources [UNCCD, 2008].

The aforesaid makes evident how it's of international importance to find common agreements and practices in order to preserve productive lands, mitigate desertification impacts and rehabilitate degraded lands. This series of activities is aimed at an integrated approach to sustainable development in arid, semi-arid and dry sub-humid areas, collectively referred to as "combating desertification" by UNCCD [1994].

Among activities to monitor and prevent desertification processes, drought mitigation and forecasting constitute a major step. By UNCCD definition, drought "means the naturally occurring phenomenon that exists when precipitation has been significantly below normal recorded levels, causing serious hydrological imbalances that adversely affect land resource production systems" [UNCCD, 1994]. As by [Mc Nab, A.L., Karl, T.R., 1991], drought occurs when significant precipitation is absent "for a period which is long enough to cause moisture deficits in the soil due to evapotranspiration and decreases on stream flow, thereby disrupting the normal biological and human activities". Despite being a naturally recurrent climate process, drought's nature is quite erratic and this characteristic makes it challenging to predict and mitigate.

Drought is often associated with land degradation [Albalawi and Kumar, 2013], and it has been defined specifically by the RS community as a period of abnormally dry weather, which results in a change in vegetation cover [Bayarjargal et al., 2006]. RS allows to obtain fast easily readable maps, over wide temporal and spatial scales, of the change on the Earth surface, among which several vegetation characteristics such as plant available moisture, land cover type and condition. This capability provides the possibility to monitor and assess the level of vegetation stress as an indicator of drought, making of RS an effective tool for combating desertification and for droughts assessment [Albalawi and Kumar, 2013; Karnieli and Dall'Olmo, 2003; Shafie et al., 2012].

In the present research in particular the drought occurred in the Middle East region in the period 2006-2010 will be investigated. During this time, the whole Fertile Crescent experi-

enced "the worst long-term period drought since agricultural civilizations began millennia ago" [Gleick, 2014], or at least from the beginning of the XX century, as by the drought index used by Kelley et al. [2015]. The latest show that Syria and the whole Fertile Crescent region were hit in the late 50s, 80s and 90s by episodes of multi-year droughts, defined as three or more consecutive years of rainfall below the century long normal. The Middle East region is particularly vulnerable to adverse climatic conditions, like periods of drought and dry conditions, because it already suffers from extreme climate variability and water scarcity [UNESCO, 2012].

1.2 Water in the the Middle East

The "Middle East" is variously intended as the region centered in Western Asia facing the Mediterranean Sea, the Red Sea and the Persian Gulf. Definitions vary from a narrower point of view as basically the region known in ancient times as the Fertile Crescent, constituted by the Tigris and Euphrates watersheds of Mesopotamia to the East and extending to the Mediterranean shore in the Palestinian region. A wider point of view inludes the area from the present states of Iran to the East, to the Arabian Peninsula to the South and to modern Egypt, comprising the Nile river flow to the Western Side, up to modern Turkey in the North. As such it is commonly referred to as Middle East and North Africa (MENA) region, acception that includes all the African continent states that overlook the Mediterranean Sea. The Middle East is a transcontinental region, lying at a juncture, not only physical, that comprises different populations, languages and religions, united by a common territorial belonging and by an interlaced millennia-long history, that saw in these lands the "cradle of civilization".

Climate in the MENA region is characterized by a variation from hot dry, hyper-arid areas in the deserts to dry sub-humid and humid areas, mainly along the Mediterranean coast [World Bank, 2007], with a predominace of arid and semi-arid areas and an average annual rainfall of about 250 mm; however vast areas of the MENA countries are hyperarid, with typical rainfall of 5 mm/year [Brooks, 2007]. The climatic variation reflects the geographical variation, from costal plaines and slopes, to mountains and rift vallyes with the lowest land elevation on Earth [Brooks, 2007; Pallant, 2007].

Historically the Middle East has been subject to the domination of different empires and colonial control up to the XX century, and the recent history is still affected by the aftermath of the geographical division occurred after the late 40s. After the First War World most of the region, that was comprised in the Ottoman Empire, underwent the control of

the French domain (to the West, Syria and Lebanon) and of the British Mandate (to the East, from Palestine to Saudi Arabia), that ruled over the region until the Second World War. In recent times, the interest of external powers on the region is mainly due to the oil and gas resources, that are abundant all over the area. But, quoting Richard Cowen *, "the most important resource in the Middle East may be water, not oil"; in fact water resources constitute by far a key point in this region: the only two countries that are self-sufficient are Iran and Turkey, while the others depend on river water flows or on scarce groundwater resources that are mainly from transboundary origin [same source].

For centuries the communities living in this region shared the water of rivers, springs and wadis, where traditional water management and irrigation schemes sustained different communal needs [UN-ESCWA and BGR, 2013] and water has been a main limiting factor in the development, as well as the source of many of its conflicts [Brooks, 2007]. The problem of shared water resources has characterized the political instability and disputes in the area for centuries [Beaumont, 1978; Gleick, 2014]. Relating to the surface sources, international rivers saw basin disputes over the division of the waters between neighboring states, that lead eventually to amicable agreements betwen Egypt and Sudan over the river Nile (in 1929 and 1959), as well as between Israel and the three neighboring countries (Lebanon, Syria, Jordan), with more tense relations, over the river Jordan. In the Euphrates basin, instead, the disputes have only arisen in the 1960s, for increasing development needs of Turkey and Syria, and did not arrive to a final agreement among the parties [Beaumont, 1978; UN-ESCWA and BGR, 2013].

Surface water resources come mainly from the rivers' contribute, with Nile and Tigris-Euphrates being the largest suppliers. Traditional and low-capital forms of water management includes rainwater harvesting systems, desert dams, groundwater aquifers abstraction, runoff. More modern, centralized and high-cost techniques are desalination of sea and brackish water, imports of water and interbasin transfers [Brooks, 2007], even though indirect or 'virtual' water [Shuval, 2007] contribution to the total avaialbility is not marginal (it has been calculated by Allan [2003] to have a flow equal to the annual Nile flow).

Water availability in the region varies for different countries from highly water stressed (like Jordan, 200 m^3/ capita/ year) to less stressed countries (like Iraq, more than 4000 m^3/ capita/ year) [Sowers et al., 2010]. Overall the MENA region is considered "scarce" in water availability, with scarcity meaning less than 1000 m^3 per capita per year (water security being considered for values above 1700 m^3, water stress between 1700 m^3 and 1000 m^3/ capita/ year) [World Bank, 2007], making it one of the most water-scarce regiones in

---

*http://mygeologypage.ucdavis.edu/cowen/ GEL115/115CHXXMideastwater.html

the world, with one of the highest population growth rate [De Châtel, 2014b; UN-ESCWA and BGR, 2013].

The raise in population, assuming no increment in total available water resources, implies less water avaialble per capita, with an expected rate in the range of 30 to 70% (average of 42%) by 2025 [Sowers et al., 2010]. The population growth has seen in these countries an average increase by 43% over the past two decades, with over 55% of the total population living in urban areas and trends of urban migration in most regions (including Egypt, Lebanon, Morocco, The Syrian Arab Republic and Tunisia) [UNESCO, 2012]. The migration is mainly attributed to reduced incomes and opportunities of employment in the agricultural sector, with a consequent expansion of industrial and service sectors, and impacts on the water demand, supply and sanitation [UN-ESCWA and BGR, 2013].

The World Bank's estimates of the effects of water scarcity on GDP for 2050, see for the MENA region a growth rate decline by as much as 6% of GDP by 2050 as a result of water-related losses in agriculture, health, income, and property, both in a bad-water-management policies scenario and in a good-policies scenario, with MENA being the only region in the world where efficient water policies are not predicted to make a change [World Bank, 2016].

As by Brooks [2007], water stress in the region arises from three interacting issues: quantity, since the demand exceeds the natural recharge rates [Gleick, 2014]; quality , which is affected by salinization [Sowers et al., 2010] and human induced pollution; equity, since most of freshwater resources are shared among neighbouring countries. In fact after the creation of the modern states, mostly during the 20th century, the rivers and many aquifer systems happened to be across the borders, making international cooperation or conflicts a necessity [Pallant, 2007].

Agriculture accounts for most of the water use in the MENA countries [Allan, 2002; UN-ESCWA and BGR, 2013], with an average of more than 70% of share on water demand [UNESCO, 2012], however the decline in agricultural productivity, due to climatic conditions and water management, is foreseen to decline of 23% by 2080 [UNESCO, 2012], with implicit need of food import, in particular cereals [Allan, 2002].

Agricultural production started flourishing from the 1960s thanks to the introduction of groundwater abstraction systems [UN-ESCWA and BGR, 2013], by increasingly cheaper and technologically advanced fuelled pumps [De Châtel, 2014b; Gleick, 2014], which resulted in intensive exploitation of groundwater resources. Several governments then in the 1980s and 1990s implemented a politic of liberalization of the agricultural sector and withdrew from a series of incentives and economical subsidies as measure to manage irri-

gation demand [Sowers et al., 2010]. This situation contributed to develop an uncontrolled and illegal water abstraction trend by the private sector, that eventually lead in modern times to consequences on the rivers flow regime and the groundwater levels [De Châtel, 2014b], with withdrawals that have tripled over the past fifty years and, in some areas, consistently exceed natural recharge rates [Gleick, 2014]. Overpumping and the flow of other saline sources are a major a cause of seawater intrusion, eventually affecting agricultural productivity due to deteriorating water quality of the groundwater aquifers [Sowers et al., 2010; UN-ESCWA and BGR, 2013]. Water quality deterioration arises also from raw sewage and uncontrolled agricultural run-off disposal, of chemical fertilizers and other pollutants, directly on the water system [De Châtel, 2014b].

Different governments implemented several experiments for improving water management, promoting public-private partnerships, user associations, and privatization of water services, in cooperation with international institutions, trying to promote an integrated water resource management [Sowers et al., 2010]. Still the water management in many countries is inadequate and can foster political unrest, as it's the case of Syria in recent years [De Châtel, 2014b] and "in practice, MENA governments continue to focus most of their resources on large-scale supply side projects, increasingly tapping fossil groundwater aquifers and building desalination plants. [...] Water resource planning in the MENA does not adequately address issues of equity in water access, linkages to population growth, or a more inclusionary role for political mobilization around resource access" [Sowers et al., 2010].

1.3   Al Azraq Oasis (Jordan), a case of groundwater exploitation

The changes occurred at Al Azraq Oasis in the last three decades are a good example of how human behavior can threaten the existence of a desert ecosystem and contribute to desertification processes, phenomenon which wetlands in arid areas are particularly vulnerable to. Understanding the evolution of desertification has a huge relevance in a country like Jordan, with a water supply of 145 m^3/person/year putting it high in the list of worldwide water scarcity countries [Al-Bakri et al., 2013; Al Eisawi, 2005; Edwards et al., 1999; UNICEF, 2014; WAJ, 2007; WHO, 2015] and poses a question on the sustainability of a society in a growing demand regime. The amount of water available per capita is in fact predicted to diminish down to 90 m^3/person/year in 2025 (personal communication), and this prediction would probably worsen if the number of refugees arriving from neighbouring Arab countries keeps on increasing [UNHCR, 2015].

Azraq Oasis is located in Jordan, 80 km east of the capital Amman approximately at coordinates 32°N and 37°S. It lies at the bottom of a relatively shallow natural depression at around 500 m of altitude, which constitutes the northern part of Wadi Sirhan Depression, a huge hydrological system covering great part of central Northern Saudi Arabia desert [Ramsar Convention, 1990a; UN-ESCWA and BGR, 2013].

The groundwater system is rather complex and is part of a greater aquifer system that extends from south-western Syria to Saudi Arabia, consisting mainly of three aquifers, one on top of the other. The upper one, called Basalt Aquifer, has been the most exploited one, and is also the aquifer from which the Oasis' springs originated. The superficial catchment area of this aquifer is a huge basin called the Azraq-Dhuleil Basin, that extends almost longitudinally, from the south-eastern side of Jebel Al-Arab (or Jebel Al-Druze, 1800 m high) mountain in Syria, to the north-eastern desert of Jordan [Cordova et al., 2013; Dottridge and Abu Jaber, 1999; El-Naqa et al., 2007]. The Basin area is considered predominantly arid, with annual precipitation ranging from less than 50 mm in the South-Eastern depression to more than 300 mm in the Northern part, in proximity of the most elevated point of the Basin [Al-Kharabsheh, 2000; UN-ESCWA and BGR, 2013].

Fig. 1.2 shows the position of Azraq in Jordan with the Azraq-Duhleil basin border and a Landsat look-like image of 25/02/2015 centered in the study area (in yellow), where the
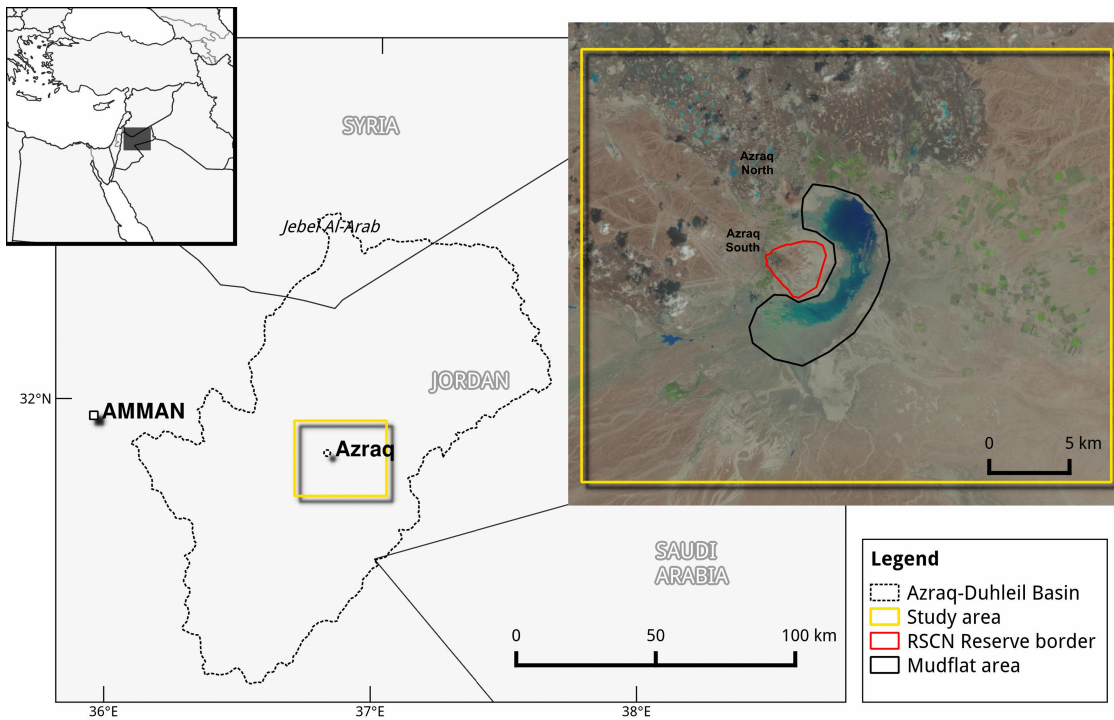
Figure 1.2: Location of Al Azraq Oasis in Jordan and the Middle East.

mudflat (shallow flooded) area and the Royal Society for Conservation of Nature (RSCN) Reserve border are also shown (see details in Section 5.1).

Al Azraq Oasis owes its name to the particularly light blue color of its water. The presence of pools of fresh water made Azraq a highly relevant spot in the Jordan Eastern desert: the first settlements in the area date back to the Middle Paleolithic era and are testified by the presence of an ancient Castle, a 13th century Ayyubid dinasty fortress built on some Roman ruins [Cordova et al., 2013; Ramsar Convention, 1998]. Beside the human colonization, Azraq represents a strategically important area for local fauna and migratory birds, stopping on their way from East Asia, Africa and Europe.

The existence of this historically important site is now at high risk, since in the 90s the Oasis went through a drastic drying up of the natural springs that were then releasing up to 16 Million Cubic Metres (MCM) of water a year [Dottridge and Abu Jaber, 1999; UN-ESCWA and BGR, 2013].

The main reason for the depletion of the water level in the Oasis is connected with human abstraction from the groundwater basin for domestic and rural use, especially after the so called 'green revolution' carried out by the Jordanian Government in the 80s [Demilecamps, 2010; IUCN, 2010; National Research Council, 1999]. The springs that supported the Oasis in fact were the natural discharge of the Azraq-Dhuleil Basin, which today is one of the biggest sources of potable water for the capital Amman (25%, in a country where groundwater resources make up 57% of total supply) [Mesnil and Habjoka, 2012]. The easily reachable water bed, in some points just a few meters under the soil level, allowed the exploitation of water resources by farmers that found in Azraq an easy and fast way of moneymaking, especially since at first the digging was not regulated nor monitored. Subsequently and still currently the illegal digging is flourishing and not completely under control. Beside the rural use, which accounts for up to two thirds of the total abstraction, the drawing of water for domestic purpose by the Water Authority of Jordan [WAJ, 2007] constitutes the second source of water exploitation [Demilecamps, 2010].

Fig. 1.3 shows how the estimated yearly abstraction grew from few MCM in the 80s up to the current 60 MCM [IUCN, 2010], from a basin for which the calculated safe yield is between 20 and 25 MCM [Al-Kharabsheh, 2000; Ramsar Convention, 1998].

Besides the lowering of the water bed, the groundwater conditions are also experiencing a general deterioration, mainly alteration in the groundwater salinity as shown by recent studies [El-Naqa et al., 2007; Goode et al., 2013]. The persistence of the present conditions will unlikely allow reversing the direction of the change, with a big loss in terms of desert biodiversity and cultural and aesthetic values [Dottridge and Abu Jaber, 1999; National

Research Council, 1999].
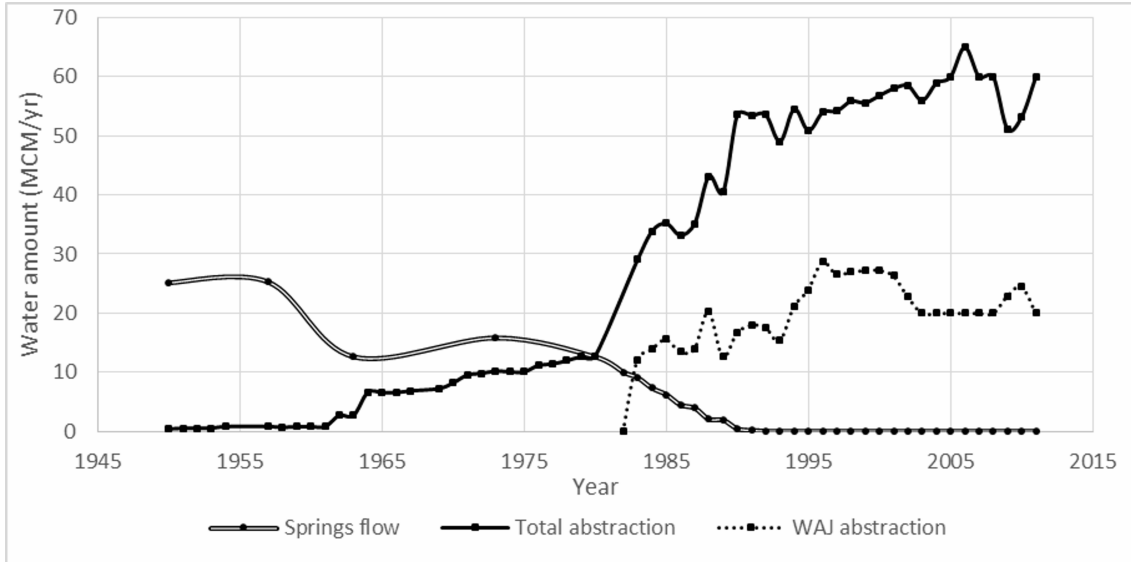
Figure 1.3: Springs flow and water abstraction from the Azraq–Dhuleil Basin since 1950, adapted from Dottridge and Abu Jaber [1999] and implemented. Source: based on data from the WAJ [2007] and Bajjali and Al-Hadidi [2005]; El-Naqa et al. [2007]; IUCN [2010]; Mesnil and Habjoka [2012].

1.4 The Jezira region along the Syrian-Turskish border, a case of transboundary water management

The Euphrates River originates in the mountains of Southeastern Turkey, in the vicinity of Lake Van, then flows through Syria and Iraq merging with the Tigris River at the confluence of the Shatt al Arab, the latest part of the river course that flows into the Persian Gulf (see Fig. 1.4). The combined Tigris-Euphrates and Shatt Al Arab watershed basin is the largest surface water resource in Western Asia, of which Euphrates constitutes the biggest contributor, covering about 440,000 km^2, 47% of which in Iraq, 28% in Turkey, 22% in Syria, and some minor percentages in Jordan and Saudi Arabia (see Fig. 1.4).

Three major tributaries flow into the Euphrates in Syria: the Sajur, the Balikh and the Khabour Rivers. South of the Khabour, there are no other tributaries to the Euphrates in Syria or Iraq. All of them originate both from the Turkish mountains North of the border with Syria and from the groundwater sources and karstic springs (Ain Al-Arus on the west and Ras Al Ayn on the East) in the Jezira region in Syria [UN-ESCWA and BGR, 2013], subject of the present study. Jezira is the Arab word for 'island' and the name comes from the position of this plain, between the Tigris on the East and Euphrates River to the West,
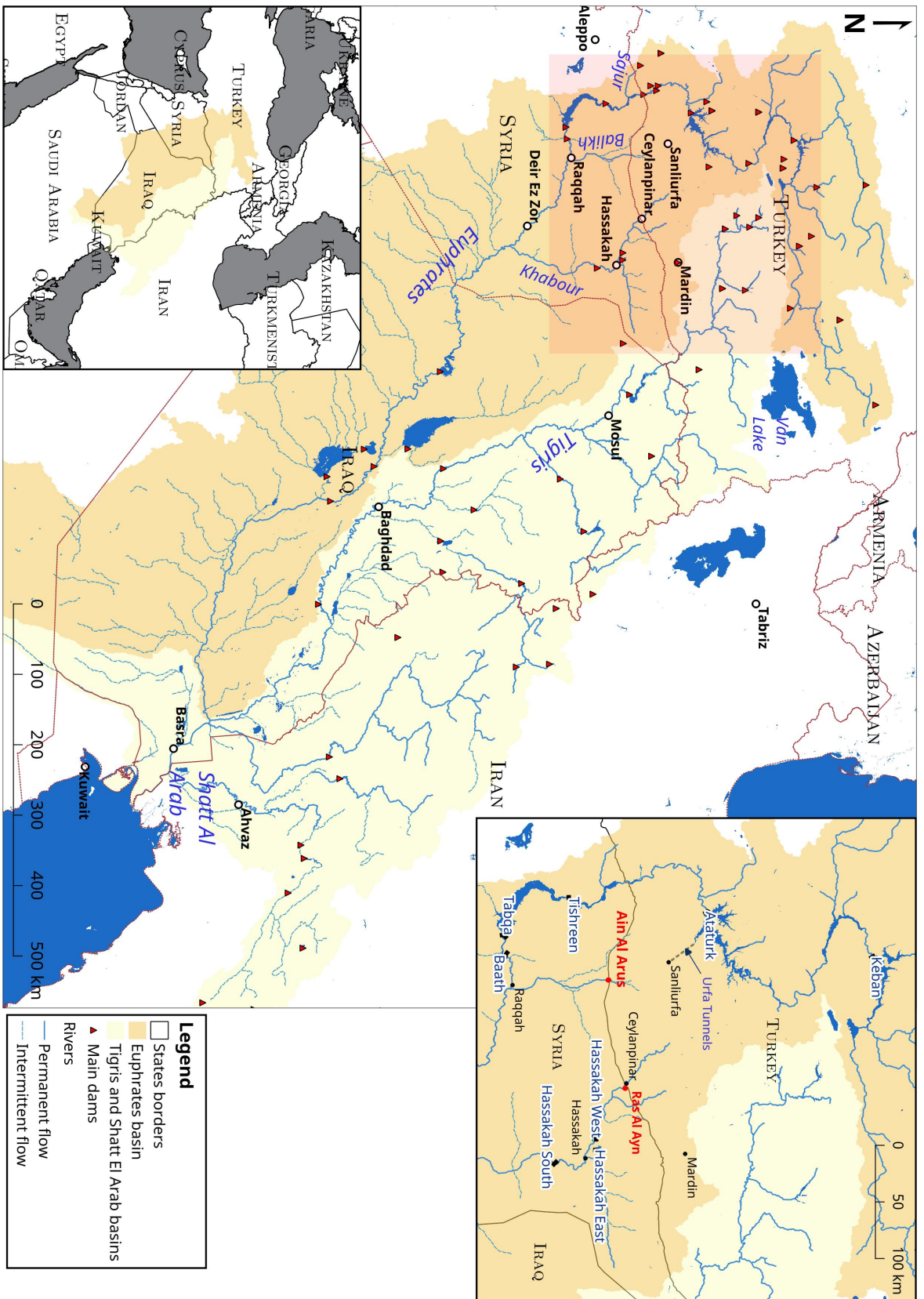
Figure 1.4: Position of the Euphrates-Tigris Basin in the Middle East region (left insert); geographical boundaries of the Euphrates-Tigris Basin with main cities and main dams along the rivers. In the right insert the names of the dams listed in the text is also shown.

constituting like a triangle in the far East extreme administrative boundaries of Syria [De Châtel, 2014b].

Jezira region is one of the richest in terms of water resources availability in the Middle East, serving as the so-called Syrian bread basket [De Châtel, 2014a; Hole and Smith, 2004], and has been exploited for agricultural purpose since thousands of years, as part of the Tigris-River Basin, known in the history as the Fertile Crescent.

Despite the richness of water resources, the Euphrates Basin is mainly characterized by an arid to semi-arid climate, with mean annual precipitation varying from 1000 mm in the Northern mountainous area, the major water catchment, to the 175 mm in the South Eastern Syrian steppe and 75 mm in Southern Iraq [UN-ESCWA and BGR, 2013].

Different civilizations populating this areas through history have been able to respond to these water scarcity, often accompanied by aridity and high climatic variability conditions, developing local systems for water management, for agricultural and domestic uses [De Châtel, 2014b]. In recent times though, in the twentieth century, the new born States after the the disgregation subsequent to the first and second World War, claimed rights on the use of Euphrates water, with strong consequences on the riparian neighbours.

This fragmentation brought also to a change in the management and control over the water resources. Until the 60s in fact, only Iraq was making large use of the river's waters, while in Syria limited irrigation was practiced mainly along the riverbed, in the floodplains [Beaumont, 1996] - see Zaitchik et al. [2002] for an accurate RS analysis of this issue. In the mid-60s, growing the interests of Syria and Turkey on the river's usage, the attention passed from downstream diversion schemes to upstream water storage projects, whose aim was of generating hydro-electricity and of providing large quantities of water for irrigation purposes [Beaumont, 1998]. The planning of this development started in the 1960s and the first big dams were complete in the early 1970s, as it's the case of the Keban Dam in Turkey and the Tabqa Dam in Syria on the Euphrates river (Fig. 1.4, right insert). In the 90s then several big water projects arrived to completion in both riparian Countries. In Syria with the Baath and Tishreen dams along the Euphrates, and three dams along the Khabur River near Al-Hassakah (Hassakah East, Hassakah West and Bassel Al Assad o Hassakah South, see Fig. 1.4 [Hole, 2009]. In Turkey the ambitious Southeastern Anatolia Project (GAP from the Turkish acronym) led to the creation of the Ataturk Dam, that constitutes by far the largest one in the area, with a capacity large enough to store the entire annual flow of river Euphrates [Beaumont, 1998]. This dam also supplies water through huge tunnels (Urfa o Halama tunnels) for irrigation purposes to two plains along the Turkish border, the Sanliurfa-Harran and the Ceylanpinar plains [Beaumont, 1996].

The GAP project foresees overall the construction of 22 dams and 19 hydro-power projects
on the Euphrates and Tigris rivers. The project is nowadays almost complete, despite
international and local criticism concerning its implementation [Sowers et al., 2010]. A
rich and complete description of the water projects planned in the area can be found in
[UN-ESCWA and BGR, 2013], with a detailed chronology of the implemented projects in
the three boundaries countries.

It's interesting to note that these projects, especially in Syria, were enforced after studies
and surveys on the feasibility of vast irrigation projects realized by international agencies
like FAO and USDA [Hole and Zaitchik, 2007]. For a country like Syria, that can count
mainly on water as the only available natural resource and therefore on agriculture as main
GDP income, this agricultural investment becomes vital, but the question arises upon the
sustainability of such huge projects.

For both Turkey and Syria the investment in huge water projects have been motivated by
the increasing population pressure since the 50s, and by the push to raise the standard
of living in the regions, some of the poorest and less developed by both sides [Beaumont,
1978]. In the same time, these dams has led also to significant changes in the social sys-
tem, with the displacement of several villages located on the dams' basin and social shifts.
Farmers had to adapt to different irrigation system that changed completely also the land-
scape, from rain-fed (especially in the Northern plains, see the 'limit for dry farming' in
Beaumont [1996]) and floodplain irrigation to heavily canalized irrigation spread along the
steppe and areas considered suitable for agricultural usage, as shown by Zaitchik et al.
[2002] in a study on the agricultural land pattern distribution.

The extensive changes come together with the question on their impacts on water quality,
for discharge of nutrient and organic matter residual from irrigation, and on soil degra-
dation, because of salinization due to water evaporation in the huge reservoirs and return
flows in the water system. The massive water engineering structures and the groundwater
withdrawal, much beyond the basin capacity [Gleick, 2014], impacted also the Euphrates
flow regime, that shows nowadays a decrease in the flow seasonality and amount compared
with the previous unaltered conditions [UN-ESCWA and BGR, 2013].

These negative impacts become even more prominent in light of the absence of solid and
unanimous agreements among the three riparian countries on the shared waters, which has
led to the situation where each of the States could develop its own water projects without
considering the possible consequences on the riparians. Negotiations have been attempted
on a number of occasions, end eventually led to bilateral agreements on water allocation
between Iraq and Syria (in 1990, after an escalation that culminated in a war threat from

Iraq in 1974) and between Turkey and Syria in 1987, bringing to the creation of a Joint Technical Committee and a Memorandum of Understanding among the three countries in 2009, not valid anymore since the starting of the Syrian Civil War in 2011 [Beaumont, 1998; Gleick, 2014; UN-ESCWA and BGR, 2013].

The 2006-2011 drought had a major impact on Syrian country, where "agricultural failures, economic dislocations and population displacement" took place [Gleick, 2014]. Several authors point out that it was not the drought alone responsible for the crisis, that eventually broke out in the ongoing conflict, but a "series of social, economic and political factors, including, in this case, growing poverty caused by rapid economic liberalization and the cancellation of state subsidies after 2005, a growing rural-urban divide, widespread corruption, rising unemployment" that wasn't adequately managed, if not exasperated, by the Syrian regime [Davis, 2015; De Châtel, 2014a]. As other countries in the region, Syria experienced an exceptional population growth over the past 60 years, passing from around 3 million in 1950 to over 22 million in 2012 [De Châtel, 2014a]. This caused a reduction in per capita available water, from over 5500 m^3 per person per year to below 760 by 2012, which categorizes Syria a scarce country as per water availability [Gleick, 2014]. The 2006-2011 drought hit a population already affected by a previous multi-year drought occurred in the early 2000, inducing the displacement of several population from rural areas to urban settlements, food insecurity (more than one million people in 2012 [FAO, 2012]) and unemployment growth. These facts summed up to a growing economic and political uncertainty, and the government's failure to size the critical situation led eventually to the eruption of an extensive dissent in the country, with consequences lasting till today.

Chapter 2

Change detection techniques for desert studies

Remote Sensing (RS) is the science of obtaining information on the Earth surface by remote observations, using sensors from airplanes and satellites. RS makes use of the spectral properties of different the surface features, that exhibit a characteristic trend, called *spectral signature*, in the visual (VIS) and Infrared (IR) regions of the spectrum (see Fig. 2.1).

In Remote Sensing (RS) of the environment, change detection covers the capability to
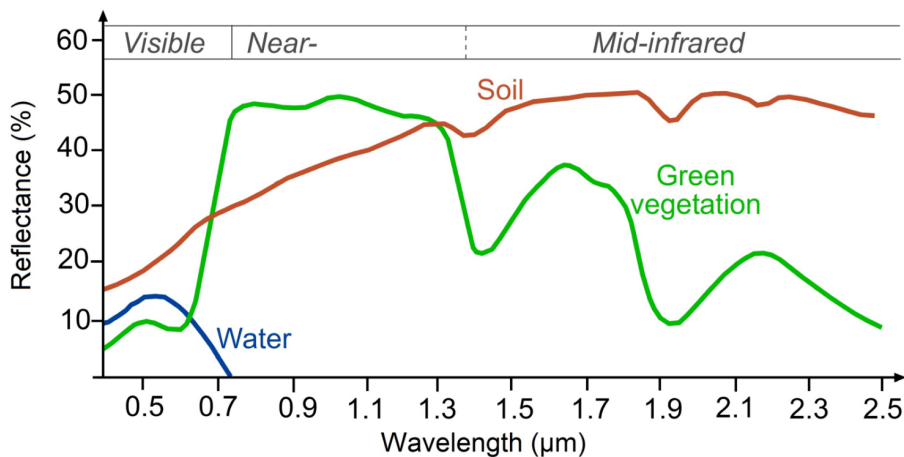
Figure 2.1: Typical spectral signatures of specific land cover types in the VIS and IR region of the electromagnetic spectrum (Source: http://www.seos-project.eu/)

identify the differences occurred on the Earth surface in time. This task can be performed through various techniques, and choosing between them depends also on the characteristics of the surface that need to be detected. Often change detection analysis is referred to as Land use/Land Cover Change (LULCC) analysis, referring to the characterization of the

terrestrial surface in terms of natural and man built types of cover. A basic condition for change detection studies is the preliminary co-registration of the images and the correction for external factors of change on the surface reflectance, such us atmospheric conditions and differences in Sun angle, plus the intrinsic characteristics of the single sensors. The selection of appropriate images, in terms of time of the year and weather conditions, allows to reduce the impact of these factors [Singh, 1989].

LULCC analysis requires in general a first identification of the surface covers, then a mechanism that compares the images along a temporal interval. The identification of the different types of cover is called image classification and can be carried out through several techniques and procedures [Coppin et al., 2004; Lu et al., 2004; Singh, 1989]. Most techniques process the single pixel and are so called pixel-based techniques. They differentiate from the relatively recent object-based analysis, that groups the pixels not only depending on their spectral behavior but also on geometrical characteristics, such as shape, color, size and similarity with neighboring pixels [Blaschke, 2010].

Considering pixel-based procedures, the categorization of the different types of classification techniques varies widely from one author to another, but mainly two different approaches can be recognized: supervised and unsupervised classification. In the first approach, supervised classification, the single images to be compared are classified separately, based on a preliminary knowledge of training areas for the different classes. The user identifies on the image some polygons of interest that correspond to specific land cover types. These training areas are then assigned to a software, that recognizes the spectral characteristics of each class and performs, through a selected algorithm, the classification of the rest of the image. The algorithms include maximum likelihood and minimum distance classification, among others.

Unsupervised procedures on the other hand are used in absence of samples or previous information on the ground. In this case the software makes use of the spectral characteristics of the pixels in order to group them in different classes. The techniques for unsupervised classification include clustering techniques like the ones used in unsupervised classification (maximum likelihood, minimum distance, k-means, ISODATA etc.) and also techniques that make use of simple algebraic procedures or more complex statistical and mathematical analysis procedures as a preliminary step for the classification. The algebraic procedures include differencing, ratioing, indexes (like Normalized Difference Vegetation Index – NDVI), while the mathematical analysis techniques include data transformations (like Principal Component Analysis - PCA, Tasselled Cap Transform – TCT, Multivariate Alteration Detector - MAD), Artificial Neural Network (ANN) analysis, fuzzy logic,

Bayesian network and others. Some unsupervised procedures promptly give as output a map of the change that must then be interpreted assigning a threshold, in order to differentiate the significant change from the pixels which are unchanged. The threshold choice, through customary or statistical criteria, is the key for the change interpretation [Eastman, 1992; Sui et al., 2008].

The choice of the type of techniques to be used depends on the purpose of the research and on the availability of ground truth data, accessory material and knowledge of the studied area. Supervised classification is an ideal procedure, but often finding both spatial and semantic accuracy can be challenging and relies on the skills of the classifier. Moreover the availability of knowledge on the field can not always be complied and an accurate classification can be time consuming. On the contrary, unsupervised approaches can be almost automatic and more time-efficient, but require the researcher to intervene in a second phase to interpret the results. Therefore, according to the aim of the researcher, the change detection analysis can be performed using a mixture of more techniques, the so-called hybrid approach, that combines two or more techniques in order to improve the results [Nussbaum and Menz, 2008; Sui et al., 2008].

In desertification studies, change detection covers a prominent role, since it allows the identification of surface elements that changed over a large scale, both spatial and temporal, and constitutes an effective method for observing, monitoring and characterizing the dynamism of drylands [Dawelbait and Morari, 2011]. One of the biggest challenge in this type of studies is the identification of common desertification indicators, since different ways of interpreting analogous factors can bring to different results [Albalawi and Kumar, 2013; Dawelbait and Morari, 2011]. Several indicators have been proposed in literature, considering in particular the soil reflectance contribution and the vegetative mass, whose deterioration can be a good indicator of desertification, being the major biological production of desert areas [Shafie et al., 2012]. In particular different authors used indicators of: land degradation (soil erosion, soil salinization [Metternicht and Zinck, 2003]), land use changes (expansion of agricultural or urban areas), bare soil expansion, drought and changing vegetation (perennial plant cover and biomass) [Albalawi and Kumar, 2013; Dawelbait and Morari, 2011; Pannenbecker, 2006]. The usage of the change detection techniques commonly used for vegetated areas, requires though some care in applications to desert areas: since vegetative cover is low, the reflectance of the exposed soil surface highly influences the pixels value [Dawelbait and Morari, 2011; Huete et al., 1985]. On the other hand, drylands have advantageous weather characteristics for change detection studies, exhibiting dry and cloudless conditions which remain unchanged for a long part of the year. These are ideal

for change detection studies, both on a short (seasonal) and long (years) scale, solving the issue connected with the atmospheric correction, a basic prerequisite for change detection studies [Singh, 1989].

A frequently used RS tool in desertification studies is vegetation indexes (VI), that were widely developed and used in literature, in particular the Normalized Difference Vegetation Index (NDVI) and its derivatives [Higginbottom and Symeonakis, 2014; Karnieli and Dall'Olmo, 2003; Morales-Salinas and Santibanez, 1998; Weiss et al., 2001]. The VI use the properties of photosintetically active vegetation, especially the pick in reflection in the NIR region, that is contrasted by a high absorption in the RED region. The NDVI takes the difference between the values of the image in these two spectral intervals and normalizes it:

$$NDVI = \frac{NIR - RED}{NIR + RED} \tag{2.1}$$

VI are often used in relation with the biomass Net Primary Productivity (NPP) and Rain Use Efficiency (RUE), which is as an indicator of the state of the vegetation cover [Higginbottom and Symeonakis, 2014], since its presence impacts the soil run off [Albalawi and Kumar, 2013; Verón et al., 2006].

In applications to desert areas, the soil reflectance tends to overwhelm the vegetation contribution, being the soil more exposed [Dawelbait and Morari, 2011; Huete et al., 1985; Shafie et al., 2012]. To reduce the soil contribution, some soil adjusted VI (SAVI) have been introduced [Albalawi and Kumar, 2013; Morales-Salinas and Santibanez, 1998].

In the present research the application of two semiautomated unsupervised techniques to desertification studies was analysed and discussed: the Change Vector Analysis (CVA), applied to the Tasselled Cap transform (TCT) features, and the Maximum Autocorrelation Factor (MAF) transformation of the Multivariate Alteration Detector (MAD) components. CVA, developed in the 80s by Malila and Lafayette [1980], gives as an output the direction of change between two dates for each pixel of an image, having the advantage, differently from canonical supervised or unsupervised classifications, of not needing a land-cover classification to be performed in advance. The CVA needs in input two (or more) spectral characteristics (bands or features) of the surface, that have a physical meaning and whose combination in the bands space can give a physical meaning to the change. For this aim TCT features are ideal candidates and have been widely used in several RS studies [Dawelbait and Morari, 2011; Flores and Yool, 2007; Malila and Lafayette, 1980; Sanchez Flores and Yool, 2007; Singh et al., 2012].

The second RS methodology used in the present study is the combined MAF/MAD analysis. MAD transformation was introduced by Nielsen et al. [1998] to improve the simple

image differencing technique, by considering the difference images with maximal variance, therefore obtaining a new set of uncorrelated images.

Although similar, MAD was intended to be an improvement over Principal Components Analysis (PCA) [Nielsen et al., 1998]. PCA in fact is a statistical procedure, used not only in RS but in several fields of Science, to transform a set of correlated variables to a new set of uncorrelated variables (called *components*) that consider the principal directions in which the data are spread in the bands space. PCA is useful to reduce the size and redundancy in the original data, since most of the information is contained in the first components, while the latter ones contain mainly noise. To do so, the PCA consider the maximum variance in the dataset, whereas MAD considers maximum autocorrelation, since it takes into account the maximum variance of the difference images. Doing so, MAD eliminates issues related to the possibility that a dominating element in the image affects the PCA components, with a disproportioned high variance compared to other elements of the image. Besides this, MAD has the huge advantage of being invariant for linear transformations of the data, making it insensitive to the application to raw DN or transformed images [Canty, 2014; Nielsen et al., 1998].

Like PCA, though, MAD analysis is locally applied to the single pixel and therefore doesn't retain the spatial context of the adjacent pixels. With this consideration in mind, Nielsen et al. [1998] introduced the application of the MAF transform, which is intended to produces variates ordered by spatial autocorrelation [Switzer and Green, 1984]. The MAD/MAF method in conclusion provides a "statistically rigorous system to determine the spatially coherent patterns of major change in an image sequence" [Nielsen et al., 1998].

Several comparison studies have been carried out on the performance of these three major techniques, CVA, PCA and MAD, also in desertification studies [Coppin et al., 2004; Nori et al., 2008; Pannenbecker, 2006]. In particular [Pannenbecker, 2006] concluded that CVA and MAD were the most effective techniques, in terms of desertification indicators and in terms of results. Considering also the added value, described above, of the MAF applications to the MAD components, in the present research it was chosen to use CVA and MAD/MAF analysis, and further develope them in order to improve them by combining the results of the two.

2.1 Tasselled Cap or Kauth-Thomas Tranform

Among RS techniques, linear transformation methods like the Tasselled Cap transform (TCT) have the advantage of reducing the amount and redundancy of data, providing

different information in derived components. The output of these transforms may also be used as input for further analysis, like Change Vector Analysis (CVA), since the output bands of the TCT have a physical meaning in terms of the characteristics of the soil cover. Referring to the TCT, also called Kauth-Thomas transform, one refers to the transformation firstly introduced by Kauth and Thomas in 1976 Kauth and Thomas [1976]. It consists of a linear transformation of the pixels' values of a satellite image of terrestrial surface, in order to convert the originally highly correlated bands (in the Infrared and Visible region, see Fig. 2.2) to a new set of uncorrelated axes.

Their study was based on Landsat MSS images of a small crop field sample in the United
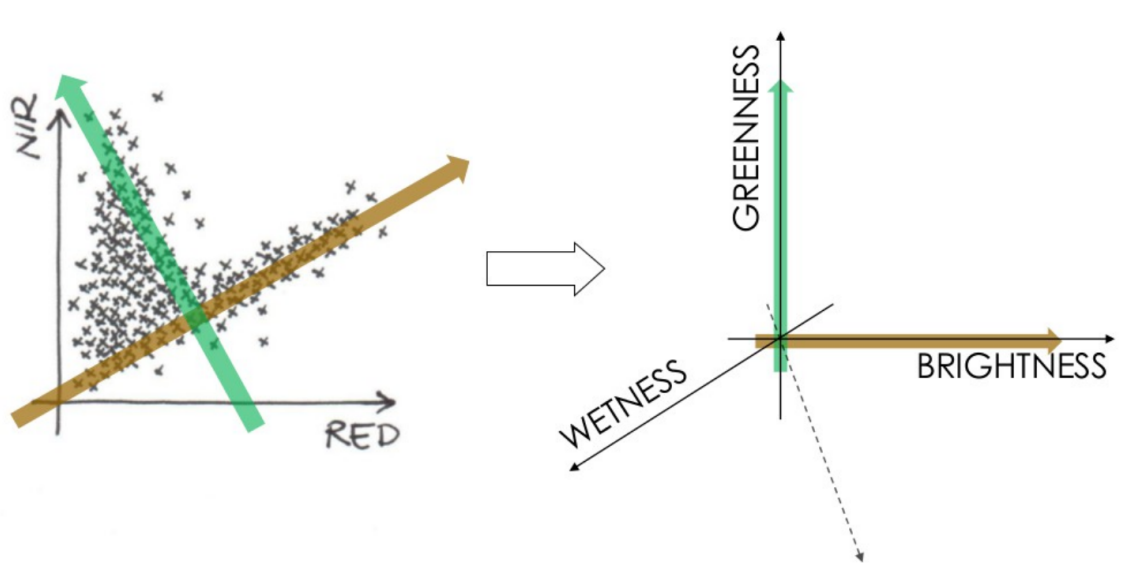
Figure 2.2: Rapresentation of the TCT tranformation from the RED-NIR space to the TCT features space. The brown arrow indicates the direction of the soil reflectance pixels, while the green arrow indicates the of the vegetation pixels.

States (Illinois), and it investigated the relationship between vegetation and soil spectral reflectances in the bands-space in a multitemporal scale; namely they followed the vegetation growth from the bare soil to plants senescence. What was evident by their study was the evolution in the disposition of the data on the bands-space, whose shape resembles the one of a "hat with tassels", hence the technique's name (see Fig. 2.3). The principle is the same as the one of Principal Components Analysis: converting the original image bands to a set of uncorrelated bands. Thus starting from the original space of m bands the TCT defines a new n ($n \leq m$) dimensions set of axes in which the image pixels have different coordinates. As a linear transform, the TCT consists of a set of parameters (frequently referred to as *coefficients*) that weigh the original spectral bands' values and sum up to
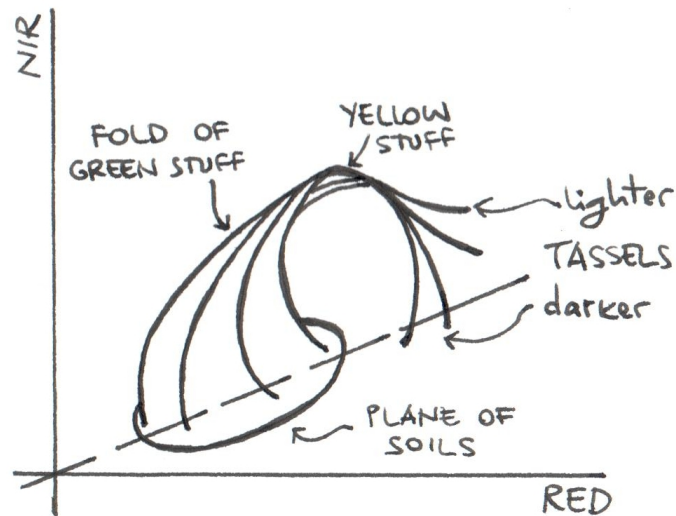
Figure 2.3: The tasselled cap, adapted from [Kauth and Thomas, 1976].

give as an output a new value for that pixel in the new set of axes, therefore literally transforming the coordinates reference system passing from the satellite bands space to a new TCT features space (fig. 2.2). Unlike other transformations, Principal Component Analysis (PCA) as one example, TCT transform is not image-dependent, therefore once a set of parameters for the transformation is given, it can be used to convert any image with the same characteristics (type of satellite, data and region) [Ivits et al., 2008; Yarbrough et al., 2012; Zanchetta et al., 2015].

The axes of the new coordinate system have a physical meaning in terms of the carachteristic of the surface. Namely the first axis, called 'Brightness', is a feature associated with variations in the soil reflectance; the second one is the 'Greenness' axis, associated with variations in green vegetation, while to the third and forth axis had been given different interpretations in different studies. In the first paper by Kauth and Thomas [Kauth and Thomas, 1976] the third axis, named 'Yellowness' , was correlated to plant senescence and the fourth one called 'Non-such', was chosen orthogonal to the first three ones, not carrying any particular information. Crist and Cicone [Crist and Cicone, 1984] then in 1984, from simulated and actual Landsat 4 and 5-TM data analysis, found out that the third feature, unlikely the first two ones which were comparable with those of the MSS, is considered indicative of soil moisture, therefore generally referred to as 'Wetness'. The remaining three features weren't considered significative, for the greatest amount of information was contained in the first three ones.

Several applications of TCT have been carried out for ecosystem and environmental anal-

ysis. When dealing with desert conditions though, special attention should be paid in applying the existing coefficients, noticing whether the original studies were carried out specifically for vegetated areas. One known remark to the use of TCT in RS, in particular when carrying out comparison between multitemporal images [Coppin et al., 2004; Lu et al., 2004; Mather, 2004] is the fact that the results have been retrieved by the analysis of limited samples of terrestrial surface. To derive the transformation coefficients, Kauth and Thomas, in fact considered only a single sample of soil and agricultural area [Kauth and Thomas, 1976]. To face this issue, Crist and Cicone in their studies extended their research to a bigger amount of samples on the ground, together with field spectrometry and laboratory measurements of soil samples. Even if the number of analized images wasn't considerably vaste, the fact that the calculated transformation produced comparable results with those achieved with simulated datasets suggested that the transformation could be used directly with other scenes as well, once geometrically and atmospherically corrected [Crist and Cicone, 1984]. However, the slope of the soil-line will be dependent on the type and condition of the soil [Ivits et al., 2008], and its reflectance characteristics [Mather, 2004].

A second known issue is connected with the the correction of the images for external effects, as pointed out by Kauth and Thomas in their first paper. In multitemporal images analysis in fact, besides a precise registration, a radiometric and atmospheric calibration (or normalization) between images is a prerequisite to carry out a change detection analysis [Coppin et al., 2004; Lu et al., 2004].

Thus application of Tasselled Cap parameters to raw digital number (DN) can be problematic, being image affected [Ivits et al., 2008]. To solve this problem, Huang [Huang et al., 2002a] suggests to calculate the TCT coefficients for at-satellite reflectance (also called Top Of Atmosphere Reflectance - TOAR.

Concerning atmospheric corrections, Huang, starting from previous works of Markham and Chander [Chander and Markham, 2003; Markham and Barker, 1986], developed a workflow for TOAR for Landsat ETM+ images, where he concludes that "the same observations could be made for previous Landsat systems, once appropriate parameters for at satellite radiance and reflectance equations are available" [Huang et al., 2002b].

In summary, if we don't take into account the first TCT coefficients calculated for MSS images, basically four TCTs have been developed for Landsat TM and ETM+ sensors:

- in 1984 for DN data - Landsat 4 [Crist and Cicone, 1984], see Tab. 2.1;

- in 1985 for reflectance factor data - Landsat 4 [Crist, 1985], see Tab. 2.2;

	B1	B2	B3	B4	B5	B7
Brightness	0.3037	0.2793	0.4743	0.5585	0.5082	0.1863
Greenness	-0.2848	-0.2435	-0.5436	0.7243	0.0840	-0.1800
Wetness	0.1509	0.1973	0.3279	0.3406	-0.7112	-0.4572
4th	0.8832	-0.0819	-0.4580	-0.0032	-0.0563	0.0130
5th	0.0573	-0.0260	0.0335	-0.1943	0.4766	-0.8545
6th	0.1238	-0.9038	0.4041	0.0573	-0.0261	0.0240

Table 2.1: Landsat 4 Tasselled Cap coefficients for DN data, 1984 [Crist and Cicone, 1984], as in Crist and Kauth [1986] (values slightly different for features 4th to 6th)

	B1	B2	B3	B4	B5	B7
Brightness	0.2043	0.4158	0.5524	0.5741	0.3124	0.2303
Greenness	-0.1063	-0.2819	-0.4934	0.7940	-0.0002	-0.1446
Wetness	0.0315	0.2021	0.3102	0.1594	-0.6806	-0.6109
4th	-0.2117	-0.0284	0.1302	-0.1007	0.6529	-0.7078
5th	-0.8669	-0.1835	0.3856	0.0408	-0.1132	0.2272
6th	0.3677	-0.8200	0.4354	0.0518	-0.0066	-0.0104

Table 2.2: Landsat 4 Tasselled Cap coefficients for Reflectance factor data, 1985 [Crist, 1985]

- in 1986 for DN data - Landsat 5 [Crist and Kauth, 1986], see Tab. 2.3;

- in 2002 for TOAR-reflectance data - Landsat 7 [Huang et al., 2002a], see Tab.2.4).

While for Landsat images TCT have been calculated and widely used, for other satellites, like the SPOT family, no wide implementation is found in literature. A study was conducted by Chang in 1992 [Chang, 1992] and by Ivits in 2008, which cites other two studies made in 1987 and 1991 [Ivits et al., 2008].
Considering Landast available TCT tranformations, particular attention should be paid with regard to which set of coefficients to use when implied in the the comparison between images. In fact the several available TCT coefficients have been calculated distinctly for different types of data (for example for DN and for TOAR data), and for different sensors

	B1	B2	B3	B4	B5	B7	Additive term
Brightness	0.2909	0.2493	0.4806	0.5568	0.4438	0.1706	10.3695
Greenness	-0.2728	-0.2174	-0.5508	0.7220	0.0733	-0.1648	-0.7310
Wetness	0.1446	0.1761	0.3322	0.3396	-0.6210	0.4186	-3.3828
4th	0.8461	-0.0731	-0.4640	-0.0032	-0.0492	0.0119	0.7879
5th	0.0549	-0.0232	0.0339	-0.1937	0.4162	-0.7823	-2.4750
6th	0.1186	-0.8069	0.4094	0.0571	-0.0228	0.0220	-0.0336

Table 2.3: Landsat 5 Tasselled Cap coefficients for DN data, 1986 [Crist and Kauth, 1986]

	B1	B2	B3	B4	B5	B7
Brightness	0.3561	0.3972	0.3904	0.6966	0.2286	0.1596
Greenness	-0.3344	-0.3544	-0.4556	0.6966	-0.0242	-0.2630
Wetness	0.2626	0.2141	0.0926	0.0656	-0.7629	-0.5388
4th	0.0805	-0.0498	0.1950	-0.1327	0.5752	-0.7775
5th	-0.7252	-0.0202	0.6683	0.0631	-0.1494	-0.0274
6th	0.4000	-0.8172	0.3832	0.0602	-0.1095	0.0985

Table 2.4: Landsat 7 Tasselled Cap coefficients for TOAR data, 2002 [Huang et al., 2002a]

(Landsat 4 and 5 TM and Landsat 7 ETM+). Therefore when performing a comparison between images taken from different sensors, one should use the same type of data, in order to be coherent in terms of measurement units and outcomes. There seem though to be some confusion in literature in the use of different TCT transformations, in particular because not all of the different satellites have TCT sets available for each type of satellite. However, regarding the contingent use of Landsat 5 and Landsat 7, a report on MRLC image processing procedure from U.S. Geological Survey [MRLC, 2001], concludes that "because the Landsat 5 TM sensor and the Landsat 7 ETM+ sensor are geometrically and radiometrically compatible, the standard landsat 7 processing procedures (including converting DN to at-satellite reflectance, tasselled cap transformation, and normalized burn ratio) also apply to L5 TM images". Based on this assumption, the Landsat 5 and Landsat 7 TCT have been used in the present research without distinction.

Regarding Landsat 8 OLI satellite, the coefficients present in literature were also calculated for vegetated conditions [Baig et al., 2014; Liu et al., 2015], therefore in this research a new set of parameters has been calculated for desert conditions.

2.2   Change Vector Analysis

Change Vector Analysis (CVA) was first implemented by Malila and Lafayette [1980] for detecting forest changes and then widely adopted for LULCC detection by several authors also for desert areas [Bayarjargal et al., 2006; Dawelbait and Morari, 2011; Lorena et al., 2002], sometimes further developed and variated [Dawelbait and Morari, 2011; Dubovyk et al., 2013; Flores and Yool, 2007; He et al., 2013; Lambin and Strahlers, 1994; Singh and Talwar, 2014]. The technique takes in input two (or more) spectral variables -i.e. spectral bands, surface features indicators, biophysical indicators or spectral indices [Lambin and a.H. Strahler, 1994; Malila and Lafayette, 1980]- to produce in output a map of the change

occurred for each pixel of the image between two dates. For each date, the pixel's values in the two variables are plotted on the variables space (see Fig. 2.4). Any change in the chosen variables implies a displacement in the pixel's position in the variables space, generating a vector of the change in time (*change vector*). The magnitude (length) of the change vector gives the intensity of the change on the surface while the direction (angle) gives the type of change occurred. Once a threshold is chosen, the significant change is given as those pixels that exceed that value in the map of the direction.

In the framework of the present study, only bidimensional CVA will be considered, even
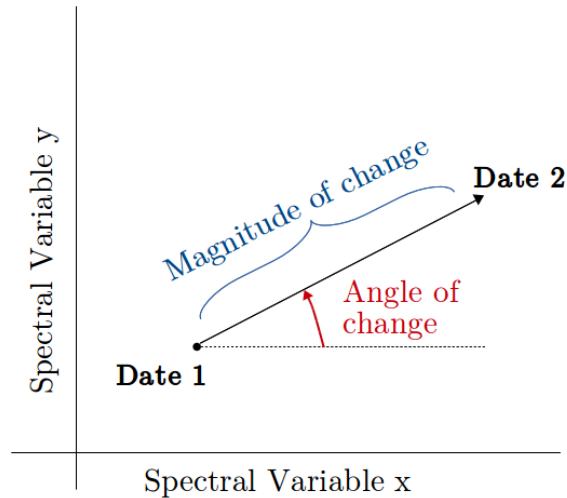
Figure 2.4: Change vector components magnitude and direction for a pixel's value in two variables (bands) space between two time limits (adapted from Malila and Lafayette [1980].

though the technique can be performed on a higher number of variables. Specifically in three dimensions the CVA has been analyzed by Allen and Kupfer [2000]; Bovolo and Bruzzone [2006]; Bovolo et al. [2012] among others, but will not be taken into account in the following considerations.

The magnitude M and angle θ of the vector change between time t_1 and t_2 can be retrieved by simple Pythagorican calculation as follows.

$$M = \sqrt{(x_2 - x_1)^2 + (y_2 - y_1)^2}$$

$$\theta = arctan\left(\frac{y_2 - y_1}{x_2 - x_1}\right)$$

Where x_i and y_i are respectively the values of the pixel in abscissa and ordinate in the two different times (with $i = 1, 2$), and θ is the angle between the direction of the abscissa and the vector of the change (see Fig. 2.4).

The application of CVA produces in output of the CVA are two maps: the angle map bears

a meaning in terms of change to the surface characteristics, while the magnitude map gives the amount of the change occurred.

The semantic interpretation of the change is given by the specific spectral bands or features used. Since the variables are chosen as indicators of surface characteristics, their combined variation can have a meaning in terms of surface change. Several variables were used in literature, in general most of the studies took into account an indicator of the soil reflectance and an indicator of the vegetation vigor. With this choice in mind, Malila et al. suggested to use the TCT features Brightness and Greenness [Malila and Lafayette, 1980], as used by other authors [Bashir and Csaplovics, 2011; Kuzera et al., 2005; Lorena et al., 2002; Sanchez Flores and Yool, 2007; Siwe and Koch, 2008]. Other researchers used as indicator of the soil reflectance variables like Albedo [Karnieli et al., 2014] and Bare soil index [Nguyen, 1986; Son et al., 2009], combined with an indicator of the vegetation, mainly NDVI [He et al., 2013; Lambin and Strahlers, 1994], or NDVI alone [Chen et al., 2001]. Further authors chose different types of indicators, like drought indices [Bayarjargal et al., 2006], the TM Landsat bands [Johnson and Kasischke, 1998], land cover types [Chen et al., 2003], land cover classification [Dawelbait and Morari, 2011]. In the present research, the variables proposed by Malila and Lafayette [1980], namely the two TCT features Brightness and Greenness were adopted.

Once the angle of the change vector is mathematically determined, the meaning of the CVA direction is not straightforward. Generally a simplified interpretation of the four quadrants of the bands space is given: the first quadrant in fact represents a positive change for both variables, the second quadrant a positive change for the y variable and negative change for the x variable, and so on. This approach is followed for example by Bashir and Csaplovics [2011]; Dawelbait and Morari [2011]; Kuzera et al. [2005]; Singh et al. [2012], that nonetheless consider the first and third quadrant as not significant for a change, since both variables changed in the same direction, therefore reducing the categories of the change to three (both positive, both negative, persistance of conditions). Other authors consider the four quadrants as four different categories of change, for example Karnieli et al. [2014]; Siwe and Koch [2008]; Son et al. [2009]. Other types of interpretation were given by the single authors choosing specific criteria not always connected with the quadrants meaning or direction, as in Bovolo and Bruzzone [2006]; Chen et al. [2001]; Johnson and Kasischke [1998]; Lambin and Strahlers [1994].

In line with the interpretation provided in other researches for desert conditions [Karnieli et al., 2014; Lorena et al., 2002], we chose the four quadrants categorization and defined the four change directions as follows. The first quadrant $(0 - 90°)$, which is characterized by an
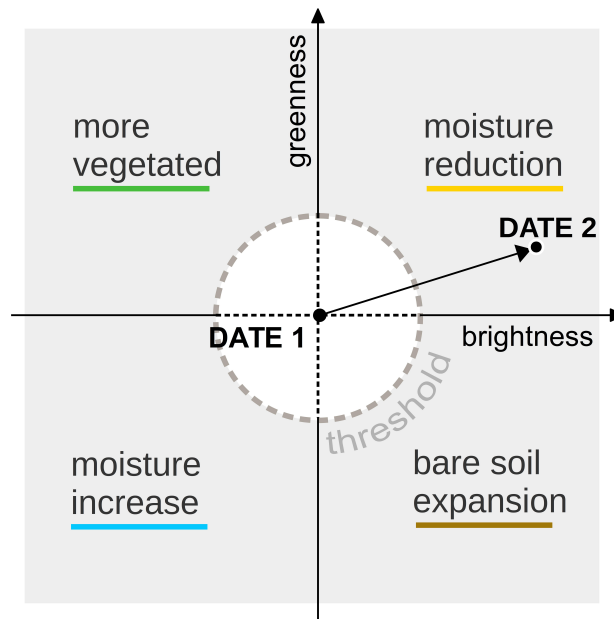
Figure 2.5: CVA: meaning of the direction of the change for the four quadrants, considering the vector between two dates. The colors that will be used later on for the classification are also shown.

increase both in Greenness and Brightness, indicates moisture reduction and in desert areas has been found connected with a change towards salty surfaces, i.e. drying lakes/water ponds [Karnieli et al., 2014]. The forth quadrant $(270 - 360°)$, with increasing Brightness and decreasing Greenness is also connected to a change towards drier conditions, namely towards bare soil/sand expansion, and is strongly related to great losses of vegetation biomass and to bare soil expansion. The other two quadrants, with decreasing Brightness, are connected with changes towards more wet conditions: the second quadrant $(90 - 180°)$ is indicative of chlorophyll increase and of regrowth and regeneration of vegetated features, and the third quadrant $(180 - 270°)$, where both spectral features have a decrease, indicates burning or water, and in general a change towards higher moisture land and water (Fig. 2.5) [Lorena et al., 2002; Zanchetta et al., 2015].

Given the meaning of the change, the significant change is given by a threshold on the magnitude map. The determination of the threshold and the interpretation of the direction of the change are critical points when applying the CVA technique and have been faced in several ways by different authors [Chen et al., 2003]. The threshold in particular can be set with the use of empirical values, or through interactive trial-and-error procedures, or semi-automated approaches [Bruzzone and Prieto, 2000; He et al., 2013]. For this work,

the threshold given by the average plus the standard deviation of the magnitude values was chosen, as in other sources [He et al., 2013]. With this choice, the threshold is not a fixed value, but it changes for each pair of images taken into consideration. Nonetheless in this way the value has a statistical meaning and the technique can be reproduced by other researchers, even if the range of the magnitude values differs, as in most of the cases.

It is important to notice that CVA gives just a direction of the change, meaning there's no classification of the actual features present on the Earth surface. For example, water becoming soil and soil becoming dryer will look the same in the output map (change towards moisture reduction). In this sense, CVA interpretation can be improved by its usage combined with other RS methodologies.

2.3   Multivariate Alteration Detector and Maximum Auto-correlation Factor

Multivariate Alteration Detector is a broadly used technique of images linear transformation based on canonical correlation analysis, developed Nielsen et al. [1998]. The idea is to improve the simple image differencing technique by "making the images as similar (correlated) as possible, before taking their difference".

For N input bands MAD gives N output difference images, called *MAD components*. The components are sorted by increasing variance, and each one represents a different type of change, therefore the output exhibits noise spread over several components [Canty, 2014]. To address this issue Nielsen et al. [1998] introduced the application of the Maximum Autocorrelation Factor (MAF) transformation to the MAD components. While MAD performs local operations, related to the single pixels characteristics, MAF finds the spatially coherent patterns of major change taking into account the spatial coeherence of neighboring pixels. MAF is a form of Minimum Noise Fraction (MNF) procedure that generates components with maximum Signal to Noise Ratio (SNR) [Canty, 2014]. Like CVA, the MAD/MAF technique is considered an unsupervised change detection technique, and requires that a threshold be applied on the components in order to filter the meaningful change. The discussion on this topic is given in the following sections.

Several applications of MAD/MAF are found in literature for change detection studies in RS [cit.]. A great advantage of the MAD/MAF, as a semi-automated technique, is to allow to perform change detection studies on wide scales in short calculation times. Beside this, MAD and MAF procedures are invariant to affine transformations, therefore they can be applied to either raw digital number, TOAR or uncorrected for atmospheric corrections

data, eliminating the actions required on the images corrections to be performed before the image analysis.

2.3.1 Multivariate Alteration Detector

Let us consider two N bands images, represented by the vectors $\mathbf{X}$ and $\mathbf{Y}$ (with length equal to N), of the same location in two different times t_1 and t_2.

$$\mathbf{X} = [X_1, ..., X_N]^\intercal \qquad \text{and} \qquad \mathbf{Y} = [Y_1, ..., Y_N]^\intercal$$

Performing a linear transformation on the vectors, a single image for each time can be generated as:

$$U = \mathbf{a}^\intercal \mathbf{X} = a_1 X_1 + ... + a_N X_N \qquad \text{and} \qquad V = \mathbf{b}^\intercal \mathbf{Y} = b_1 Y1 + ... + b_N Y_N$$

In this way, the difference image between time t_1 and t_2 is given by the scalar difference $U - V$ and the "change information is now contained in a single image" [Canty, 2014; Nussbaum and Menz, 2008].

The vectors $\mathbf{a}$ and $\mathbf{b}$ are to be determined in a convenient way. Nielsen et al. [1998] suggests to use standard Canonical Correlation Analysis (CCA), as described by Hotelling [1936]. CCA finds two sets of linear combinations of the original variables, where the first two linear combinations (called canonical variates) are the ones with the largest correlation (called first canonical correlation). The second canonical correlation and canonical variates are defined subject to the condition that they are orthogonal to the first ones, and this process goes on for the higher-order canonical correlations and variates. Performing differences between these pairs of variates allows then to consider a change detection analysis based on linear combinations of the original variables, ordered by correlation (similarity) between pairs [Nielsen et al., 1998].

As by the work of Nielsen et al. [1998] the vectors $\mathbf{a}$ and $\mathbf{b}$ are chosen in a way that the positive correlation between U and V is minimized, therefore imposing that the difference image

$$D = U - V = \mathbf{a}^\intercal \mathbf{X} - \mathbf{b}^\intercal \mathbf{Y}$$

has a maximal variance, subject to the constraints that $Var\{\mathbf{a}^\intercal \mathbf{X}\} = Var\{\mathbf{b}^\intercal \mathbf{Y}\} = 1$. This corresponds to determining linear combinations with minimum correlation, in compliance

with CCA. The MAD transform

$$
\begin{bmatrix} \mathbf{X} \\ \mathbf{Y} \end{bmatrix} \longrightarrow \begin{bmatrix} \mathbf{a}_N^\mathsf{T}\mathbf{X} - \mathbf{b}_N^\mathsf{T}\mathbf{Y} \\ . \\ . \\ . \\ \mathbf{a}_1^\mathsf{T}\mathbf{X} - \mathbf{b}_1^\mathsf{T}\mathbf{Y} \end{bmatrix}
$$

where a_i and b_i $(i = 1, ..., N)$ are defining coefficients derived from standard CCA, thus is given by the "variates we get when we subtract corresponding canonical variates in reverse order" [Nielsen et al., 1998].

The MAD components

$$
MAD_i = U_i - V_i = a_i^\mathsf{T}\mathbf{X} - \mathbf{b}_i^\mathsf{T}\mathbf{Y}
$$

corresponds then to i-th difference bearing the maximum variance between two sets of variables that are positively correlated. Each MAD_i represents a different type of change, supposing that similar types of spatial change will be grouped in one component, since each of them is found under the constraint of being uncorrelated with the preceding one [Nori et al., 2008]. In this way the actual changes are emphasized [Nussbaum and Menz, 2008].

2.3.2   Maximum Autocorrelation Factor

Maximum Autocorrelation Factor (MAF) was firstly applied by Nielsen et al. [1998] to the MAD components in order to retain the spatial context of the data in the change detection results. In fact MAD components, like PCA, fail to consider the overall spatial coherence of the change, taking into account only local (single pixel) analysis. Differently from PCA transformation, that maximizes the variance, MAF maximizes the autocorrelation between images. MAF transform was introduced by Switzer and Green [1984] to isolate the noise component of the data, transforming a set of original measurements to "a new set of variates with the following properties: the low-number variates have minimal spatial autocorrelation, identified as mainly noise, and the high numbered variates have maximal spatial autocorrelation, identified as mainly signal".

As such, MAF transformation is a form of Minimum Noise Fraction (MNF) procedure that generates components with maximum Signal to Noise Ratio (SNR): assuming that the noise is derived from the evaluation of the difference between values of neighboring pixels, the first MAF component will exhibit maximum autocorrelation (areas with maximum change), while the noise is expected to be more present in lower order components,

having low spatial correlation [Canty, 2014].

The first component (MAF1) is the linear combination of the variables that maximizes autocorrelation, the second one (MAF2) is the same type of linear combination with the condition that it is orthogonal to MAF1, and so on, up to the higher order components, whose number equals the number of initial variables. The formulation of the MAF transformation of the MAD components (MAD/MAF) is via a vector of coefficients $\mathbf{c}$, such that

$$Corr\{\mathbf{c}^\mathsf{T}\mathbf{D}(\mathbf{x}) , \mathbf{c}^\mathsf{T}\mathbf{D}(\mathbf{x} + \boldsymbol{\Delta})\}$$

is maximized, where $\mathbf{D}(\mathbf{x})$ is the considered variable (in this case $D = a_i^\mathsf{T}\mathbf{X} - \mathbf{b}_i^\mathsf{T}\mathbf{Y}$) at location $\mathbf{x}$ and $\boldsymbol{\Delta}$ is a spatial interval. A complete description of the MAF transformation retrieval is available in Switzer and Green [1984].

MAF components, like MAD components, are invariant to linear scaling of the input data and can therefore be applied equally on raw data as well as on transformed images.

In order to get a value for the significant change, a threshold can be applied to the MAD/-MAFs. Since the MAD (or MAD/MAF) variates are approximately normally distributed about zero and uncorrelated, a good candidate for the thresholding is in terms of standard deviations about the mean for each component. In this sense, all the pixels whose intensities are within $\pm N\sigma$ of zero are considered unchanged. A usual choice for the threshold is taking values lower and higher than two standard deviations ($\pm 2\sigma$) from the mean [Barreda-bautista et al., 2011; Canty, 2014; Canty and Nielsen, 2006]. The threshold criterion though is not univocal and more sophisticated criteria based on statistical analysis, like Bayes Rule of Minimum Error [Bruzzone and Prieto, 2000; Zhang et al., 2007] and Spectral Mixture Analysis (SMA) [Canty, 2014], have been introduced in literature. For the aim of this study, and missing ground truth data necessary for the SMA, the basic threshold was chosen.

Chapter 3

Materials

3.1 Satellite data

3.1.1 SPOT satellites

The SPOT (*Satellite Pour l'Observation de la Terre*) satellites are a series of Earth observing satellites operated by the French space Agency CNES (Centre National d'Etudes Spatiales), located in Toulouse, France.

Seven SPOT satellites have been launched since 1986. SPOT 1, 2, and 3 carried the High Resolution Visible (HRV) sensor, with three channels at a spatial resolution of 20 m and a Panchromatic band at 10 m. SPOT 1 was retired at the end of 1990, following the launch of SPOT 2 in the beginning of 1990, who was deorbited in 2009. SPOT 3, launched in 1993, was lost following a technical error [Mather, 2004].

In 1998 SPOT 4 was launched, carrying still an HRV instrument extended with an additional mid-Infrared sensor (HRVIR) at 20 m resolution. Before stopping working in July 2013, SPOT 4's altitude was lowered and the satellite programmed to acquire scenes from 42 sites, with a 5 days interval time. The images are collected in a dataset called SPOT 4-Take 5, freely available and downloadable *.

SPOT 5, launched in 2002, carries two High Resolution instruments - Geometric (HRG) and Stereoscopic (HRS) with 10 to 20 m resolution, in multispectral mode, and 2.5 to 5 m in panchromatic mode. Like SPOT 4, it carries also a Vegetation (VGT) sensor with low spatial resolution (1 km) meant to be used to generate global datasets.

SPOT 6 and 7 were launched respectively in 2012 and 2014, and constitute a constellation of satellites with spatial resolution ranging from 1.5 m (panchromatic) to 6 m (multispectral).

---

*http://spirit.cnes.fr/take5/

For the aim of the present research, the SPOT4-Take 5 scenes acquired above Al Azraq Oasis were used. The selected dates for the analysis are listed in Tab. 3.3, while Tab. 3.1 lists the characteristics of the SPOT 4 HRVIR sensor, for the bands used in the current research.

Denomination	Band n.	Range (μm)
Green	1	0.50-0.59
Red	2	0.61-0.68
Near infrared (NIR)	3	0.79-0.89
Shortwave infrared (SWIR)	4	1.58-1.75

Table 3.1: Technical data of selected spectral bands used in the TCT transform for the SPOT 4 HRVIR (Visible & Infrared High-Resolution) sensor, with resolution of 20 m.

3.1.2   Landsat satellites

Landsat program is the longest running civilian project for Earth satellite imagery, started in 1972 with the launch of Landsat 1 satellite by the US National Aronautics and Space Administration (NASA). It has a substantial dataset of images available online [†] and has at date two operative satellites, Landsat 7 and Landsat 8 (launched in 1999 and 2013). While Landsat 6 was lost in the launch phase, Landsat 5 has been the most long-running of all (launched in 1984, stopped working in 2013) and its rich archive of imagery is still available [Mather, 2004]. A comparison of the different sensors' coverage in the electromagnetic spectrum, from the Visible to the far-Infrared region, is shown in Fig. 3.1.

 Landsat 1 to 5 carried the multispectral Scanner (MSS), a sensor with four multispectral bands, two in the Visible region and two in the near-Infrared region, with spatial resolution from 79 to 240 m. From Landsat 4 to 7 also the Thematic Mapper (TM) sensor was aboard the satellites, which includes seven multispectral bands with 30 m resolution (with the exception of the Thermal Infrared band, numbered 6, at 120 m resolution).

Landsat 7 satellite was launched in 1999 and carries the Enhanced Thematic Mapper Plus (ETM+) sensor, which replicates the capabilities of the TM sensor adding a Panchromatic band and a Thermal Infrared band (15 and 60 m spatial resolution). A further improvement over these instruments is the Operational Land Imager (OLI) and the Thermal InfraRed Sensor (TIRS) aboard Landsat 8, with 15 days acquisition interval and with new spectral

---

[†]http://glovis.usgs.gov
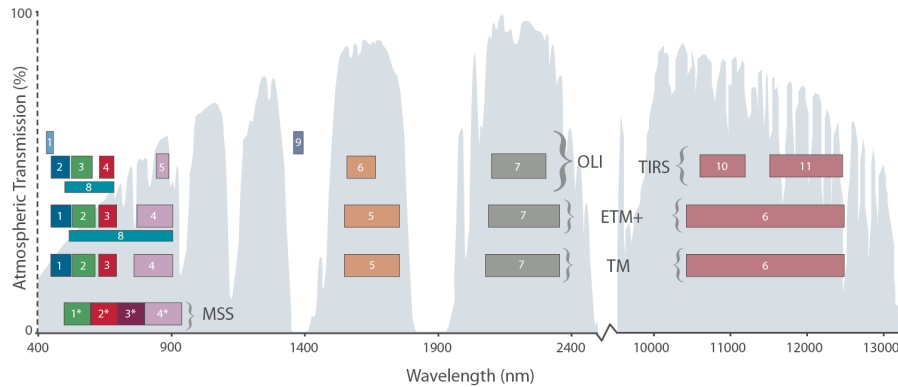
Figure   3.1:   Visual   comparison   of   Landsat   spectral   bands   (Source: https://landsat.gsfc. nasa.gov/about/technical-information/)

bands (for a total of eleven), with spatial resolution ranging from 30 m, in the Visible and Infrared region, to 100 m for the TIRS.

Tab. 3.2 displays the characteristics of selected spectral bands of Landsat 5 and Landsat

Denomination	Landsat 5		Landsat 8	
	Band n.	Range (μm)	Band n.	Range (μm)
Coastal aerosol			1	0.43-0.45
Blue	1	0.45-0.51	2	0.45-0.52
Green	2	0.52-0.60	3	0.53-0.59
Red	3	0.63-0.69	4	0.64-0.67
Near infrared (NIR)	4	0.76-0.90	5	0.85-0.88
Shortwave infrared (SWIR1)	5	1.55-1.75	6	1.57-1.65
Shortwave infrared (SWIR2)	7	2.08-2.35	7	2.11-2.29

Table 3.2: Technical data of selected spectral bands used in the Tasselled Cap Transform for the Landsat 5 satellite TM (Thematic Mapper) and Landsat 8 satellite OLI (Operational Land Imager) sensors (spatial resolution of 30 m).

8, for future reference in the research, while the dates of the Landsat scenes used in the present research are provided in Tab. 3.3, 3.4 and 3.5, separated by the different scope and use in the research. In general the criterion for the image selection was conditioned by the presence of clouds and by the dataset availability. For the change detection analysis in particular, to reduce the seasonal variation and to retrieve similar vegetative conditions on the surface, images in the same time of the year were chosen. Considering the arid and semi-arid climate conditions, images taken at the end of the summer (August-September)

	SPOT 4	Landsat 5	Landsat 8	Landsat path/row
Egypt (Al Fayoum)		1986/11/04 1998/04/11 1999/02/09	2014/08/13 2015/01/20	177/40
Egypt (Lake Burullus)	2013/02/03 2013/06/18			
Jordan (Al Azraq)	2013/02/04 2013/06/19	1985/11/05 1998/05/01 1999/02/13	2013/12/20 2014/03/26	173/38
Tunisie (Lake Sidi Saad)	2013/03/10 2013/06/18			
Tunisie North			2014/04/09 2014/08/15	191/35
USA (Maricopa)	2013/02/14 2013/06/19			

Table 3.3: Selected dates for SPOT 4, Landsat 5 and Landsat 8 satellites, for the TCT calculation (see 4.1)

Date	Satellite	Path/row	Denomination
1984/08/30	Landsat 5	173/38	Oasis 1984
1984/09/01		171/35	Lake 1984
2015/08/20	Landsat 8	173/38	Oasis 2015
2015/08/22		171/35	Lake 2015

Table 3.4: Selected dates for Landsat 5 and Landsat 8 satellites for the new combined methodology (see 4.3). Last column to the right lists the denomination used later on in the text.

were selected, assuming that the atmospheric correction is negligible.

For matter of clarity, the eight Landsat images used for the second case study (Section 5.2) are shown in Fig. 3.2 (see Tab. 3.6 for the dates). For this study a second criterion for the images selection was given by the the years belonging to the same climatic condition, meaning coming from periods of droughts or high rainfall years. Referring to the droughts years listed by Kelley et al. [2015] for the Middle East, years preceding droughts periods, therefore showing likely undisturbed conditions, were considered. Taking into account the image availability, that dates back to the 80s for Landsat 5 but with irregular frequency, the earliest available image for all the set is for 30 August 1984, for path 170, that was

Path/row	Date	Satellite
173/38	1984/08/30	
	1990/08/31	Landsat 5
	1998/08/21	
	2003/08/19	
	2013/08/30	Landsat 8

Table 3.5: Selected dates for Landsat 5 and Landsat 8 satellites for the long-term multitemporal change detection in Al Azraq Oasis (see 5.1.2).

Path/row	1984 date	1999 date	2006 date	2015 date	Satellite
170/34 170/35	1984/08/09	1999/08/19	2006/09/07	2015/08/15	
171/34 171/35	1984/09/01	1999/08/10	2006/08/13	2015/08/22	Landsat 5
172/34 172/35	1985/08/10	1999/08/17	2006/08/04	2015/08/13	
173/34 173/35	1984/08/30	1999/08/24	2006/08/11	2015/08/20	Landsat 8

Table 3.6: Selected dates for Landsat 5 and Landsat 8 satellites for the analysis of the case study along the Syrian-Turkish border (see 5.2)
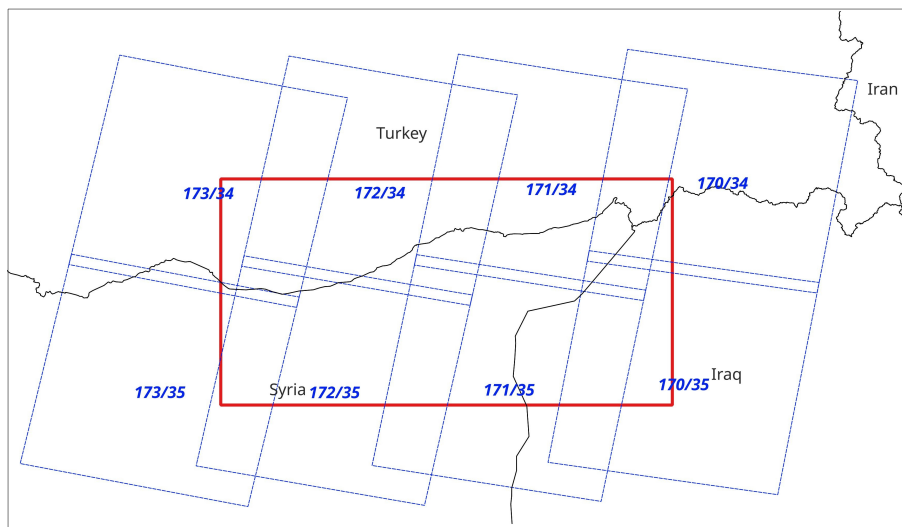
Figure 3.2: Path/row of the eight Landsat scenes used in Section 5.2. The study area is also shown (in red).

combined with images from early September 1984 for paths 171 and 173, and one image from August 1985 for path 172. A first comparison date was chosen in recent years, in summer 2015, for an overall analysis of the change in the available span time.

3.2   Software used

In the present research it was chosen to adopt Free and Open Source Software (FOSS) in Linux environment, where for Geospatial software the acronym GFOSS is commonly used. Several GFOSS tools are grouped under the umbrella of the The Open Source Geospatial Foundation (OSGeo), that was created in 2006 "to support the collaborative development of open source geospatial software, and promote its widespread use". The Foundation promotes an open philosophy and participatory community driven development, ensuring that all the software comply with the Open Geospatial Consortium (OGC) standards. Besides this, OSGEO provides financial, organizational and legal support and "serves as an independent legal entity to which community members can contribute code, funding and other resources, secure in the knowledge that their contributions will be maintained for public benefit" [‡].

In specific, the research made use of Grass GIS software [Neteler et al., 2012] for most of the RS analysis, where BASH scripts were implemented to run several steps in batch mode. The scripts used for the CVA analysis were implemented in the software through a new module available for other users in the Grass GIS addons repository (see Section 4.2). Some analysis were conducted also in QGIS software, as specified later on in the text, as well as the maps created for this research. From QGIS, through the Processing Toolbox, it was also possible to implement the MAD and MAF analysis through the access to Orfeo Toolbox (OTB).

To conclude, the statistical analysis for the TCT calculation was performed in R.

[‡]http://www.osgeo.org/content/foundation/about.html

Chapter 4

Research development and outcomes

4.1 Calculation of a new Tasselled Cap Transform for desert areas

As pointed out by different authors [Ivits et al., 2008; Lu et al., 2004; Mather, 2004], the TCT existing in literature might be used for RS studies worldwide, but particular attention should be paid to the area used for the analysis. Ivits et al. [2008] in particular points out that TCT parameters are sensible to the type of surface (a comparison among soils in Germany and Cameroun is given), and also to the season of the year. Therefore it seems reasonable to broaden the study of Tasselled Cap also to arid-semi arid areas, which have not been taken into account in such kind of analysis in other studies.

The problem of retrieving the transformations coefficients reduces to linear algebra calculations. In practice, two different approaches have been commonly used in literature to perform TCT calculation: Gram Schmidt ortogonalization (GS) [Jackson, 1983] and an implementation of Principal Components Analysis (PCA).

The Gram Schmidt ortogonalization was used originally by Kauth and Thomas [1976]. It consists of a procedure which takes a non-orthogonal set of linearly independent functions and constructs an orthogonal basis, and thus a new set of axis based on this. This method has been used, among others, by [Chang, 1992; Collins and Woodcock, 1994; Ivits et al., 2008; Jackson, 1983].

In the second approach, PCA is used as a firsty step to find orthonormal relations in the data, then a subsequent rotation on preferential axes must be performed, to match some preferential directions on the bands space given by the position of selected categories of surface cover [Crist and Cicone, 1984; Huang et al., 2002a; Yarbrough et al., 2012]. The procedure in fact gives as an output the main directions on which the original data are

spread, that do not correspond a priori to the direction of soil and vegetated areas. There-
fore a rotation on the TCT space must be performed in order to align the PCA axes to
the desired directions. This is the method that has been used by Crist and Cicone in their
research [Crist and Cicone, 1984; Crist, 1985]. Huang et al. [2002b], Liu et al. [2015] and
Yarbrough et al. [2012], who recently (2012) proposed a procedure to improve the deriva-
tion of TCT parameters, also used this approach.

The two techniques face the problem of transformation of bands coordinates with two dif-
ferent approaches. PCA is widely used in statistics as tool to reduce redundancy in the
original data, selecting the portion that bears significance and that explains the highest
variation in the dataset [Liu et al., 2015]. However, in the frame of TCTcalculation, PCA
is used just as a tool to find a preliminary set of perpendicular axes [Crist and Cicone,
1984] and "due to the nature of the Tasseled Cap space, it is serendipitous that the co-
ordinate axes align with the Principal Component space" [Yarbrough and Easson, 2005].
This technique then is more convenient in terms of preliminary work since the calculation
of the initial eigenvalues is an automatic procedure, but it requires further work to next
rotate the PCA axes.

As opposed to this, an advantage of the GS technique is the possibility to look at the
disposition of the data and select a priori the desired directions, allowing to perform a
step-by-step supervised procedure. This point solves an intrinsic problem related with the
TCT calculation for desert images, which tend to be eliminated in the calculation process
performed with PCA mainly for two reasons. First of all, during the preliminary scenes
selection, desert images can give very outlying results in the range of the eigenvalues used
as the first step for the analysis [Yarbrough et al., 2012]. Secondly the disposition of the
image pixels in the Tasseled Cap space represents a critical point since a scene dominated
by sands doesn't show a clearly defined shape in the bands' space. As Huete et al. [1985]
states, in desert scenes "soil and vegetation spectral behavior are somehow correlated and
dependent upon each other", giving a significant decrease in red reflectance with increasing
amount of vegetation over the arid soil types. The soil line and the greenness direction
thus tend to overlap, making difficult for the rotation to match the two axes separately
[Yarbrough et al., 2012].

On the other hand, when using the GS technique the calculation is straightforward after
some basic preliminary steps are performed. In the same time, the iterative procedure
bears an intrinsic nature of propagation of error given by the subsequent approximations.
For this reason the GS technique should only be used when the number of initial bands is
equal or fewer than four, given that the output number of features (n) is expected to be

$n \leq m$, with m equal to the number of initial bands. Considering though that the number of features bearing any significance is just three (see Section 2.1), even in the Landsat case where we do have more input bands, this restriction might be considered satisfied.

In the present research the calculation of new desert-apdapted TCT coefficients the GS method was chosen, as explained in the paper by Zanchetta et al. [2015].

The procedure takes a non-orthogonal set of linearly independent functions and constructs by geometrical projections and subtraction an orthonormal basis, then a new set of axes based on it. The soil line, which gives the Brightness axis, is highlighted from the original n-bands space and the second axis, Greenness, is given by the vegetated pixels' direction orthogonal to the first axis (Fig. 2.2).

The study has been conducted on two different and frequently used families of satellites: SPOT and Landsat satellites. The TCT coefficients were retrieved following the method extensively illustrated by Jackson [1983] using GS orthonormalization. In two dimensional
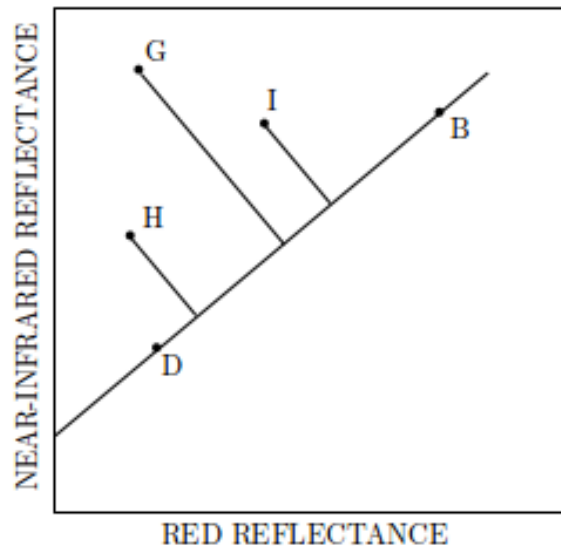
Figure 4.1: Diagram of the soil line and vegetation points in 2-dimensional space, adapted from Jackson [1983].

space, the graphical representation of the process can be schematized as in Fig. 4.1. Every TCT feature (Brightness, Greenness, etc.) is retrieved step by step by algebric calculation, finding m spectral *indices*, whose number is equal to the n number of bands. The GS process bears a problem of error propagation which implies that often only the first few indices are significative, as discussed above.

To compute the first index (in our case the Brightness coefficients) the choice of the direction of the new axes is traightforwards, taking the direction given by the soil line. For the

subsequent indices the procedure requires a bit more of workaround, since they are subject to the condition of being orthogonal one to each other.

Starting from the first index direction, a line through the soil data points must be described, in terms of an equation. From here on, the considerations made by Chang [1992], based on Jackson's work, will be followed to extrapolate from the data the 'best fit' line for soil, vegetation and water characteristic pixels. Two soil points are required, one characteristic of bright soil and one characteristic of dark soil. The simplified representation of their position in the 2-dimensional bands space is shown in Fig. 4.1 as B (bright soil) and D (dark soil). The soil line is given by the difference between the two pixels reflectance:

$$b_i = X_{b,i} - X_{d,i}$$

for each band $(i = 1, 2, ..., n)$, where X_i is the value of the pixel in the i band. The soil line vector $(b_1, b_2, ..., b_n)$ is normalized to define a unit vector by dividing each component by:

$$B = \left(\sum_{i=1}^{n} b_i^2 \right)^{1/2}$$

The first index A_1 is given then by:

$$A_{1,i} = \frac{b_i}{B}$$

These constitute the coefficients for the transformation, namely Brightness will be calculated as

$$Brightness = A_{1,1}X_1 + A_{1,2}X_2 + ...A_{1,n}X_n$$

Once the soil line has been determined, the second index can be retrieved by the identification of a vegetated-pixels direction. For this aim, it has been validated that any vegetation point can be used "and it would make no difference in the final result" [Chang, 1992]. In this research the criterion was to choose the average value of the vegetated (*green*) pixels, X_g. Subsequently a line through the vegetated data points is found as the difference between the vegetated point, point G in Fig. 4.1, and the soil line, assuming that it has no vegetation. The points H and I represent pixels that compared to G have lower vegetation cover and partial soil cover. They have the same distance from the soil line, so have the same vegetative cover, but H is on a wetter surface (less reflective) and I on a drier soil (more reflective).

To determine a vegetation line orthogonal to the soil line, one pixel that is characteristic of the soil must be assigned. Since a single pixel is enough for this purpose, also for the soil the criterion adopted was to take the mean of the pixels' soil values, X_s. The difference

between the green points and the soil points $X_{g,i} - X_{s,i}$ (vegetation line) for each band is then the first step to calculate:

$$g_i = (X_{g,i} - X_{s,i}) - \left[\sum_{i=1}^{n} (x_{g,i} - x_{s,i} A_{1,i}) A_{1,i} \right] = (X_{g,i} - X_{s,i}) - D_{2,1} A_{1,i}$$

Where $D_{2,i}$ is the inner product and the term $D_{2,1} A_{1,i}$ gives the projection of the vegetation line into $A_{1,i}$, ensuring that the vectors $(b_1, b_2, ..., b_n)$ and $(g_1, g_2, ..., g_n)$ are orthogonal. An esemplification of the process in two dimensions is shown in Fig. 4.2.

Again normalization takes place using the normalization factor

$$G = \left(\sum_{i=1}^{n} g_i^2 \right)^{1/2}$$

and the second index A_2 is given then by:

$$A_{2,i} = \frac{g_i}{G}$$

For the third index we proceed in an analogous way, taking the average value of the wet
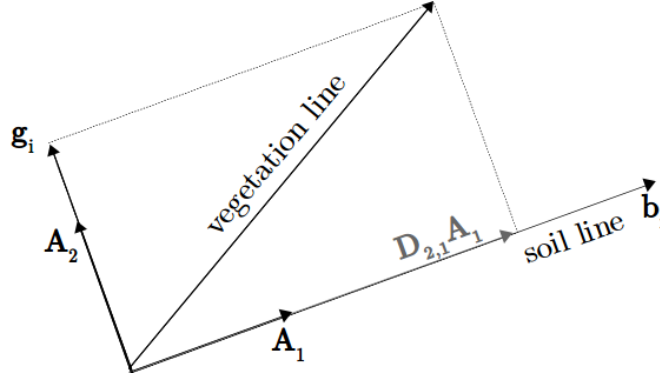
Figure 4.2: Esemplification of the Gram-Schmidt orthogonalization process in two dimensions. $\mathbf{b}_i$ and $\mathbf{g}_i$ are the two orthogonal vectors, $\mathbf{A}_1$ and $\mathbf{A}_2$ are the two components of the orthonormal basis.

cover pixels (X_w), and considering that it must be orthonormal to both Brightness and Greenness. Even though the interpretation of the third axis is not univocal, its direction is an automatic outcome orthogonal to the first two axes, therefore in this research wet area/water pixels have been chosen following the most common reference found [Crist and Cicone, 1984; Huang et al., 2002a; Ivits et al., 2008; Yarbrough et al., 2012].

Starting from the vector of the soil and wet points differences $X_{w,i} - X_{s,i}$, one gets

$$g_i = (X_{w,i} - X_{s,i}) - (D_{3,1} A_{1,i} + D_{3,2} A_{1,i})$$

Where

$$D_{3,1} = \sum_{i=1}^{n}(x_{w,i} - x_{s,i}A_{1,i})A_{1,i}$$

and

$$D_{3,1} = \sum_{i=1}^{n}(x_{w,i} - x_{s,i}A_{2,i})A_{2,i}$$

are respectively the inner products of the soil-wet points vector with the first index $A_{1,i}$, and the second index $A_{2,i}$.

The procedure can involve as many indices as the starting n bands, but for the interests if the research we stop at the third index. The process is performed on a range of images from different seasons and selected geographic locations in the Middle East (Jordan and Egypt), in order to overcome the dependency of the TCT calculation on temporal conditions and location. These criteria allow the use of the new TCT coefficients, both for SPOT and Landsat satellites to perform a LULCC detection against products of previous Landsat and SPOT satellites.

The calculation of desert-adapted TCT coefficients was performed on data images transformed to TOAR. This choice is related to the possibility of comparing the results with the coefficients already existing in literature both for SPOT and Landsat satellites [Huang et al., 2002a; Ivits et al., 2008]. Using surface reflectance data would be the most accurate choice, but still using TOAR data is a reasonable choice [Huang et al., 2002a]. In fact the use of the TCT transform calculated for raw digital numbers (DN) can be problematic, being image affected [Ivits et al., 2008], as pointed out also by Kauth and Thomas [1976]. While for Landsat 4 or Landsat 5 DN coefficients are available, for Landsat 7 just TOAR coefficients are available. Though, a report on MRLC image processing procedure from the U.S. Geological Survey [MRLC, 2001] states that "the standard Landsat 7 processing procedures (including converting DN to at satellite reflectance, tasselled cap transformation, and normalized burn ratio) also apply to Landsat 5 TM images", so when comparing Landsat 5 and Landsat 7 images they should both only be converted either to DN or to TOAR data in order to use the same type of coefficients. In conclusion, for Landsat satellites the choice was to calculate TOAR coefficients for Landsat 5 in order to compare them with the ones calculated by Huang for Landsat 7 satellite, while for SPOT 4 the comparison is possible with the coefficients calculated by Ivits et al. [2008] for SPO T5, given that the two satellites present analogous spectral characteristics.

To address the problem of the seasonal dependency of TCT coefficients, then, it was decided to take for each location as much variation as possible, ranging through seasons and years. Then for each site a combined average set of coefficients was considered taking into

account all the calculated values for that site, by feature and by band.

For SPOT 4 satellite the data chosen for the study are at Top of Atmosphere Reflectance data (Level 1C) from the SPOT 4 – Take5 project website (Section 3.1.1). For the choice of the images, three sites in arid and semi-arid areas in the Middle East (Egypt, Jordan, Tunisia) and one site in Arizona (USA) have been chosen. The Jordanian site is centered in Al Azraq Oasis. The site in Tunisia is centered on the area of the dam Lake of Sidi Saad and the Sebkha Sidi El Hani, another wetland area that is bordering the Sahara Desert in Tunisia. The site in Egypt is not a proper a desert site, since it's located on the coast of the Mediterranean Sea, but has been selected because it belongs to the same climatic region of the first two locations. The image is centered on Lake Burullus, in the Delta of the river Nile. Besides these three sites, considered significant spots for arid and semi-arid areas in the Middle East/Mediterranean region, another location in the Maricopa County in Arizona (USA) was chosen as to add an area with different desert conditions. In order to calculate the coefficients using a variety of geographical conditions and seasons, one image in winter and one in summer were chosen for each location.

Given the restricted time range of the dataset, the date for winter conditions was the earliest and for summer the latest available in the dataset. These dates were different for each location, because of weather conditions and availability of water areas in the surface, both necessary for the calculations (see Tab. 3.3).

For Landsat 5 satellite, two locations were chosen: Al Azraq Oasis (Jordan), as before, and Al Fayoum Oasis (Egypt). The latest is located South-West of Cairo and is formed by the depression of the Lake Qarun (also called Lake Moeris) and the Wadi Al Rayan wetlands, surrounded by an intensively cultivated area. The images available for free download in these locations from the Landsat database were mainly for Landsat 5, while images from Landsat 7 were lacking, and so they were not considered for the research. As for the SPOT satellite, a range of different seasons was chosen to get the maximum possible variability of data but in this case the images could also be chosen in different years.

The main requisite for the selection of the images was the availability of water covered areas on the scene. Three images have been chosen for both locations in similar dates (month and year), dating back to February 1985 and 1986, April and May 1998, and February 1999.

For Landsat 8 satellite, two dates have been selected for the TCT calculation considering the same two locations chosen for Landsat 5. The criterion for the choice of the images was the same followed for SPOT and Landsat 5. Given the lack of good images for these two locations in the restricted life time of Landsat 8 (images available from 2013), another

location in North Tunisia, centered on the capital Tunis, was selected, in order to reach a total amount of six images for the TCT calculation.

The selected images are summarized for both SPOT4 and Landsat 5 in Tab. 3.3.

The initial image processing was performed in Qgis environment, the selected pixels were then imported in Grass GIS to make use of its interface with R software.

In Qgis the images were photointerpretated in order to select the three categories of land cover necessary for the GS process: soil, vegetation and water. For each category 20 squares of 10x10 pixels were selected, thus giving a sum of 2000 pixels for each category. This threshold was chosen referring to the studies of Yarbrough et al. [2012], while the choice of taking 20 squares to add up to the threshold was given by technical reasons related to the software used for the calculations. Fig. 4.3) shows the preliminary work that has been carried out on the images (visualization of the areas and photointerpretation) in QGis for all the locations in different years (a zoom of the image for Al Fayoum area for Landsat 5 is shown as an example). After the preliminary pixels selection, the procedure
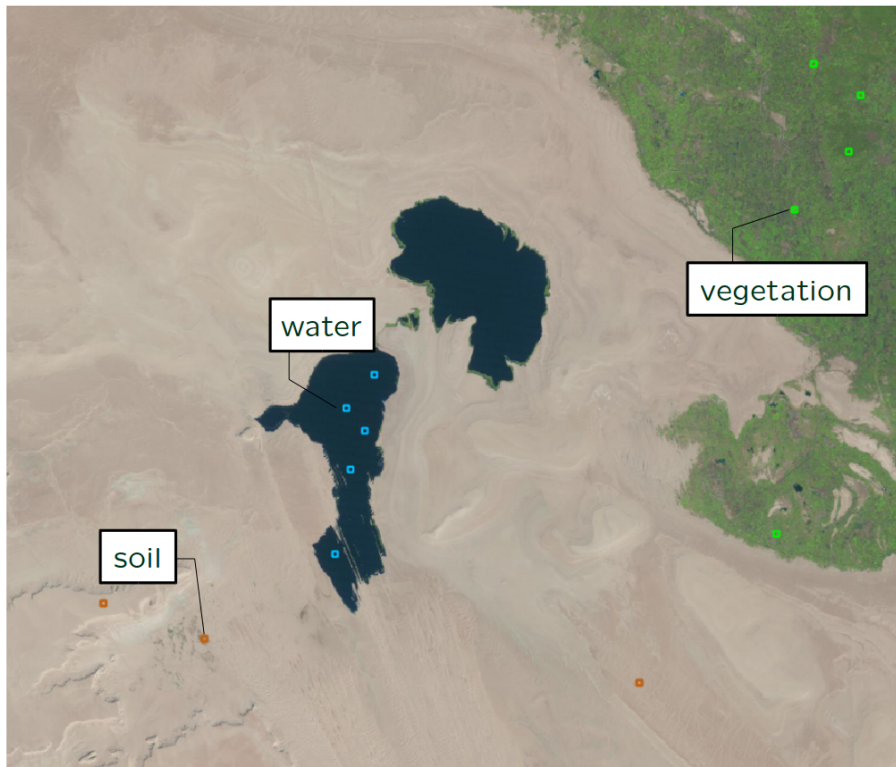
Figure 4.3: Example of the selection in Qgis of 20 squares of dimension 10x10 pixels for the three soil cover categories for the GS process. The background is the look-like image of Al Fayoum (Egypt) of 1986/11/04 for Landsat 5.

described above for performing the GS process was applied. The subsequent analysis was

performed using Grass-GIS software (including DN to TOAR transformation for Landsat images), which enabled writing several BASH scripts able to call the commands in batch mode for multiple images. The statistical analysis was performed in R for each location and each year. The script calls the Grass-GIS region and performs at first the upload of each single "square" for each image. A subsequent categorization by the land cover categories is performed through a filter on the squares' name, giving three different datasets. These are then treated as matrices for the GS process, that is performed following the steps described above. See Appendix B for the R script, with the case of Jordan for Landsat 8 TCT calculation as en example.

The output is a set of coefficients for TCT for each image (date and location), that

	B1	B2	B3	B4
Brightness	0.307	0.495	0.583	0.562
Greenness	-0.217	-0.357	0.800	-0.406
Wetness	0.445	0.523	-0.004	-0.714

Table 4.1: TCT coefficients for SPOT4 satellite for TOAR data in Egypt.

	B1	B2	B3	B4
Brightness	0.387	0.522	0.623	0.435
Greenness	-0.133	-0.297	0.740	-0.584
Wetness	0.347	0.593	-0.237	-0.680

Table 4.2: TCT coefficients for SPOT4 satellite for TOAR data in Jordan.

	B1	B2	B3	B4
Brightness	0.289	0.491	0.531	0.624
Greenness	-0.259	-0.236	0.825	-0.410
Wetness	0.585	0.473	0.011	-0.646

Table 4.3: TCT coefficients for SPOT4 satellite for TOAR data in Tunisie.

were then averaged for each location. The results are shown in Tab. 4.1, 4.2, 4.3, 4.4 for SPOT 4 satellites, in Tab. 4.5 and 4.6 for Landsat 5.

The results exhibit indeed a variation both among seasons and sites (intra-seasonal variation is not shown here), even if all the sites are located in an arid and semiarid environment. This fact supports the thesis that TCT varies by season and by site. In particular the largest variation in the values by band is in the second and third feature (Greenness and Wetness,

	B1	B2	B3	B4
Brightness	0.391	0.517	0.470	0.571
Greenness	-0.249	-0.426	0.852	-0.144
Wetness	0.473	0.330	0.190	-0.779

Table 4.4: TCT coefficients for SPOT4 satellite for TOAR data in the USA.

	B1	B2	B3	B4	B5	B7
Brightness	0.247	0.347	0.426	0.472	0.477	0.422
Greenness	0.141	0.090	-0.064	0.721	-0.318	-0.564
Wetness	0.399	0.493	0.463	-0.435	-0.341	-0.224

Table 4.5: TCT coefficients for Landsat 5 satellite for TOAR data in Egypt.

	B1	B2	B3	B4	B5	B7
Brightness	0.166	0.287	0.398	0.477	0.549	0.448
Greenness	-0.040	-0.032	-0.147	0.846	-0.075	-0.455
Wetness	0.183	0.451	0.680	-0.123	-0.464	-0.262

Table 4.6: TCT coefficients for Landsat 5 satellite for TOAR data in Jordan.

see Fig. 4.4 and 4.5). This might be due to the error propagation connected with the GS orthonormalization, but it's more likely due to the visual interpretation of vegetated and wet areas selected in the calculation process. These two categories in fact could vary from agricultural areas to natural vegetation in the Oasis for Greenness, likely including difference in type of vegetation when ranging from USA to Jordan and Mediterranean conditions. Wetness' pixels instead could range from deep water in dam lakes (Tunisia) to swallow and sometimes salty water in the oasis environment.

A comparison with the previous calculated coefficients for non-desert areas was done plotting the coefficients values together in a scatter plot, using as comparison the range (minimum and maximum value) exhibited by band and by feature among all the calculated values (Fig. 4.4 and 4.4). No other statistical parameters were taken into account, given the low number of samples available.

Comparing the results to the old coefficients, the same pattern is shown for each feature when moving through the different bands, both for SPOT and for Landsat satellites. For SPOT 4 satellite in particular the non-desert value lies within or very close to the range of values for the new coefficients.

 What happens for Landsat 5 satellite is a different trend for each feature. The Brightness
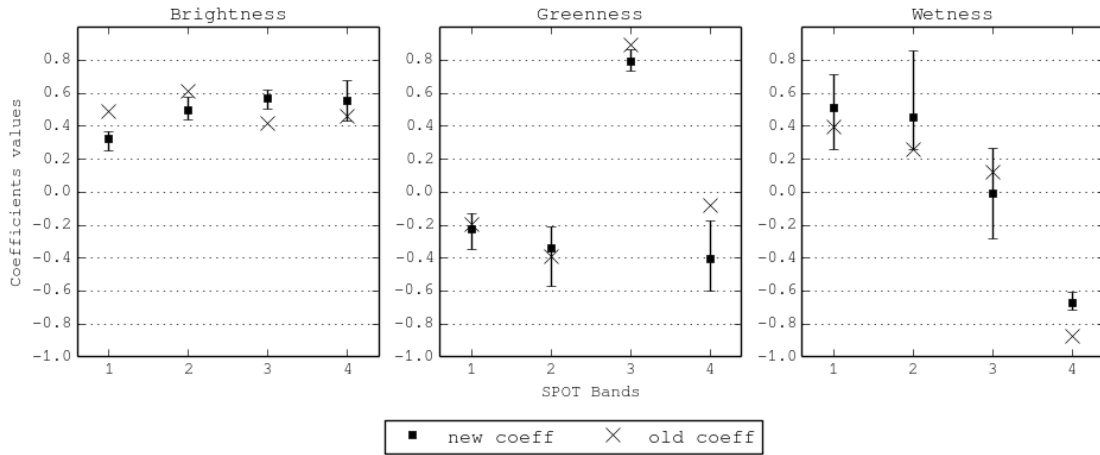
Figure 4.4: Comparison of TCT coefficients values Brightness, Greenness and Wetness for SPOT 4 and 5 for TOAR data: desert conditions coefficients (*New coeff*) are shown with the range of minimum-maximum calculated values. Non desert conditions coefficients (*Old coeff*) are from Ivits et al. [2008].
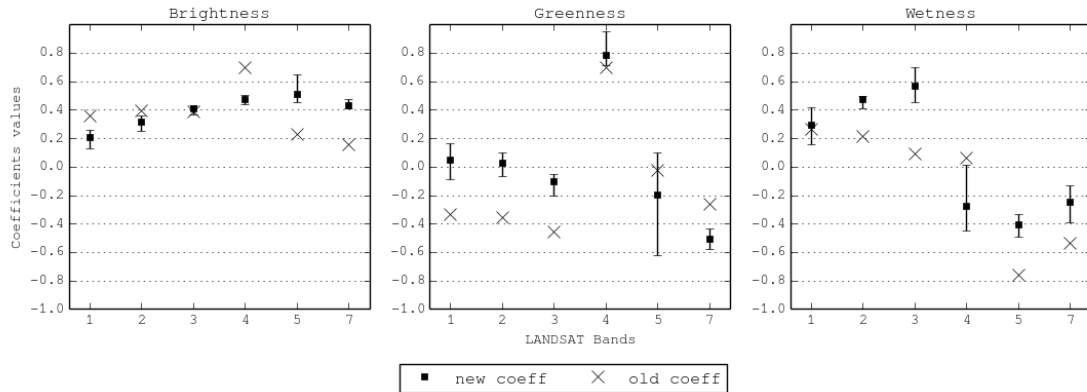
Figure 4.5: Comparison of TCT coefficients values for Brightness, Greenness and Wetness for Landsat 5 and Landsat 7 for TOAR data: desert conditions coefficients (*New coeff*) are shown with the range of minimum-maximum calculated values. Non desert conditions coefficients (*Old coeff*) are from Huang et al. [2002a].

parameters have values quite similar to the old ones for the first three bands (Blue, Green and Red) but up to 0.2 difference in magnitude in the last three bands. Since Landsat 5 band 4 is centered in the NIR and is indicative of vegetation on the surface, a lower value in desert conditions might be explained by the lower reflectance values that are characteristic to stressed and desert vegetation in this spectral interval. Relating to this phenomena and as expected, the correlation between soil and vegetation spectral behavior in desert scenes seems to affect the vegetation reflectance [Huete et al., 1985], as is the case for the values

of band 1, 2 and 3 (respectively Blue, Green and Red) of the Greenness feature, where the higher values can be explained by the fact that "the soil surrounding vegetated areas tends to overwhelm the vegetation signal by saturating the sensor's detector" [Yarbrough et al., 2012]. The higher values in bands 5 and 7 for Brightness might be explained by the spectral behavior of low moisture content soils in those spectral intervals.

For Wetness we can recognize the same trend for both satellites in the behavior of the new coefficients compared to the old ones: higher values in the Visible region (bands 1 and 2 for SPOT, bands 1, 2 and 3 for Landsat), lower value in the NIR band (3 for SPOT, 4 for Landsat) and again higher values for SWIR bands (4 for SPOT, 5 and 7 for Landsat). The behavior in the Visible region is likely due the spectral signature of shallow and not clear water (as is the case of a wetland area like the Oasis), that normally exhibits in this spectral interval higher reflectance values than clear water surfaces.

To obtain a single set of coefficients for each satellite, a combination of the ones obtained for each location was taken, again as an average of the values calculated for each band and feature. The final tables for the new TCT coefficients are shown in Tab. 4.7, 4.8 and 4.9. Regarding Landsat 8 coefficients, they are simply shown here, without a comparison with previous ones, whose use for RS studies has not been yet investigated enough in literature.

	B1	B2	B3	B4
Brightness	0.321	0.499	0.570	0.556
Greenness	-0.227	-0.338	0.793	-0.403
Wetness	0.508	0.453	-0.009	-0.675

Table 4.7: Desert adapted TCT coefficients for SPOT4 satellite for TOAR data.

	B1	B2	B3	B4	B5	B7
Brightness	0.207	0.317	0.412	0.475	0.513	0.435
Greenness	0.051	0.029	-0.105	0.784	-0.196	-0.510
Wetness	0.291	0.472	0.572	-0.279	-0.402	-0.243

Table 4.8: Desert adapted TCT coefficients for Landsat 5 satellite for TOAR data.

	B1	B2	B3	B4	B5	B6	B7
Brightness	0.185	0.206	0.316	0.403	0.478	0.491	0.418
Greenness	0.075	0.080	0.020	-0.180	0.771	-0.349	-0.425
Wetness	0.250	0.264	0.400	0.529	-0.289	-0.433	-0.246

Table 4.9: Desert adapted TCT coefficients for Landsat 8 satellite for TOAR data.

4.2 *i.cva*, a module to implement Change Vector Analysis in Grass GIS

A Grass-GIS addon, *i.cva*, was developed and made available for Grass GIS 7.0.x. The Grass addons are available at the software website for the download and installation *.

i.cva gives in output three images, one of the CVA magnitude and two of the CVA angle between two dates, The first angle map is unclassified (it has values between 0 and 360), while the second one is classified by the four quadrants, as an option for the user.

A threshold can also be specified, either by a statistical criterion (number of standard deviation to be summed to the average) or by a customary value. In the case a threshold is set, *i.cva* gives as output also a map of the final change, given by the classified pixels whose value exceeds the threshold for the magnitude.

For a complete explanation of the addon, refer to the HTML manual page, available online and with the script, once installed. For the Python script code refer to Appendix A.

4.3 Combination of MAF and CVA for change detection analysis in desert areas

For this research, the use of two semi-automated techniques have been investigated: Change Vector Analysis (CVA), and Multivariate Alteration Detector (MAD). CVA was developed by Malila and Lafayette [1980] to investigate vegetated areas, and was performed by us on the Tasselled Cap Transform (TCT) features of Brightness and Greenness. MAD was implemented by Nielsen et al. [1998], and is a technique broadly used for image analysis also in other fields. As in the work of Nielsen, it was here used in junction with Maximum Autocorrelation Factor (MAF) components.

The aim of the research is to reduce the weakness of unsupervised techniques, mainly absence of ground truth information, by the joint use of two of these techniques in a hybrid approach, thus introducing a new and reproducible change detection procedure. In spe-

---

*https://grass.osgeo.org/download/addons/

cific, the effectiveness of a combination of CVA and MAD/MAF is investigated in change detection studies in arid and semiarid areas, naturally prone to desertification processes. Two case studies have been chosen in arid and semiarid areas following the Koppen climate map (see Fig. 1.1), where arid areas (BW) and semiarid areas (BS) are defined based on a combination of mean annual precipitation and mean annual temperature [Peel et al., 2007]. The first case study is Al Azraq Oasis, in Jordan. The second case study is the lake originated by the South Hasakah Dam, in North East Syria, built 25 km South of Al Hasakah in the late 90s on the Khabour River (see Fig. 1.4) [Hole, 2009; Nguyen, 1986].

The two sites, which locations are shown in Fig. 4.6 are characteristic of desert environment and both present water bodies and vegetated areas, mainly agricultural. In the case of Al Azraq, the area surrounding the Oasis shows also natural vegetation growing around the water sources.

For Al Azraq Oasis the information on the ground were given by historical maps, aerial photographies and personal communications collected during a field visit, as discussed in Section 5.1 [Zanchetta et al., 2016]. This study includes a change detection analysis using some of the same techniques (CVA, TCT), and so the confrontation with the new methodology was direct. Several Landsat satellites images were chosen before and after the 90s to assess the expected change in the two areas: in the first case the drying out of the Oasis and in the second case the appearance of the Lake.

In order to reduce dissimilarities in the atmospheric and weather conditions in situ, the criteria for the choice of the images are based on similar acquisition dates and summer season. Therefore images in the end of August 1984 and August 2015 were selected for the change detection analysis. The chosen images are listed in Tab. 3.4, alongside the denomination that will be used to refer to them in the rest of the paper.

4.3.1 Validation of the combined methodology

The images for both 1984 and 2015 have been processed in Grass GIS using two different regions around the Azraq Oasis and the South Hasakah Lake (see Fig. 4.8 A and 4.9 A for 1984, and 4.8 and 4.9 for 2015 images). The raw DN images were firstly transformed to TOAR data with i.landsat.toar, and then to TCT features. The transformation of the TOAR images to TCT features is carried out through Grass GIS BASH scripts encompassing the desert-specific coefficients.

CVA is then performed through *i.cva* in Grass GIS on the Brightness (in abscissa) and Greenness (in ordinate) maps for both dates, taking as a threshold one standard deviation.

Figure 4.6: Location of the two case studies (grey stars) in Syria and in Jordan in the Middle East region.

The outputs of CVA are shown in Fig. 4.8 C, D, E and 4.9 C, D, E separately for the two case studies, where the angle, magnitude and the final change maps are given.

In parallel, MAD/MAF analysis between the 1984 and 2015 images was performed in QGIS on the same areas, using the bands listed in Tab. 3.2, to respect the spectral correspondence between the pairs of bands from each satellite. MAD and MAF transformations can be performed in GFOSS using Orfeo Toolbox, available in QGIS environment via the Processing Toolbox. The subsequent processing of the images was conducted in Grass GIS. The research passed through several combinations and tested them on the Oasis case, prior to extensively testing the chosen methodology. Hence an application on the Lake case was carried out. As a first attempt, a combination of CVA and MAD was considered. The first step was the comparison of several RGB combinations of MAD components in QGIS, in order to select the ones that visually detect the expected change on the surface (Fig. 4.8 F), as commonly performed in MAD application studies. The components 1, 5 and 6 were selected, and then imported in Grass GIS where the $\pm 2\sigma$ threshold was applied to each of the three MAD components, giving in output a map of positive and negative values beyond the threshold.

At this point, a visual correspondence was noticed between the CVA results and the thresholded MAD image, where the positive values are generally correlated with the first and forth quadrant (therefore positive Brightness) of the CVA, while the negative values are correlated with the second and third CVA quadrant (therefore negative Brightness). To make this more clear, a new map was created with only two raster categories, grouping all positive values to one and all negative to another (see Fig. 4.8 G for the component 5 as an example). To quantify the similarity between the maps, analogous to visually overlapping the maps, the Grass GIS *r.cross* module was used, between CVA and two components of MAD. *r.cross* creates an output raster map representing all unique combinations of category values in the input rasters, and outputs also a table summarizing the occurring categories. The number of possible combinations (not shown here) was still large, and their interpretation was not straightforward.

With reproducibility in mind then, the combination MAD-CVA is not satisfying, as it depends on the choice of the number and orders of the significant MAD components, that can differ from case to case. Moreover, the high amount of unique combinations between the MAD and CVA classes leaves a complex classification, rather than an easy-to-interpret change map.

Next, the option of the transformation to MAF variates was considered. Like with MAD components, the results contained a high degree of detail, but the meaning of the change was not yet clear (Fig. 4.8 H). The first MAF variate (MAF1), which was imported in Grass GIS and visually compared with the CVA change map, showed a high spatial agreement. It was therefore taken as the only input for the combined methodology. Higher order MAF variates are not shown here but mostly contained noise, as expected.

Like done with MAD, the MAF1 was subsequently thresholded, considering values higher and lower than $\pm 2\sigma$, and then reduced to a binary valued map grouping positive and negative values (see Fig. 4.8 I). The selection of a single variate as an input alongside the CVA map to *r.cross*, reduced the number of unique combinations, and now the meaning of the CVA classes could be simply attributed to the MAF1 values. The *r.cross* categories results (in terms of percentage and number of pixels) are shown in Tab. 4.10, where the semantic interpretation is retained from the CVA categories (as seen in Fig. 2.5).

 In terms of surface cover the CVA detects more changed pixels, with an extension up to two or three times more than MAF in some specific classes (see the Bare soil and bare sand expansion class, with more than 5% pixels undetected from MAF, out of 6.93% of the CVA). On the other hand, pixels identified by MAF, but not considered from CVA, cover in total only 0.58% of the Oasis area.

	CVA classes	MAF 1 values	Oasis		Lake	
			%	# pixels	%	n. pixels
1	No data	Negative	0.31	990	0.19	1043
2		Positive	0.27	857	0.04	200
3	1st quadrant	No data	0.21	685	0.03	143
4	(Moisture reduction)	Negative	0.01	39	0.03	182
5		Positive			0.00	1
6	2nd quadrant	No data	1.73	5551	0.52	2808
7	(Chlorophyll increase)	Negative				
8		Positive	2.63	8427	1.37	7406
9	3rd quadrant	No data	0.44	1420	3.19	17215
10	(Higher moisture land	Negative				
11	and water bodies)	Positive	0.12	390	1.83	9882
12	4th quadrant	No data	5.05	16172	0.68	3645
13	(Bare soil and bare	Negative	1.88	6015	4.16	22480
14	sand expansion)	Positive				
15	No data	No data	87.33	279454	87.96	474995
		TOTAL	100	320000	100	540000

Table 4.10: Results of Grass GIS *r.cross* module between CVA map and MAF map (first component thresholded and classified) in terms of pixels count (n. pixels) and percentage over the study area for both case studies.

A comparison with the results of a previous CVA change detection analysis, carried out in the same study area and in the same time interval with similar conditions was visually performed ([Zanchetta et al., 2016], as described in Section 5.1.2). The major difference between the use of the CVA alone and its use combined with MAF is given by the lesser spatial extent of the detected change, as shown by the results in Tab. 4.10 The change classes are correctly detected, but CVA tends to overestimate the change, detecting wider areas, especially in the Bare soil expansion class (see Northwestern and Western part of the study area). The combined technique shows more precise identification of the surface elements who changed, in particular the pools and ditches on the East side of the Oasis who went through a drying out process.

The high correspondence of the CVA and MAF results, together with the improvement in the CVA spatial detection, induce to propose the combination of the two techniques as a new methodology for change detection studies, where CVA gives the semantic interpreta-

tion and MAF the spatial extent of the change (Fig. 4.8 J).

Considering the new methodology valid, an application to the second case study was implemented, in order to evaluate an antithetical situation, of water replenishment in a semiarid area. The steps performed in the Oasis case were repeated in the second case, as shown in Fig. 4.9 C-J. Also in this case, the MAD components 1,5 and 6 were chosen for the analysis, but the MAD and CVA combination showed the same weak points seen before. The MAF1 visually exhibited a high spatial correspondence and the Grass GIS *r.cross* module was applied, giving the results shown in Tab. 4.10. The possible combinations were the same seen for the Oasis case, with one stray pixel matching the first CVA quadrant with the positive MAF1. Like in the Oasis case, MAF results are almost entirely overlapped by CVA, with a missed detection of just 0.23% of the image (compared to the 0.58% of the Oasis area).

A visual interpretation of the results indicates that the combined methodology finds the abandonment of the fields areas South of the dam along the river banks, and again the MAF reduces the spatial extent of the CVA bare soil expansion class. The expected occurrence of a new vast water basin upstream the dam in the North is also correctly detected. However the MAD/MAF contribution eliminates from the change map the central part of the basin, that was correctly detected by CVA (3.19% of pixels, belonging to the Higher moisture land and water bodies, not detected by MAF). This issue could be possibly solved if considering higher order MAF variates, and this could be discussed in further work.

Summarizing, the MAD/MAF finds an equivalent change to the CVA and at the same time the CVA allows the physical interpretation of MAD/MAF technique. This gives a new prospective for the use of MAD/MAF, since in other cases found in literature the interpretation of the results is always dependent on the image considered as a case study. The research shows that the use of the two unsupervised techniques in a hybrid approach allows an improvement in understanding the results of both.

For clarification on the performed steps, the proposed workflow for the combined methodology is displayed in Fig. 4.7.
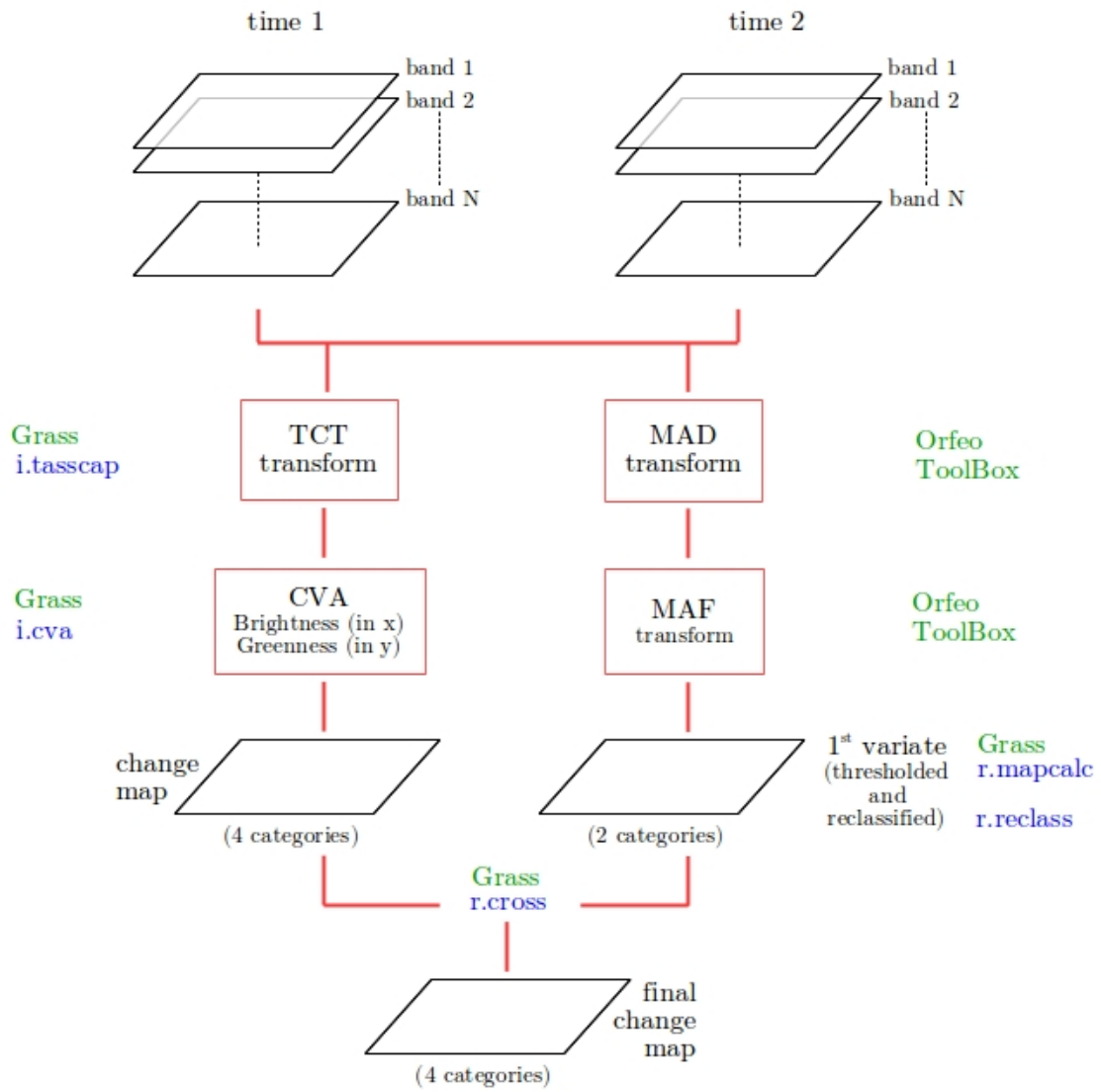
Figure 4.7: Proposed workflow for the new combined methodology. In green the name of the software used, in blue the Grass GIS modules.

CVA legend: ■ 1ˢᵗquadrant ■ 2ⁿᵈquadrant ■ 3ʳᵈquadrant ■ 4ᵗʰquadrant
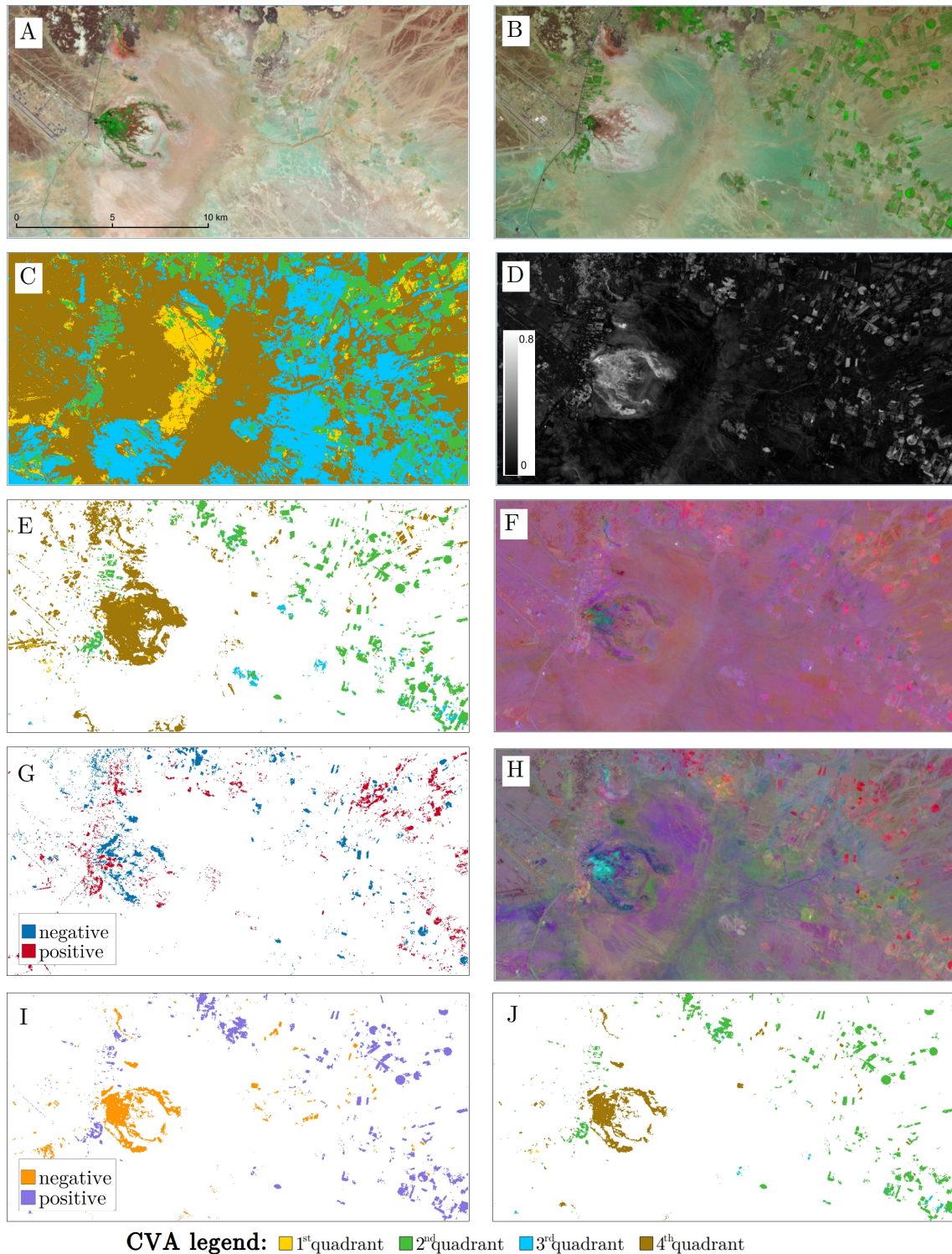
Figure 4.8: Processing of the images for the combined procedure for Al Azraq Oasis. A. RGB composition of Landsat 5 image for 1984; B. RGB composition of Landsat 8 image for 2015; C. CVA classified angle map (legend is shown below for all the CVA maps); D. CVA magnitude map; E. CVA final change map; F. RGB MAD map (components 1,5,6); G. MAD component 5 thresholded and classified map; H. RGB MAF map (components 1,2,3); I. MAF component 1 thresholded and classified map; J. Final change map. For the colors meaning refer to Fig. 2.5.
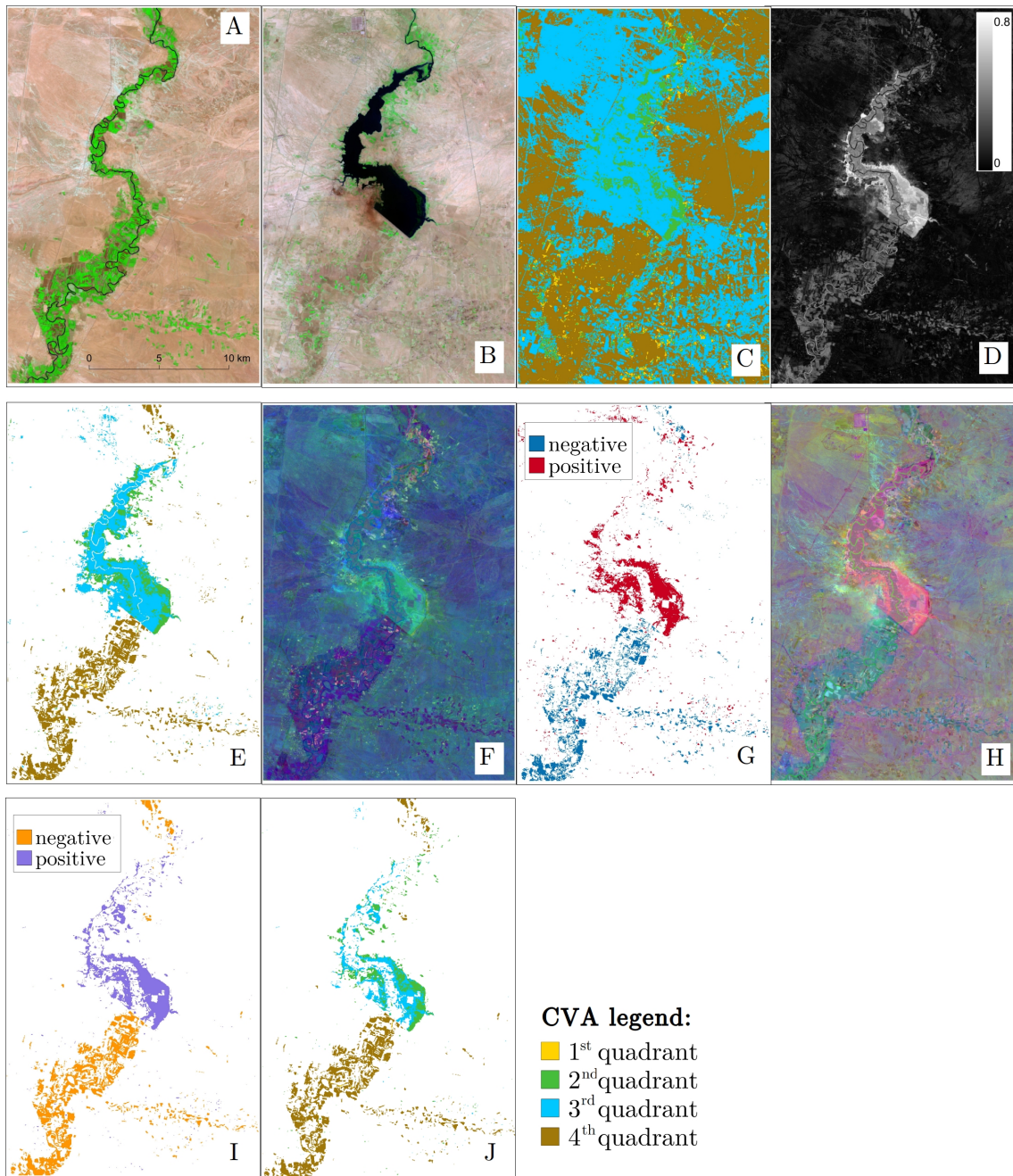
Figure 4.9: Processing of the images for the combined procedure for South Hasakah Lake Oasis. A. RGB composition of Landsat 5 image for 1984; B. RGB composition of Landsat 8 image for 2015; C. CVA classified angle map (legend is shown below for all the CVA maps); D. CVA magnitude map; E. CVA final change map; F. RGB MAD map (components 1,5,6); G. MAD component 5 thresholded and classified map; H. RGB MAF map (components 1,2,3); I. MAF component 1 thresholded and classified map; J. Final change map. For the colors meaning refer to Fig. 2.5

Chapter 5

Case studies and results

In the present chapter the discussion of the application of RS change detection techniques to two case studies is performed. At first a detailed description of the study area is given, for both cases, then several analysis are carried out, on different time scales and for different purposes.

The chosen analysis follows the research flow, that at first tested the CVA on a short term (seasonal interval) in Al Azraq Oasis for SPOT satellites, with the employment of new TCT coefficients for desert conditions. A subsequent application to a longer term (decadal, 30 years) is then addressed, in the same study area and with the application of the new TCT coefficients for Lansat 5 and Landsat 8 satellites.

The last analysis is carried out in the Jezira region, where a cross-border comparison is performed through CVA applied to TCT and MAD/MAF components, combined in a new change detection methodology.

5.1 Depletion of Al Azraq Oasis (Jordan)

Before drying up in the 90s, Al Azraq Oasis was made up of two main groups of springs surrounded by marshes: the Aura and Moustadhema springs surrounded by the Druze Marsh in the Northern part, and the Souda and Qaisiyah Springs surrounded by the Shishan Marsh in the South [Ramsar Convention, 1990a]. The springs and the marshes created a seasonal cycle with the nearby *Qa'* or *Sebkha*, the Arabic terms to refer to a mudflat, also called 'salt flat' or 'playa lake' [Alvarez Cobelas et al., 2005]. The mudflat consists of a depressed area that is flooded during the winter season by the drainages from incoming streams (wadies) and then dries up due to the dry climate, creating temporary salty water ponds and swamps until the water evaporates [Cordova et al., 2013].

Object in the 60s of several study campaigns, mainly by ornithologists and desert researchers [Green, 1995; Mountfort, 1965; Nelson, 1973; Scates, 1968], Azraq Oasis started to gain attention far before the complete drying up of the sources in the 90s: a first draft of the Natural Reserve was drawn as early as 1965. Later, in 1977 Jordan designated the Azraq wetland for the List of Wetlands of International Importance under the Ramsar Convention, an international agreement established in 1971. The Member States of the Convention commit to protect and preserve the wetlands that are enlisted in the agreement (the "Ramsar Sites" across the world are more than 2000 for 160 Contracting Parties). Also thanks to the Ramsar Recommendations, which are periodically provided during the Ramsar Meetings, the Natural Reserve was finally instituted in 1978, under the jurisdiction of the Royal Society for Conservation of Nature (RSCN) which got the mandate from the Ministry of Agriculture.

In 1980, a special cabinet committee created to establish a plan of action, assessed the safe yield at 20 MCM; in the meantime the Amman Water and Sewage Authority (AWSA) set up a governmental wellfield for domestic use abstraction, and during the 80s the pumping from the Oasis kept on growing, despite the calls from Ramsar Recommendations to reduce it at least by 50%, as by Ramsar Convention [1987, 1990b] and personal communications. Eventually the sources dried up completely in 1992 and this led to a Global Environment Facility (GEF) funding of a three-year project aimed to restore and manage the Azraq Wetlands Reserve. This resulted in a variety of management activities during 1994-1999, including the opening of a Visitors Center (active from 2000) and a guided natural trail through the Reserve, together with the return of a supply of water to the Shishan Marshes from June 1994, following lack of water for two years. In 1998 the artificial water supply started to be pumped bypassing the former springs (Souda and Quasiya), where a large amount of water was being lost through infiltration, and transported directly to the central marsh [Ramsar Convention, 1999].

5.1.1   Short term (seasonal) analysis of Al Azraq Oasis

The short term analysis was performed on SPOT images from the SPOT4-Take5 project, taking images with the maximum time spread possible in the database. Therefore an image from February 2 (considered winter) and one from June 9 (summer) where chosen (see Tab.3.3). The study was a first test to evaluate the efficacy of the new desert-adapted TCT in detecting the change compared to the old coefficients available in literature [Ivits et al., 2008]. Results of the comparison are shown in Fig. 5.1.

The February and June images are the RGB representation of the SPOT bands 1, 2 and 3.
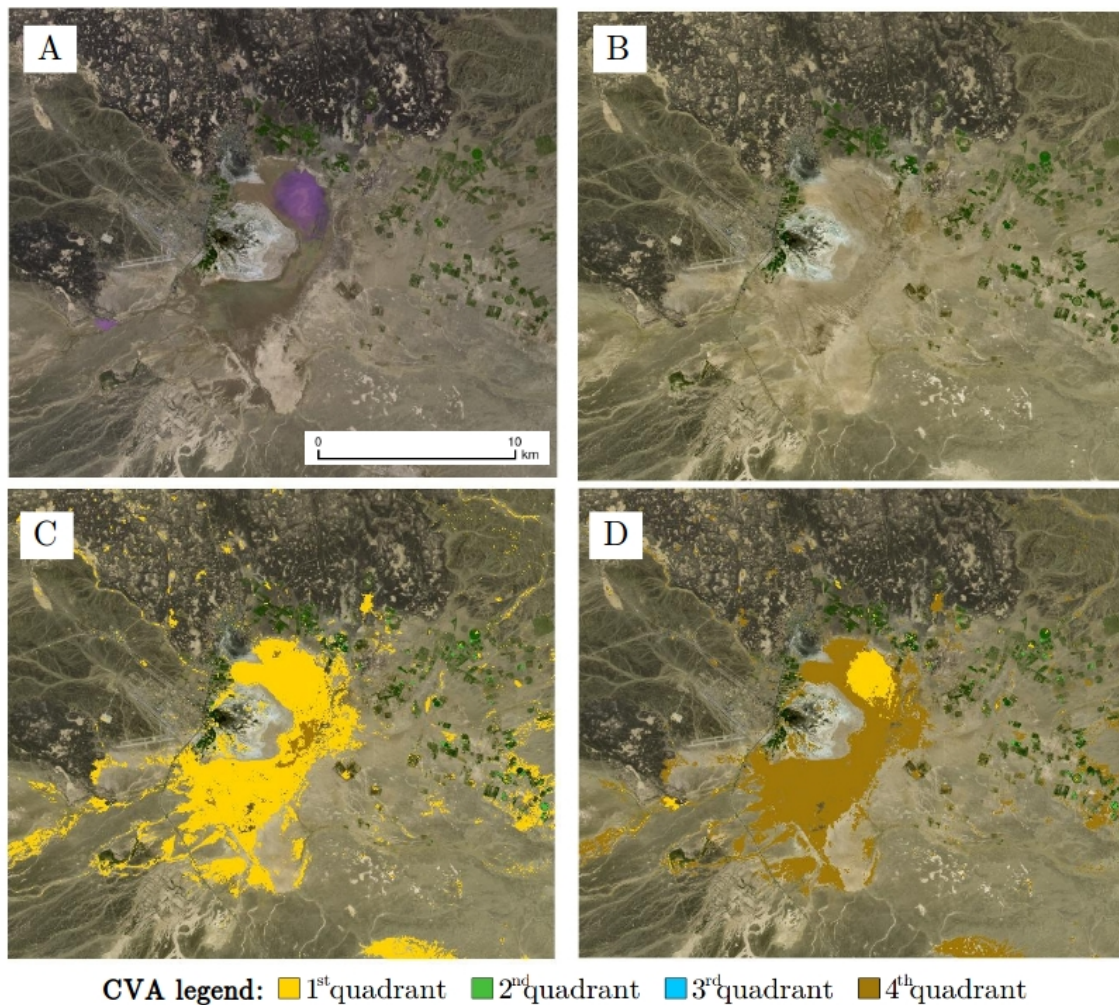
Figure 5.1: Comparison of new and old SPOT satellite TCT coefficients for CVA in Al Azraq Oasis area. A. RGB image for February; B. RGB image for June; C. CVA analysis with the old coefficients [Ivits et al., 2008]; D. CVA analysis with the new coefficients. For the CVA legend refer to Fig. 2.5.

Since SPOT4 satellite misses the blue band, what we see in purple color approximately in the center of the image is a pond of water originated from seasonal rainfall in the mudflat area, surrounding the Oasis (to the West) with a C shape (see Section 1.3). It's evident from the summer image that this area underwent a process of drying out in the occurred interval.

The visual comparison of the CVA results shows indeed a general drying out of the area of mudflat area with both the new and old coefficients. However, while the old coefficients detect mainly a change towards Moisture reduction (in yellow), the new desert-adapted coefficients are more effective in distinguishing the change in the water pond (the circular purple spot). In fact, as seen in Section 2.2, the CVA category Moisture reduction in desert

areas is associated to drying of lakes/salty water surfaces.

The spatial extension of the changed area is similar with both sets of coefficients, but the new coefficients differentiate between Moisture reduction (in yellow) and Bare soil expansion (in brown). The results corroborate the hypothesis that desert-adapted coefficients are more suitable for LULCC detection in arid and semiarid areas.

5.1.2   Long term (decadal) analysis of Al Azraq Oasis

Before performing CVA on the selected dates, a visual interpretation of images was carried out in order to visualize the expected change between the pre-drying up conditions and the present conditions. As a reference for the pre-event situation, a map from 1979 was digitized and georeferenced (see Fig. 5.2).

The map is available from the 1990's RAMSAR Report and it contains also some handwritten updates from an expedition organized by the RAMSAR committee in March 1990 [Ramsar Convention, 1990a]. The annotations describe a general deterioration of the Oasis: stressed or tainted vegetation in the central area of the marsh (on dunes and water) and low water level in the pools, with the Ingilesi pool almost dry and the ditches totally dry. As a reference for the present conditions, missing ground truth data, a comparison with updated base maps available on-line (OpenStreetMap, Google) was taken in consideration (Fig. 5.3).

Further help for interpreting the intermediate dates comes from aerial pictures available from the APAAME online catalogue (Aerial Photographic Archive for Archaeology in the Middle East), that dates from 1998 to present. The visual comparison over the entire time span shows indeed a deterioration of the general status of the Oasis area, while rural areas on the North-East part of the plateau seem to flourish. These impressions were confirmed during a field visit in June 2014.

CVA was performed in Grass GIS on the TOAR transformed images for selected Landsat scenes between 1984 and 2013 (see Tab.3.5). The CVA image resulting from the comparison between 1984 and 2013 is given in Fig. 5.4-a and -b, where Landsat look-like images are also shown. The highest change occurs in the Bare soil expansion category, which accounts for more than 80% of the total changed pixels (see Tab. 5.1). A Bare soil expansion was detected in and around the Reserve area, while Chlorophyll increase/regeneration and Moisture increase were detected in the Eastern side and around the mudflat area, with clear identification of agricultural fields (Fig. 5.4-e).
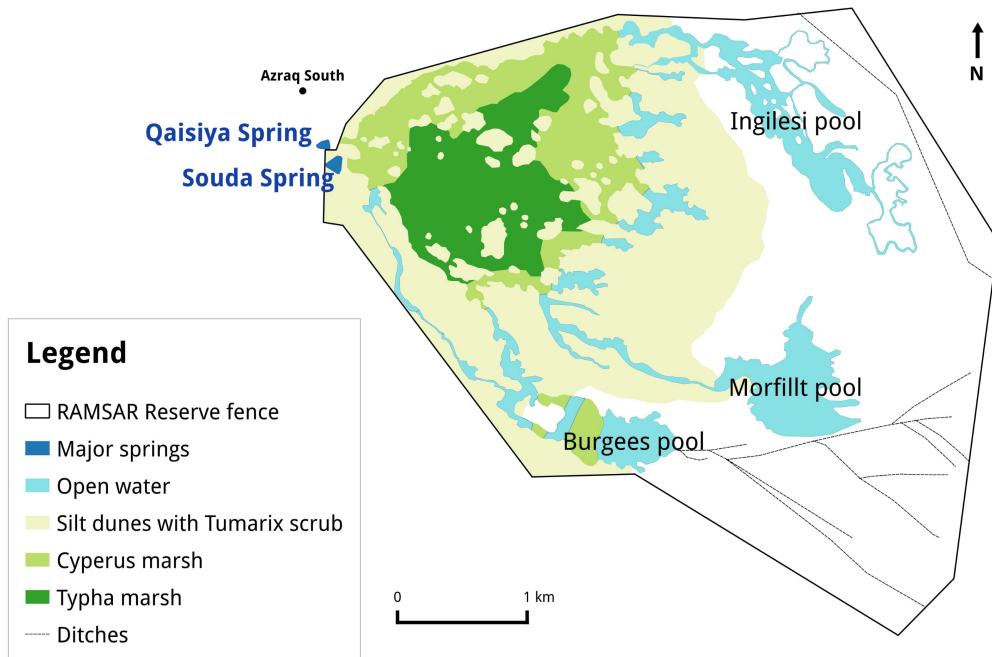
Figure 5.2: Major habitats/vegetation communities in Azraq Wetland Reserve, digitization of a 1979 map. (Source: Ramsar Convention [1990a])

Figure 5.3: Google Earth image of the Azraq Reserve in 2015, 1979 RAMSAR fence (in black) is shown.

CVA classes	1984-2013		1984-1990		1990-1998		1998-2003		2003-2013	
	km^2	%	km^2	%	km^2	%	km^2	%	km^2	%
Moisture reduction	0.2	0.02	6.34	2.96	26.65	2.99	26.54	2.98	0.02	0.00
Chlorophyll increase	10.2	1.14	28.43	3.19	29.00	3.25	34.67	3.89	4.58	0.51
Moisture increase	3.1	0.35	11.76	1.32	19.46	2.18	13.67	1.53	1.93	0.22
Bare soil expansion	76.8	8.62	30.81	3.46	21.83	2.45	11.21	1.26	83.71	9.39
Area changed	90.3	10.13	97.33	10.93	96.93	10.87	86.09	9.66	90.23	10.12

Table 5.1: CVA results for the studied time periods in km^2 and % on the total study area. For the meaning of the categories refer to Fig. 2.5.

The long-term trend is replicated in the shorter term periods, where the highest change occurs in the Bare soil expansion category with a maximum in the 2003-2013 period (9.39%). The intermediate periods show in general a more varied picture, with change occurring homogeneously in all the categories. The whole area study includes also the North-East side of the image, where a high rural activity developed in the period taken into account, therefore a closer view on the Oasis area, centered on the RSCN Reserve, for shorter temporal scales is also analyzed (Fig. 5.5).

The centered CVA image for 1984-2013 (Fig. 5.5-j) detects a high change towards Bare soil expansion in the Reserve area and this is affirmed by the base maps. The CVA image for 1984-1990 (Fig. 5.5-f) detects Bare soil expansion and Moisture reduction all along the Reserve area and the mudflat. This trend continues in the 1990-1998 CVA image (Fig. 5.5-g), where the drying up of the major pools adjacent to the mudflat is evident. This trend is partly halted in the following CVA image for 1998-2003 (Fig. 5.5-h) likely as a result of the restoration project completed in 1998 through the GEF fund, and in fact a replenishment of green areas is detected in the central part of the marsh. The following CVA image for 2003-2013 (Fig. 5.5-i) shows again a change towards Bare soil expansion and this is attributable to the fire that broke out in October 2010, after which the Reserve was temporarily closed and could open again just in April 2011: the fire's consequences on the vegetation were still evident during the field visit in June 2014.

A closer analysis of the CVA results on the area of the pools surrounding the former Shishan springs was also considered (not shown here). The results show a main change towards drier conditions between 1990 and 1998, as expected, and a partial recovery between 1998 and 2003. Finally between 2003 and 2013 the Oasis achieves its present conditions, with the former springs' pools left empty and a partial recovery of the marsh and of the stream that flows towards the former Burgees pool (Fig. 5.3).
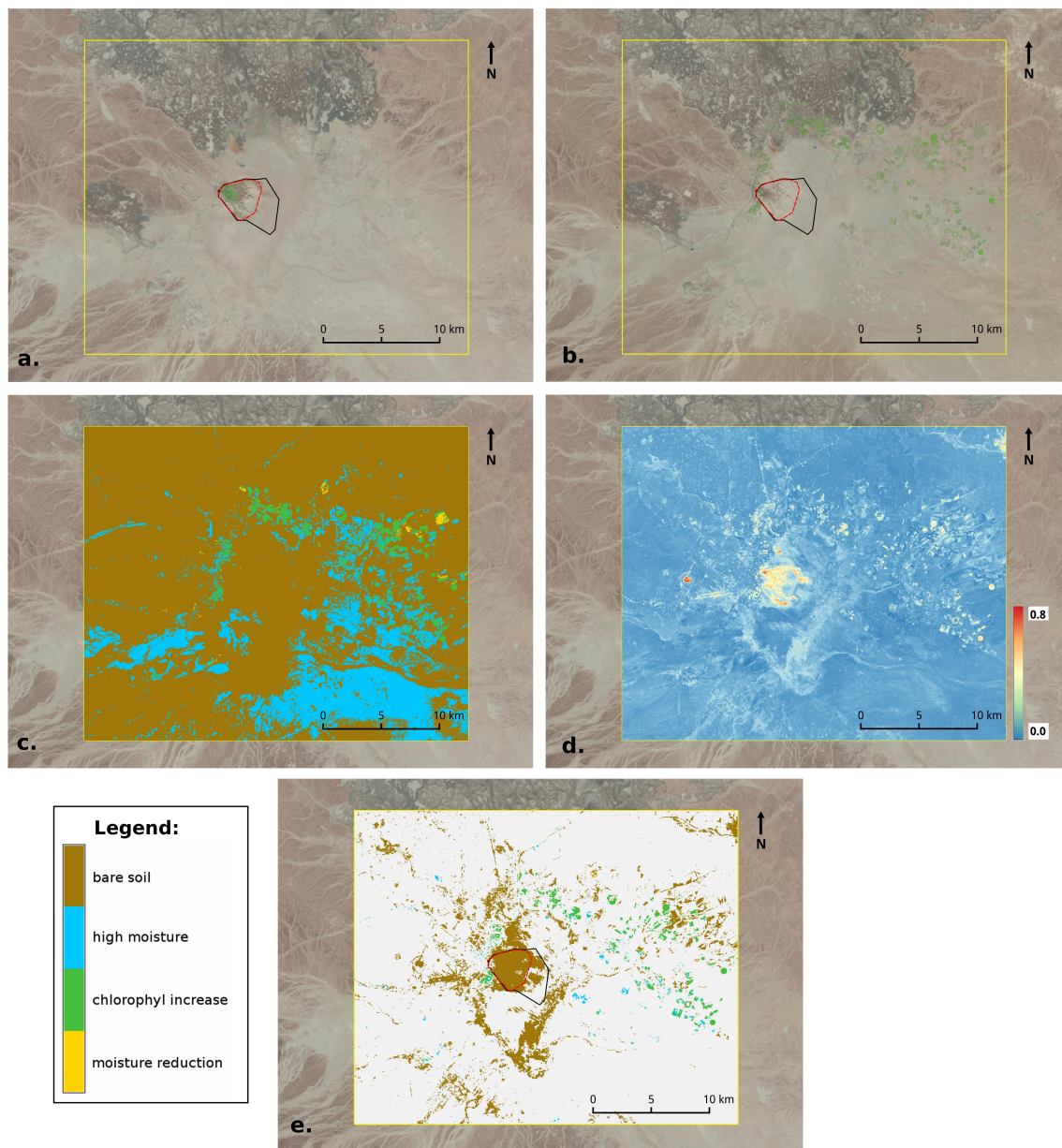
Figure 5.4: Landsat look-like image for August 30, 1984 (a) and August 30, 2013 (b) and results of the CVA between the two images for the study area: directions (c) and magnitude (d) images before applying the threshold, final change detection analysis (e); RSCN Reserve border (in red) and the 1979 RAMSAR fence (in black) are shown.
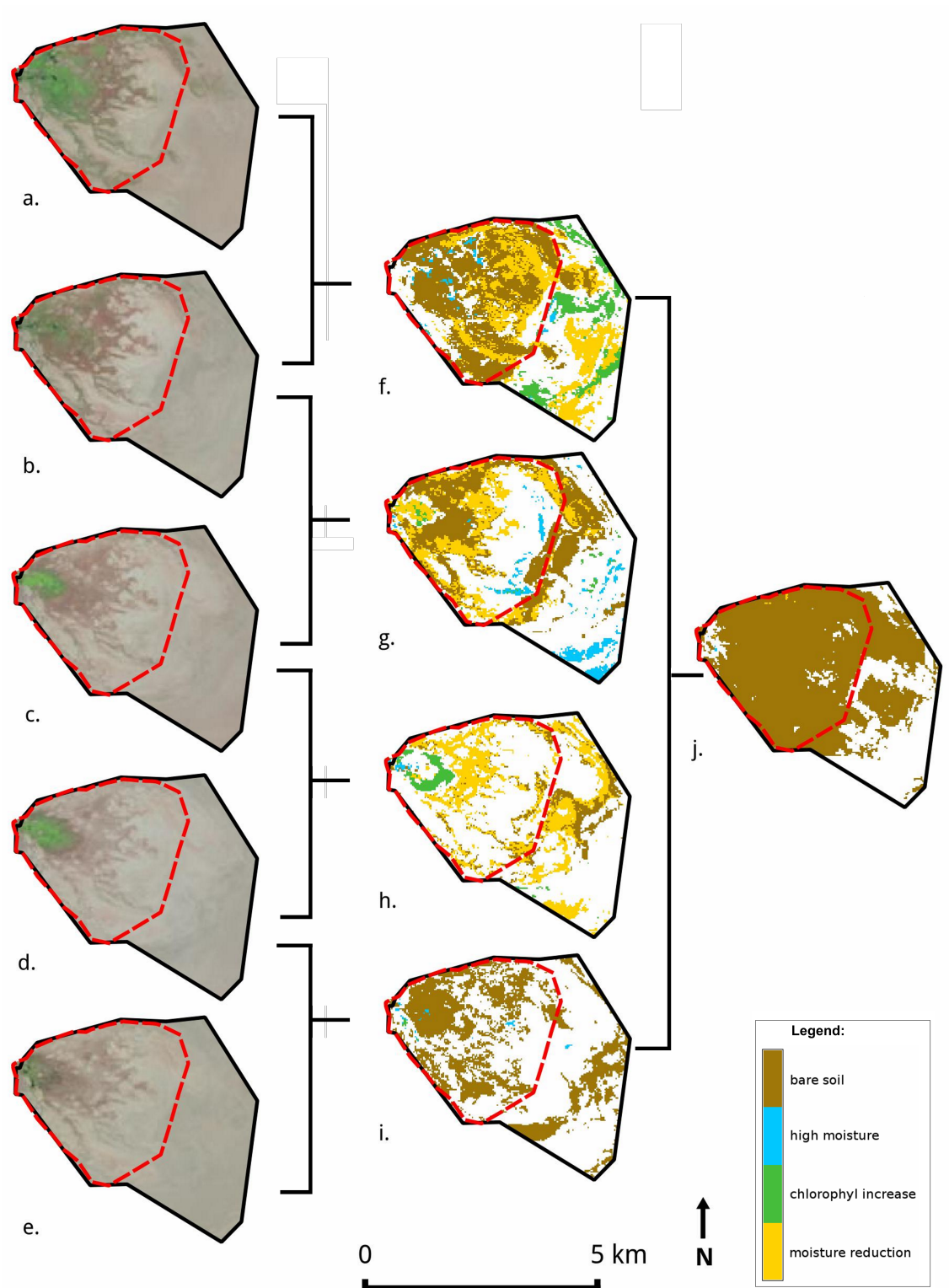
Figure 5.5: Look-like Landsat images (a 1984, b 1990, c 1998, d 2003, e 2013) and CVA results images (f 1984–1990, g 1990–1998, h 1998–2003, i 2003–2013, j 1984–2013) for the Reserve area from 1984 to 2013 (for the dates specification see Tab. 3.5).

5.2   Analysis of the LULCC along the Syrian-Turkish border in the last 30 years

The study area covers 64,800 squared kilometers in a region comprised between 38E/35N and 37E/42N long/lat, see Fig. 5.6. The area includes several irrigated and cultivated lands around the Syrian-Turkish border, specifically, referring to the Corine land cover map for 2006, it comprises the Sanliurfa-Harran irrigated plains in Turkey on the West, following the Balikh River to the South until his junction with the Euphrates Rivers, therefore including the rural area, so-called 'horseshoe', around the town of Raqqa (canalized water from the Baath Dam). Moving to the East we have the steppe covering most of the area until the Khabur River bed, where it is easily recognizable the funneled shape of the two tributaries coming from Ras Al Ain spring (West) to the Jaghjagh river (East) originating from the karstic springs near Qamishli. Above this area, beyond the border, lye the Celainpinar plans, also irrigated through the tunnels coming from the Ataturk Dam, like the Urfa plans. On the East the study area comprises the fertile Al Hasakah triangle closed in the Syrian border with Turkey and Iraq, and therefore part of the Tigris river until the Saddam Lake, originated by the Saddam Dam.
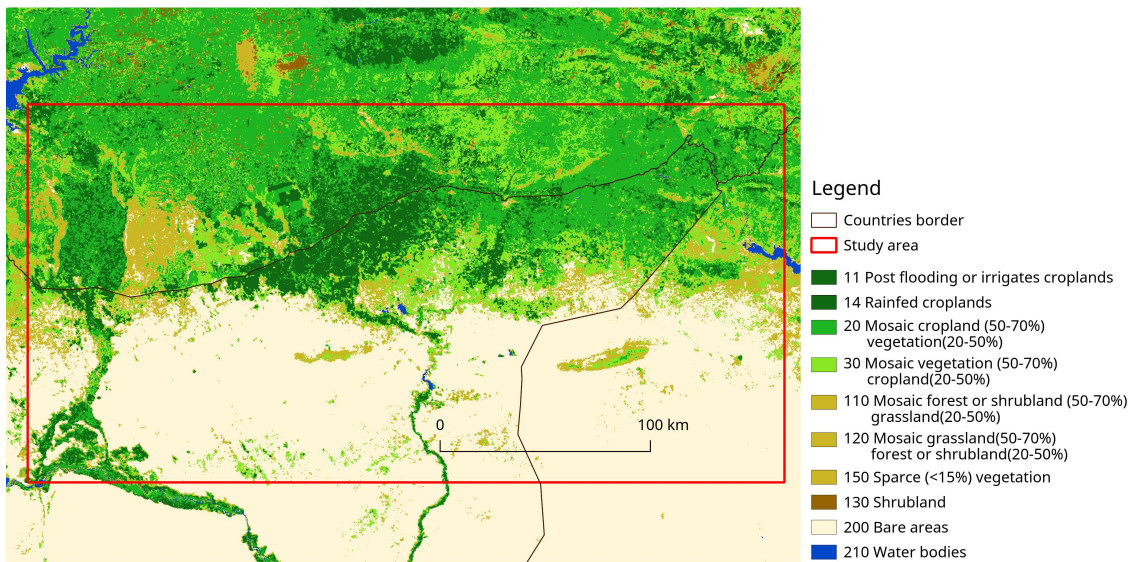
Figure 5.6: Jezira study area (in red) and 2009 land cover map, from ESA GLOBCOVER Project.

The RS technique used for the analysis is the new combined methodology explained in Chap.4. The raw images (see Tab. 3.6 for the dates) were firstly corrected atmospherically to TOAR, then transformed to TCT features in Grass GIS software. The subsequent mo-

saicking of the images showed some minor errors in the areas at the border between images from different paths, especially for the earliest available images, from Landsat 5 (1984).

A correction through histogram matching was performed, but was rejected for unsatisfactory results, probably caused by the differences in land cover throughout the study area, from vegetated humid high-plains in the North to deserted bare areas in the South part. This choice doesn't seem to have affected considerably the results, since no border is detected in the final change maps.

Secondarily the CVA was performed in Grass GIS, while MAD andMAF transforms were carried out in Qgis through Orfeo Toolbox. The two techniques were combined in Grass GIS overlapping the results, in order to get the categories of CVA on the spatial results of the MAD-MAF, obtaining in the end a map with four categories of direction of the change between two dates.

A qualitative analysis of the actual change on the single fields, which may be due to change in crop type or seasonal variation in the specific plantation, goes behind the aim of this study and is not feasible lacking data on the ground for the whole time frame. In the same time, several fields pattern are clearly distinguishable even if temporarily not covered by vegetation, and it's not possible to establish if this is due to abandonment or temporary pause in the cultivation (fields rotation or seasonal pattern of the single cultivation). The idea thus is to check if in the region as a whole there has been an overall variation in the pattern of the vegetated/not vegetated areas, and this is possible with this study through a quantification of the change towards more wet and green or, on the opposite, towards more arid and dry conditions. In fact some new fields, whose pattern is easily recognizable by the classical canalization figure, are detected by CVA as change towards more humid conditions, where photo-interpretation allows to distinguish the presence of new irrigated areas, but not temporarily cultivated. This is explained as a change in the soil moisture, which is recognized by the technique comparing it to the drier preceding conditions of non-cultivated soil.

The results of the combined RS methodology are shown in Tab. 5.2, where the overall areal change between the 1984 and 2015 maps is shown for the whole study area. Tab. 5.3 and Tab. 5.4 show the change on selected intervals, at half time of the whole span period (1984-1999 and 1999-2015) and at half of this second period (1999-2006 and 2006-2015). A mid-term date was chosen, in 1999, following a year of relative high winter rainfall in 1998 and preceding the early 2000s drought. To investigate the 2006-2010 drought effects then a mid-term date for the second half of the period was also taken into account, for summer 2006.

The map of the change is shown in Fig. 5.7 C for the period 1984-2015, while the false color RGB images for the two dates are also shown in Fig. 5.7 A and B.

CVA classes %	Total area		Syria		No Syria	
	km²	%	km²	%	km²	
Moisture reduction	92	0.14	7	0.01	85	0.13
Chlorophyll increase	2201	3.40	255	0.39	1946	3.00
Moisture increase	138	0.06	37	0.00	101	0.06
Bare soil expansion	733	1.13	602	0.93	131	0.20
Area changed	3164	4.73	1.39	901	3.34	2263

Table 5.2: Change in the study area by category between 1984 and 2015 with distinction for Syrian and no-Syrian (Iraq and Turkey) territories , in % of the study area and total square kilometers.

CVA classes	1984-1999				1999-2015			
	Syria		No Syria		Syria		No Syria	
	%	km²	%	km²	%	km²	%	km²
Moisture reduction	0.52	339	0.65	419	0.11	35	0.37	242
Chlorophyll increase	1.31	846	1.23	794	0.32	205	2.39	1548
Moisture increase	0.31	200	0.55	358	0.13	85	0.51	328
Bare soil expansion	0.78	507	0.26	171	2.08	1348	0.43	282

Table 5.3: Change in the study area by category, with distinction for Syrian and no-Syrian (Iraq and Turkey) territories in the whole period (1984-2015) divided in two, in % of the study area and total square kilometers.

CVA classes	1999-2006				2006-2015			
	Syria		No Syria		Syria		No Syria	
	%	km²	%	km²	%	km²	%	km²
Moisture reduction	0.69	450	1.28	829	0.40	257	1.14	741
Chlorophyll increase	0.62	403	0.61	396	0.13	86	1.31	852
Moisture increase	0.78	503	1.17	761	0.48	314	1.43	928
Bare soil expansion	0.77	502	0.42	269	0.86	557	0.31	200

Table 5.4: Change in the study area by category, with distinction for Syrian and no-Syrian (Iraq and Turkey) territories in the second half period (1999-2015), in % of the study area and total square kilometers.

CVA legend: ■ 1ˢᵗquadrant ■ 2ⁿᵈquadrant ■ 3ʳᵈquadrant ■ 4ᵗʰquadrant
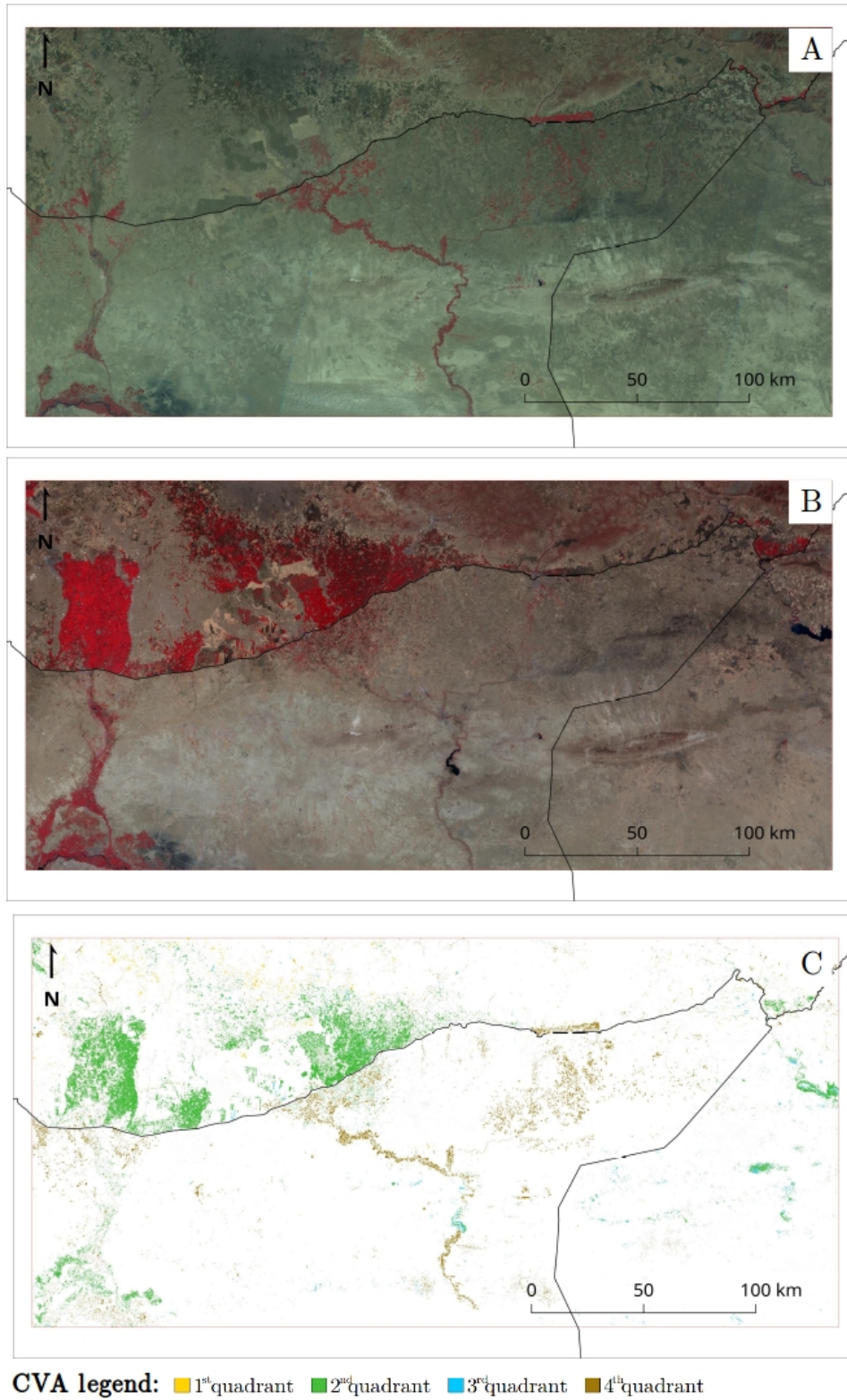
Figure 5.7: A. False colors RGB map of the study area for 1984; B. false color RGB map of the study area for 2015; C. change map between the two dates. For the legend of the change map refer to Fig. 2.5.

Change between 1984-2015 is evident towards greener conditions, with more than 2000 km^2 of changed area (the highest category, 3.40% of the study area). A further distinction between the change occurred within Syrian borders and the rest of the map, comprising territories in Turkey and Iraq, shows though that most of this change (3.00%) happened outside of the Syrian territory, where the most vast change was toward Bare soil expansion (0.93%).

The half time analysis (1984-1999-2015) shows a different picture. In fact, in the first half of the considered period (1984-1999), both in Syria and outside, the major change has been towards more vegetated conditions with comparable values (around 1.30%), while the rest of the categories shows lower and comparable rates. In the second half of the period though (1999-2015), the change in Syria is evidently towards drier conditions (more than 2%) while the rest of the study area experiences an analogue rate of change towards more vegetated conditions.

An additional analysis of the change occurred before and after the 2006-2010 drought, separating the second 15 years period in two, exhibits a more varied picture. In Syria the change towards drier conditions, comprising Moisture reduction and Bare soil expansion, in 1999-2006 is comparable to the one occurred in the 2006-2015 period (1.46% and 1.26%, summing up the two contributes), and is comparable to the change towards more wet and green conditions, that instead diminished in the second half of the period (0.61% compared to 1.40%). In the same period, 1999-2006, the Turkish-Iraqi side exhibits an analogue behavior, with comparable changes towards drier and wetter conditions, but experiences in the 2006-2015 period an increase of green and humid conditions (from 1.78% to 2.74%), almost double compared to the areas who changed towards Bare soil expansion and Moisture reduction (1.44%).

Analyzing the 2006-2015 period, the difference of the type of change happened in the two sides can't be attributed only to climatic variations, given the contingency determined by the boundary conditions. The Syrian civil conflict, who started in the middle of this time, can't be considered the only cause either. The results, put together with an analysis of the political situation and development in the last 30 years, lead to hypothesize that the difference must be due to several contributing factors, ranging from the mismanagement of the resources, lack of effective political response to the drought/climatic conditions, rural abandonment caused by the conflict in terms of territorial limitations and fleeing. What is remarked from this research is the striking difference between the change occurred in this region across the border, that is now not only visible by photo-interpretation of satellite images, but also quantified.

Analyzing the overall spatial change, from visual interpretation, it's evident from the change map the revitalization of the Balikh River, in the West of the study area, whose flow completely stopped in 1985 due to the drying out of Ain Al Arous spring. In fact the flow started again thanks to the water coming from the Sanliurfa plans, as a result of the outflow and residuals of water used for irrigation, following the Urfa tunnels construction [UN-ESCWA and BGR, 2013]. This contributed to the development of the cultivated land surrounding Al Raqqa, where though also canalization from the Al Baath dam brought croplands expansion.

To illustrate more clearly the change occurred in the study area, some smaller areas are taken into account as indicative of the whole picture, and shown in detail in Fig. 5.8 and 5.9. The area around Ras Al Ain spring also experienced a recovery in the 1999-2006 period, as shown in Fig. 6, where the visual comparison among the border with Turkey show analogues changes on both sides of the line. The whole area, predominated by the presence of the Khabour River, in fact went dry for the underground water exploitation and therefore the disappearance of the karstic springs in 2001 [De Châtel, 2014b; UN-ESCWA and BGR, 2013]. The subsequent change map, for the period 2006-2015, shows the change that is then indicative of the second half of the thirty years period, namely a strong introduction of irrigated areas in Turkey, while Syria experiences the loss of fields present up to 1984.

Southern of this area, around Al Hasakah town, it's interesting to notice the replenishment of croplands and irrigated lands thanks to the Hasakah dams, built around 1990 [UN-ESCWA and BGR, 2013], that are in fact visible in the 1984-1999 change image, and disappear again in the 1999-2006 change map (see Fig. 5.9). It's evident the abandonment of the floodplain agriculture along the river, in favor of the creation of new irrigated areas along canals, especially in the 1984-1999 change map. This trend continues in the 1999-2006 period, as seen in the whole picture, with an enlargement of the Hasakah South Lake, while in the last period (2006-2015) the two Northern lakes completely dry out and the South lake shrinks to the 1999 conditions. In general, the overall change along the thirty years doesn't notice the existence of the two Northern Hasakah lakes (formed by the North and East Hasakah dams, see Fig. 1.4).
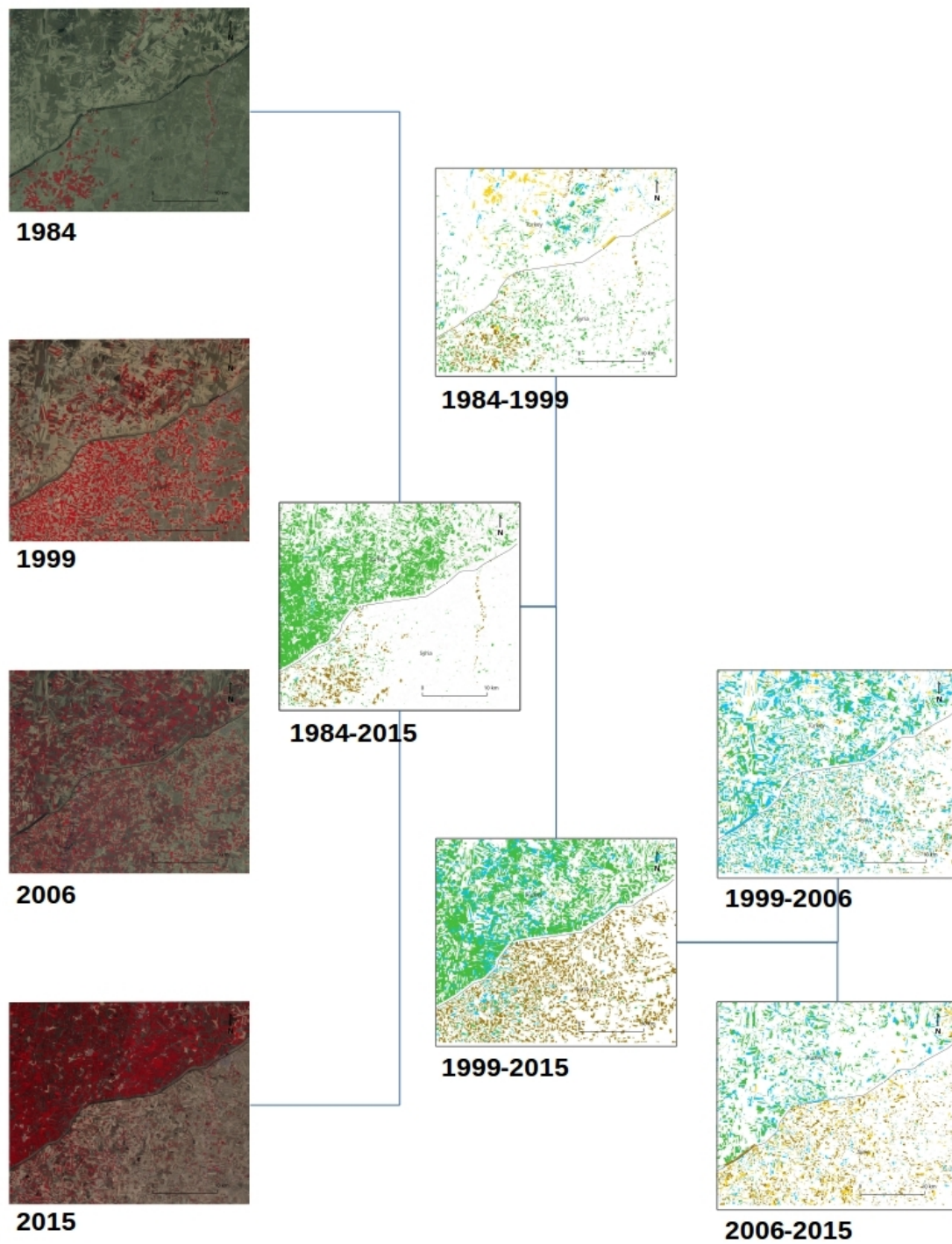
Figure 5.8: RGB false color image and change map between selected temporal intervals for the area around Al Hasakah, Syria. For the legend of the change map refer to Fig. 2.5.
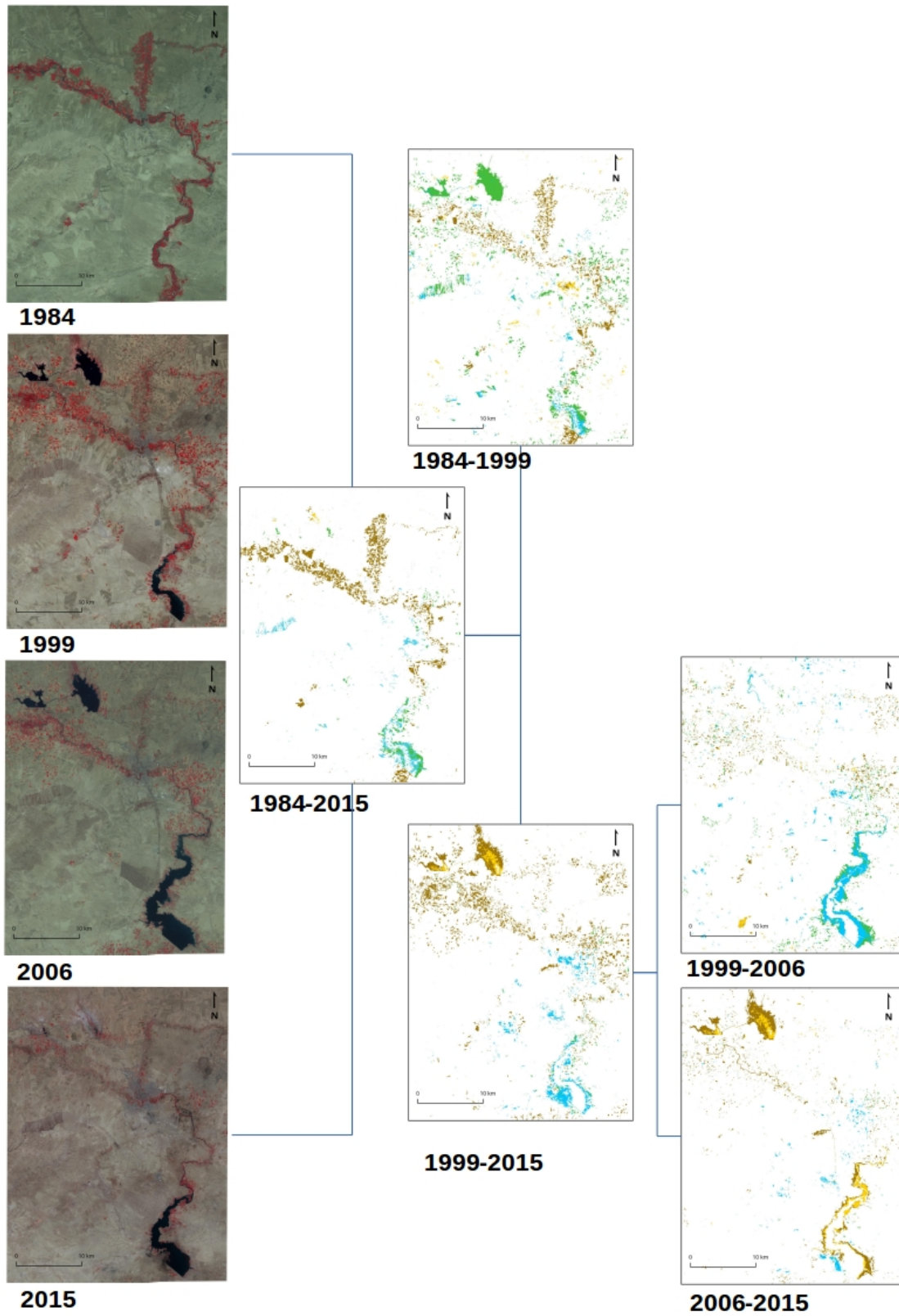
Figure 5.9: RGB false color image and change map between selected temporal intervals for the area around Al Hasakah, Syria. For the legend of the change map refer to Fig. 2.5.

Conclusions

Aim of this research was to investigate Remote Sensing (RS) change detection techniques in desertication studies. Given the very nature of this phenomena, who interests wide areas of the Earth surface, the usage of RS can be really powerful and effective in detecting, monitoring and prevent desertification processes.

With this purpose, two case studies were selected in the Middle East region as indicative for desertification analysis: Al Azraq Oasis, in Jordan, and the Jezira region, across the border between Syria and Turkey. The first one constitutes an example of wetlands drying out in arid areas, whose change on the surface in a time interval through the 1990s was rapid and particularly evident. The relevance of the second case study is given by the land use and water management difference between the bordering countries, making of this area a good example for the study of the impacts of droughts and political decisions on land cover development in a semi-arid region.

After a preliminary assessment of the available RS techniques for change detection studies in arid and semi-aris areas, the research focused on two main techniques: Change Vector Analysis (CVA) [Malila and Lafayette, 1980], applied to the outputs of the Tasselled Cap Transform (TCT) [Kauth and Thomas, 1976], and the Maximum Autocorrelation Factor (MAF) transformation of the Multivariate Alteration Detector (MAD) components (MAD/MAF) [Nielsen et al., 1998]. Both CVA and MAD/MAF are considered unsupervised techniques, meaning that they perform the change detection without preliminary information on the ground. The advantage of this two techniques is that they can be applied in a semi-automated manner and they give a time and cost-effective procedure for LULCC studies. Their downside though is the lack of a precise interpretation of the results. A second aim of the research thus is to investigate the possibility of an improvement in the intepretation of both techniques, by their use in a combined procedure.

The use of TCT in arid and semi-arid areas (together *drylands*) was investigated, developing several new sets of TCT coefficients for SPOT 4, Landsat 5 and Landsat 8 satellites. Several images of selected drylands locations in the Middle East were employed for the

calculation, in order to overcome the dependency of the TCT on season and location, and to detect desert specific conditions.

As a first step of the research, an analysis was performed of the capability of the new desert-adapted TCT applied to CVA to detect surface changes in arid areas, using as a case study the wetland of the Azraq Oasis, Jordan. The analysis was carried out on a 30 years interval (1984 to 2013) on Landsat satellite images.

CVA gives as an output a map of the magnitude and a map of the direction of the change between two dates, having the advantage of not needing a previous land use/land cover classification. However two main issues, intrinsic to the use of the CVA, can be stressed: the first is deciding what the meaningful change is, namely choosing a threshold for the change detection, and the second is the absence of an objective validation method. The first issue was addressed using a statistical criteria for the selection of the threshold (average of the magnitude values plus the standard deviation), resulting in an automatic selection of the value for each couple of dates. The second one was faced with the support of data and material collected in a field visit in June 2014, together with several sources available in literature.

The results show that the CVA applied to the new desert-adapted TC transform features is able to detect the expected changes in the studied area, and can therefore be considered a valuable technique for change detection studies in areas subject to desertification and deterioration processes in drylands.

An added value of the research is the integration of a CVA calculation module into the Free and Open Source Software (FOSS) project Grass GIS, making the implementation of the technique available and editable by future users.

The combination of CVA and MAD/MAF techniques was then addressed, taking as validation areas two sites in the Middle East region. The first, Al Azraq Oasis, was chosen as a representative of drying conditions, while the second one, South Hasakah Lake, in Syria, was considered for water bodies replenishment.

A first attempt to combine two change detection techniques was carried out using CVA combined with the output of MAD analysis. The results, applied to Landsat images between 1984 and 2015, were positive but not satisfying, due to the nature of the MAD components, where the noise is spread among the bands, and to the difficulty in overlapping the many categories given from the two techniques together. A second approach took into account the MAD/MAF components, that groups the images differences, called variates, by decreasing autocorrelation. In this case, one single variate was chosen and combined with the CVA output.

The results of the application to Al Azraq Oasis, show that the two techniques can be successfully used in a combined way because they give complementary information: while CVA gives a meaning of the surface change, MAD gives a slightly more detailed map of the change on the surface. In this sense, the first MAF variate, appropriately thresholded, can be used like a first step for the identification of the changed features, while a second step is taken assigning a meaning to the features by the CVA semantic classification. This procedure is corroborated by the high correspondence between the change found by the individual techniques: once thresholded and reclassified, MAF positive values match with the CVA classes indicative of changes towards drier conditions, while MAF negative values correspond to the classes of CVA indicative of changes towards more wet and vegetated conditions.

Extending the results to the second case study, the expected visual superficial change is again detected by the combined methodology, namely the replenishment of water in the Lake and the loss of cultivated areas along the river. Missing ground truth data, though, an accurate validation of the results can't really be performed in this case. Only the correspondence with the results obtained for Al Azraq Oasis can give some positive feedback about the methodology, beside the fact that the visual change on the surface is correctly identified.

An important output of the research is the improvement in the use of MAD/MAF technique in change detection studies. Previously, the interpretation of the MAD/MAF was not straight-forward and in general relied on the single researcher's choices. The research has showed how using a statistical criteria for the threshold determination, and relying on the correspondence between the results of CVA and MAF's first component, the combined technology provides an almost automated, time effective and reproducible technique. As such, it can be used as either a complementary procedure or a first interpretation step in change detection studies. The fast detection can be used for example to perform a preliminary selection of relevant time intervals, on which to perform more accurate change studies with the support of ground data. The methodology then has been found effective for desertification studies in arid and semi-arid areas, detecting the expected change on the surface.

A limitation of the methodology is given by the choice of the threshold applied to both techniques, that relies on the researcher. Another weak point is that the method has been employed just in a restricted number of cases and could be tested in other geographical regions. Future works can be considered in order to validate the technique, both by verification of the results against ground truth data and by comparing them with other change

detection techniques. The implementation of higher order MAF variates could also be taken into account, for a complete investigation of the technique.

Finally, an application of the new combined methodology was carried out in the second case study. An analysis has been conducted of the spatial change occurred on the surface along the Syrian-Turkish border between 1984 and 2015 in summer conditions, taking into account an area of 86,400 km^2 on the North-Eastern side of the Syrian country.

Despite being geographically adjacent, the two sides of the border exhibit a different evolution in the land cover along the thirty years interval. Specifically they exhibit a similar pattern along the first half of the period, between 1984 and 1999, while the difference becomes striking in the second half of the period, between 1999 and 2015. The analysis was conducted between years preceeding some multi-year droughts, occurred at the beginning of the 21st century and then between 2006 and 2010. It was expected therefore that the surface would exhibit similar conditions of regeneration, or at least non-drying conditions, in the whole study area.

The non-Syrian side shows in fact in general a change towards more vegetated and more humid conditions in all the considered time intervals, while the Syrian side experienced this pattern only in the first fifteen years. A further analysis of the second half of the whole period shows that the actual change was heavily conditioned by the drought started in 2006. In fact from 1999 to 2006 the non-Syrian and the Syrian territories exhibit analogue changes on the surface, with similar rates among drier and wetter conditions. Instead from 2006 the Syrian side shows a change towards drier conditions that is more than double (1.26% of the whole study area) than the one towards greener and more humid conditions (0.61%). In the same the non-Syrian side experienced an overall regeneration (2.74% of the study area), almost double compared to the areas who went through a bare soil expansion and moisture reduction change (1.44%).

This different behavior in adjacent territories can't be attributed to different climatic conditions. On the opposite, the research proves that other factors, like different political responses to the 2006-2010 drought crisis, have to be addressed as the cause.

As a parallel result, the research shows the impact of large water system management structures on the land cover in Turkey, with an evident expansion of irrigated areas between the Sanliurfa and Celainpynar plans. In the same time Syria, still under the strain of a long lasting civil conflict, experiences the consequences of a long time political crisis and of an improper use of the water resources, which caused the deterioration of a territory that was once known as the country's 'bread-basket' and ensured the national autonomy in terms of wheat production.

In conclusion, the research proved the powerness of RS tools in change detection analysis for desertifcation studies. Existing tools were improved and new tools were implemented, with the added value of making them available to other users, through GFOSS software and publications.

Appendices

A i.cva Grass GIS source code

Available at: https://trac.osgeo.org/grass/browser/grass-addons/grass7/imagery/i.cva/i.cva.py

```
#!/usr/bin/env python

#%module
#% description: Performs Change Vector Analysis (CVA) in two dimensions
#% keyword: imagery
#%end
#%option G_OPT_R_INPUT
#% key: xaraster
#% description: Name of the first raster for X axis
#%end
#%option G_OPT_R_INPUT
#% key: xbraster
#% description: Name of the the second raster for X axis
#%end
#%option G_OPT_R_INPUT
#% key: yaraster
#% description: Name of the first raster for Y axis
#%end
#%option G_OPT_R_INPUT
#% key: ybraster
#% description: Name of the second raster for Y axis
#%end
#%option G_OPT_R_BASENAME_OUTPUT
#% label: Name for output basename raster maps (angle and magnitude)
#%end
#%option
#% key: custom_threshold
#% description: Use a custom threshold
#% guisection: Magnitude threshold
#% type: double
#% required: no
#% descriptions: Insert numerical value for the threshold to perform the analysis
#% multiple: no
```

```
#%end
#%option
#% key: stat_threshold
#% description: Use a statystical parameter for the threshold (mean + N * standard
    deviation)
#% guisection: Magnitude threshold
#% type: double
#% required: no
#% descriptions: Insert the integer value for a multiple of standard deviation (to
    be summed to the mean of the magnitude values )
#% multiple: no
#%end
#%rules
#% exclusive: custom_threshold, stat_threshold
#%end


from __future__ import print_function
import atexit, sys
import grass.script as grass
from grass import script


TMPRAST = []

def delta_calculation(delta, second_band, first_band):
    """
    Calculates the Delta as difference between the second band and the first band
    """
    equation = ('$delta = $second_band - $first_band')
    grass.mapcalc(equation, delta=delta, second_band=second_band, first_band=first_
        band)

def angle_calculation(anglemap, deltaX, deltaY):
    """
    Calculates the vector angle as the arctg of deltaY/deltaX
    """
    equation = ('$anglemap = atan($deltaX,$deltaY)')
    grass.mapcalc(equation, anglemap=anglemap, deltaX=deltaX, deltaY=deltaY)

def magnitude_calculation(magnitudemap, deltaX, deltaY):
    """
    Calculates the vector length (magnitude) as sqrt((deltaX)^2+(deltaY)^2)
    """
    equation = ('$magnitudemap = sqrt((($deltaX)^2)+(($deltaY)^2))')
    grass.mapcalc(equation, magnitudemap=magnitudemap, deltaX=deltaX, deltaY=delta
        Y)

def change_map_calculation(change_map, magnitude_map, threshold, angle_map_class):
    """
```

```
    Generates the change map as the values of the classified angle map whose magnit
        ude follows the criterion (values higher than the threshold)
    """
    equation = ('$change_map = if($magnitude_map>$threshold,$angle_map_class,null()
        )')
    grass.mapcalc(equation, change_map=change_map, magnitude_map=magnitude_map, thr
        eshold=threshold, angle_map_class=angle_map_class)

def main():
    options, flags = grass.parser()
    xAmap = options['xaraster']
    xBmap = options['xbraster']
    yAmap = options['yaraster']
    yBmap = options['ybraster']
    output_basename = options['output']
    custom_threshold = options['custom_threshold']
    stat_threshold = options['stat_threshold']
    Xdelta_name = 'deltaX'
    Ydelta_name = 'deltaY'
    anglemap_name = output_basename + '_angle'
    anglemap_class = anglemap_name + '_class'
    magnitudemap_name = output_basename + '_magnitude'
    changemap_name = output_basename + '_change'

    # Checking that the input maps exist
    if not grass.find_file(name=xAmap, element='cell')['file']:
        grass.fatal("xaraster map <%s> not found" % xAmap)
    if not grass.find_file(name=xBmap, element='cell')['file']:
        grass.fatal("xbraster map <%s> not found" % xBmap)
    if not grass.find_file(name=yAmap, element='cell')['file']:
        grass.fatal("yaraster map <%s> not found" % yAmap)
    if not grass.find_file(name=xBmap, element='cell')['file']:
        grass.fatal("ybraster map <%s> not found" % yBmap)

    TMPRAST.append(Xdelta_name)
    TMPRAST.append(Ydelta_name)

    # Calculating delta for X and Y bands
    grass.message(_("Calculating DeltaX and DeltaY"))
    delta_calculation(Xdelta_name, xBmap, xAmap)
    delta_calculation(Ydelta_name, yBmap, yAmap)

    #Calculating angle and magnitude maps
    grass.message(_("Writing angle map %s") % anglemap_name)
    angle_calculation(anglemap_name, Xdelta_name, Ydelta_name)

    grass.message(_("Writing magnitude map %s") % magnitudemap_name)
    magnitude_calculation(magnitudemap_name, Xdelta_name, Ydelta_name)

    # Reclassifing angle map to get a map with the four quadrants
```

```
keys = ['1', '2', '3', '4']
vals = [0, 90, 180, 270, 360]
rvals = [(int(vals[i-1]), int(vals[i]), keys[i-1], vals[i-1], vals[i]) for i in
    range(1, len(vals))]
rules = '\n'.join(['%3d thru %3d = %s    %s-%s' % v for v in rvals])
script.write_command('r.reclass', input=anglemap_name, output=anglemap_class, r
    ules='-', overwrite=True, stdin=rules.encode())

# Generating the change detection map using the given threshold
if custom_threshold:
    threshold = custom_threshold
    grass.message(_("Threshold is %s") % threshold)
    grass.message(_("Writing change detection map %s") % changemap_name)
    # Creating the final map of the change, using a custom threshold
    change_map_calculation(changemap_name, magnitudemap_name, threshold, anglem
        ap_class)
elif stat_threshold:
    #Getting values of mean and standard dev of magnitude to calculate the chan
        ge detection criteria (> mean + N*stdev)
    univar = grass.read_command('r.univar', map=magnitudemap_name, flags='g')

    found = 0
    for line in univar.splitlines():
        name,val = line.split('=')
        if name == 'mean':
            grass.message(_("Mean of magnitude values is: %s") % val)
            mean = val
            found += 1
        if name == 'stddev':
            grass.message(_("Standard deviation of magnitude values is: %s") %
                val)
            stddev = val
            found += 1
    if found != 2:
        grass.fatal("Couldn\'t find mean or stddev!")

    adding_value = float(stat_threshold) * float(stddev)
    threshold = float(mean) + float(adding_value)
    grass.message(_("Threshold is %s") % threshold)
    #Creating the final map of the change, using a statistical threshold
    change_map_calculation(changemap_name, magnitudemap_name, threshold, anglem
        ap_class)
else:
    grass.message(_("No threshold given, only angle and magnitude maps have bee
        n created"))


    return 0

def cleanup():
```

```
    # !Delete temporary maps
    TMPRAST.reverse()
    for i in TMPRAST:
        script.run_command("g.remove", flags='f', type='raster', name=i, quiet=Tru
            e)


if __name__ == "__main__":
    atexit.register(cleanup)
    sys.exit(main())
```

B R code for TCT calculation

Example of the R code used for the calculation of TCT in R for Landsat 8 satellite for the
Jordan site (Al Azraq Oasis).

```
library("rgrass7")
library("rgdal")
library("raster")


#defining functions
multi_select_func <- function(pattern_list, original_list) {
  new_list=c()
  for (i in pattern_list) {
    new_list=c(new_list, grep(i, original_list, value=TRUE, fixed=FALSE))
  }
  return(new_list)
}


# ------ CHOOSING GRASS MAPSET AND LOCATION
initGRASS(gisBase = "/usr/lib/grass70", home = tempdir(),
          gisDbase = "/home/username/grassdata/",
          location = "utm37N-landsat", mapset = "TC_calc", #!!! change depending on
              the folder you want!!
          override = TRUE)


# ------ GETTING FROM GRASS THE LIST OF RASTERS AVAILABLE IN THE CHOOSEN MAPSET
grass_filename_list <- execGRASS("g.list", parameters=list(pattern="*",type="rast")
    , intern=TRUE)
grass_filename_list


# ------ CONSTS (CHANGE DEPENDING OF WHAT YOU NEED)
#the following division into categories is a duplicate of the one existing in the q
    gis attribute table,
#and must be maintained manually up-to-date.
MASK_NAMES_TERRAIN = c(paste0("S",LETTERS[1:20])) # SA, SB, ...
MASK_NAMES_VEGET = c(paste0("V",LETTERS[1:20])) # VA, VB, ...
MASK_NAMES_WATER = c(paste0("W",LETTERS[1:20])) # WA, WB, ...
```

```
MASK_NAMES_TOT=c(MASK_NAMES_TERRAIN, MASK_NAMES_VEGET, MASK_NAMES_WATER) # this def
    inition must be changed in case the masks' name changes in Qgis
MASK_NAMES_TOT

DATES=c("201403") #c("201312")
NUM_OF_BANDS=7

#STEP1: Load all images into a dataframe
list_filename_patterns_tot=c()
for (date in DATES){
  for (maskname in MASK_NAMES_TOT){
    list_filename_patterns_tot=c(list_filename_patterns_tot,paste0(date,"_",masknam
        e,"_B*"))
  }
}
list_filename_patterns_tot

list_rasternames_tot=grep(paste(list_filename_patterns_tot,collapse="|"), grass_fil
    ename_list, value=TRUE)
list_rasternames_tot
#importing maps from Grass depending on the above-chosen criteria for raster names
rasters_list_tot=c()
for (i in list_rasternames_tot){
  execGRASS("g.region", raster=i)
  system("g.region -p")
  print(i)
  raster=readRAST(i) #this is the single image for each band and mask
  image(raster, col=rainbow(200))
  raster_df=data.frame(raster)
  #print(raster)
  raster_col=c(subset(raster_df, select = -c(s1,s2) )) #taking off the columns with
       coordinates (called s1 and s2)
  #creating a list with all the rasters:
  rasters_list_tot=c(rasters_list_tot,raster_col) #NB: transforming to dataframe ta
      kes some time, so it's better to do it right after...
}
#rasters_list_tot
raster_df_tot=data.frame(rasters_list_tot) #creating dataframe from the list
names(raster_df_tot)=list_rasternames_tot #need this step to give to the columns th
    e correct names (otherwise R adds an X at the beginning, since the names in Gra
    ss start with a number and looks like R doesnt like it). If not, the multi_sele
    ct funciton doesn't work later on
head(raster_df_tot)
length(raster_df_tot)
max(raster_df_tot) #to verify dataframe values
min(raster_df_tot)
summary(raster_df_tot)

#STEP 2: create dataframes by category
```

```
#application of multi_select_func with for ex. pattern_list=MASK_NAMES_TERRAIN , or
    iginal_list=list_rasternames_tot
raster_df_terrain=raster_df_tot[,multi_select_func(MASK_NAMES_TERRAIN, list_rastern
    ames_tot)]
head(raster_df_terrain)
#summary(raster_df_terrain)
#is.na(raster_df_terrain)

raster_df_veget=raster_df_tot[,multi_select_func(MASK_NAMES_VEGET, list_rasternames
    _tot)]
head(raster_df_veget)
#summary(raster_df_veget)
#is.na(raster_df_veget)

raster_df_water=raster_df_tot[,multi_select_func(MASK_NAMES_WATER, list_rasternames
    _tot)]
head(raster_df_water)
#min(raster_df_water)
#summary(raster_df_water)
#is.na(raster_df_water)

#STEP 3: create dataframes by band
LANDSAT_BANDS=NUM_OF_BANDS #NUM_OF_BANDS+1
landsat_numbers=c()
band_name_list=c()

for (i in 1:LANDSAT_BANDS){
  band_name=paste0("Band",i)
  landsat_numbers=c(landsat_numbers, i)
  band_name_list=c(band_name_list, band_name) # crea una lista Band1, Band2, ... Ba
    ndN
}

create_df_byband <- function(df_by_category) {
  raster_byband=data.frame()
  column_band_list=c()
  #number_of_images=length(df_by_category)/NUM_OF_BANDS
  for (m in landsat_numbers){
    bands_selection=c(grep(paste0("B",m), names(df_by_category), value=TRUE, fixed
        = FALSE)) #takes names with that band (ex. B1) from the rasters list
    column_band=df_by_category[,bands_selection] #creates new df from the first df
        with columns whose name corresponds to bands_selection
    column_band_list[[m]]=as.vector(as.matrix(column_band)) #this creates one singl
        e column from the many-columns df just created
    column_band_df=as.data.frame(column_band_list)
  }
  names(column_band_df)=band_name_list
  return(column_band_df)
}
```

```
terrain_bb = create_df_byband(raster_df_terrain)
veget_bb = create_df_byband(raster_df_veget)
water_bb = create_df_byband(raster_df_water)


#+++++++++++++++++++++++++#
#    Gram-Schmit process    #
#+++++++++++++++++++++++++#


# 1. ---- CALCULATING 'IDEAL terrain POINTS' IN EACH BAND
vec_vec=c()
for (i in 1:NUM_OF_BANDS){
  next_vec=c()
  for (j in 1:NUM_OF_BANDS)
  {
    if (j != i)
      {
      next_vec=c(next_vec,j)
    }
  }
  vec_vec=c(vec_vec,next_vec)
}
vec_vec

vec_b1=c(2,3,4,5,6,7)
vec_b2=c(1,3,4,5,6,7)
vec_b3=c(1,2,4,5,6,7)
vec_b4=c(1,2,3,5,6,7)
vec_b5=c(1,2,3,4,6,7)
vec_b6=c(1,2,3,4,5,7)
vec_b7=c(1,2,3,4,5,6)

ideal_points_func <- function(coeff_selection, coeff_list, old_value_by_band) {
  calculated_value_by_band = c()
  old_value_selected = c()
  coefficient = coeff_list[[1]]
  new_coeff_list <- coeff_list[-1]
  for (i in coeff_selection){
    old_value_selected = c(old_value_selected, old_value_by_band[i])
  }
  print(old_value_selected)
  for (i in 1:6) {
      calculated_value_by_band=c(calculated_value_by_band, new_coeff_list[[i]]*old_
          value_selected[i])
      print(calculated_value_by_band)
      }
  calculated_value = sum(calculated_value_by_band)+coefficient
  return(calculated_value)
}


value_bb_bright <- function(dataframe_bb) { #NB: bands_vector written as c()
```

```
  value_bb = c()
  for (band in 1:length(dataframe_bb)) {
    value=max(as.matrix(dataframe_bb[band]))
    value_bb = c(value_bb,value)
  }
  return(value_bb)
}


value_bb_dark <- function(dataframe_bb) { #NB: bands_vector written as c()
  value_bb = c()
  for (band in 1:length(dataframe_bb)) {
    print(band)
    value=min(as.matrix(dataframe_bb[band]))
    print(value)
    value_bb = c(value_bb,value)
  }
  return(value_bb)
}

value_by_band_b = value_bb_bright(terrain_bb)
value_by_band_d = value_bb_dark(terrain_bb)

for (i in 1:NUM_OF_BANDS){
  next_vec=c()
  for (j in 1:NUM_OF_BANDS)
  {
    if (j != i)
    {
      next_vec=c(next_vec,j)
    }
  }
}

# BAND1:
model_band1_s = lm(Band1 ~ Band2 + Band3 + Band4 + Band5 + Band6 + Band7, data=terr
    ain_bb)
coeff_B1=model_band1_s$coefficients
coeff_B1
prova = coeff_B1[-1]
prova
#calculating the bright point
Xb_band1 = ideal_points_func(vec_b1, coeff_B1, value_by_band_b)
Xb_band1
##calculating the dark point
Xd_band1 = ideal_points_func(vec_b1, coeff_B1, value_by_band_d)
Xd_band1

#.... This to be repeated for each band (omitted here)
```

```
# 2. - - - CALCULATING THE COEFFICIENTS FOR THE 1ST INDEX (Brightness)
norm_vec <- function(x) sqrt(sum(x^2))

Xb = c(Xb_band1, Xb_band2, Xb_band3, Xb_band4, Xb_band5, Xb_band6, Xb_band7)
Xd = c(Xd_band1, Xd_band2, Xd_band3, Xd_band4, Xd_band5, Xd_band6, Xd_band7)
b = Xb-Xd
B = norm_vec(b)
A1 = b/B
A1


# 3. - - - PREPARING THE DATA FOR THE 2nd INDEX (Greenness)
Xs_band1 = mean(as.matrix(terrain_bb[1]))
Xs_band2 = mean(as.matrix(terrain_bb[2]))
Xs_band3 = mean(as.matrix(terrain_bb[3]))
Xs_band4 = mean(as.matrix(terrain_bb[4]))
Xs_band5 = mean(as.matrix(terrain_bb[5]))
Xs_band6 = mean(as.matrix(terrain_bb[6]))
Xs_band7 = mean(as.matrix(terrain_bb[7]))
Xs = c(Xs_band1, Xs_band2, Xs_band3, Xs_band4, Xs_band5, Xs_band6, Xs_band7)

value_bb_green <- function(dataframe_bb) { #NB: bands_vector written as c()
  value_bb = c()
  for (band in 1:length(dataframe_bb)) {
    value=mean(as.matrix(dataframe_bb[band])) #taking average of the vegetated pixe
        ls values
    value_bb = c(value_bb,value)
  }
  return(value_bb)
}

value_by_band_g = value_bb_green(veget_bb)

# BAND1:
model_band1_g = lm(Band1 ~ Band2 + Band3 + Band4 + Band5 + Band6 + Band7, data=vege
    t_bb)
#model_band1
#plot(model_band1)
coeff_B1=model_band1_g$coefficients
#calculating the green point
Xg_band1 = ideal_points_func(vec_b1, coeff_B1, value_by_band_g)
Xg_band1

#.... This to be repeated for each band (omitted here)

Xg = c(Xg_band1, Xg_band2, Xg_band3, Xg_band4, Xg_band5, Xg_band6, Xg_band7)

# 4. - - - CALCULATING THE COEFFICIENTS FOR THE 2nd INDEX (Greenness)

inner_prod <- function(x,y) (sum(x*y))
```

```
g = ( Xg-Xs ) - inner_prod( (Xg-Xs), A1) * A1
G = norm_vec(g)
A2 = g/G
A2


# 5. - - - PREPARING THE DATA FOR THE 3rd INDEX

value_bb_wet <- function(dataframe_bb) { #NB: bands_vector written as c()
  value_bb = c()
  for (band in 1:length(dataframe_bb)) {
    value=mean(as.matrix(dataframe_bb[band])) #taking average of the vegetated pixe
        ls values
    value_bb = c(value_bb,value)
  }
  return(value_bb)
}


value_by_band_w = value_bb_wet(water_bb)


# BAND1:
model_band1_w = lm(Band1 ~ Band2 + Band3 + Band4 + Band5 + Band6 + Band7, data=wate
    r_bb)
#model_band1
#plot(model_band1)
coeff_B1=model_band1_w$coefficients
#calculating the wet point
Xw_band1 = ideal_points_func(vec_b1, coeff_B1, value_by_band_w)
Xw_band1

#.... This to be repeated for each band (omitted here)

Xw = c(Xw_band1, Xw_band2, Xw_band3, Xw_band4, Xw_band5, Xw_band6, Xw_band7)


# 6. - - - CALCULATING THE COEFFICIENTS FOR THE 3rd INDEX (Wetness)

y = ( Xw-Xs ) - inner_prod( (Xw-Xs), A1) * A1 - inner_prod( (Xw-Xs), A2) * A2
Y = norm_vec(y)
A3 = y/Y
A3


# creating matrix with all coefficients together (a table)
coefficients=rbind(A1,A2,A3)
rownames(coefficients) = c('Brightness', 'Greenness', 'Wetness')
colnames(coefficients) = band_name_list
coefficients
```

Bibliography

Al-Bakri, J., Salahat, M., Suleiman, A., Suifan, M., Hamdan, M., Khresat, S., and Kandakji, T. (2013). Impact of Climate and Land Use Changes on Water and Food Security in Jordan: Implications for Transcending "The Tragedy of the Commons". *Sustainability*, 5(2):724–748.

Al Eisawi, D. M. H. (2005). Water Scarcity in Relation To Food Security and Sustainable Use of Biodiversity in Jordan. 65(November):239–248.

Al-Kharabsheh, A. (2000). Ground-water modelling and long-term management of the Azraq basin as an example of arid area conditions (Jordan). *Journal of Arid Environments*, 44(2):143–153.

Albalawi, E. K. and Kumar, L. (2013). Using remote sensing technology to detect, model and map desertification: A review. *Journal of Food, Agriculture and Environment*, 11(2):791–797.

Allan, J. A. (2002). *The Middle East Water Question: Hydropolitics and the Global Economy*. I.B. Tauris, London - New York.

Allan, J. A. (2003). Useful Concept or Misleading Metaphor ? Virtual Water : A Definition. *Water International*, 28(1):4–11.

Allen, T. R. and Kupfer, J. a. (2000). Application of spherical statistics to change vector analysis of landsat data: Southern appalachian spruce - Fir forests. *Remote Sensing of Environment*, 74(3):482–493.

Alvarez Cobelas, M., Rojo, C., and Angeler, D. G. (2005). Mediterranean limnology: Current status, gaps and the future. *Journal of Limnology*, 64(1):13–29.

Baig, M. H. A., Zhang, L., Shuai, T., and Tong, Q. (2014). Derivation of a tasselled cap transformation based on Landsat 8 at-satellite reflectance. *Remote Sensing Letters*, 5(5):423–431.

Bajjali, W. and Al-Hadidi, K. (2005). Hydrochemical Evaluation of Groundwater in Azraq Basin, Jordan Using Environmental Isotopes and GIS Techniques. *Proceeding of the 25th Annual ESRI International User Conference San Diego California July 2529 2005*, pages 1–19.

Barreda-bautista, B. D., López-caloca, A. A., Investigación, D., Ing, G., and Tamayo, J. L. (2011). Tropical Dry Forests in the Global Picture : The Challenge of Remote Sensing-Based Change Detection in Tropical Dry Environments. In Carayannis, E., editor, *Planet Earth 2011 - Global Warming Challenges and Opportunities for Policy and Practice*, chapter 11, pages 231–256. InTech.

Bashir, M. and Csaplovics, E. (2011). Appling Change Vector Analysis to Detect Vegetation Regeneration and Deforestation in Edd Al Fursan locality, South Darfur, Sudan. In Sunny, Schwarze, and Brummer, editors, *Conference on International Research on Food Security, Natural Resource Management and Rural Development*, Tropentag. University of Bonn.

Bayarjargal, Y., Karnieli, A., Bayasgalan, M., Khudulmur, S., Gandush, C., and Tucker, C. (2006). A comparative study of NOAA-AVHRR derived drought indices using change vector analysis. *Remote Sensing of Environment*, 105(1):9–22.

Beaumont, P. (1978). The Euphrates River—an International Problem of Water Resources Development. *Environmental Conservation*, 5(1):35.

Beaumont, P. (1996). Agricultural and environmental changes in the upper Euphrates catchment of Turkey and Syria and their political and economic implications. *Applied Geography*, 16(2):137–157.

Beaumont, P. (1998). Restructuring of water usage in the Tigris-Euphrates Basin: The impact of modern water management policies. *Coppock, J. and Miller, JA Transformation of Middle Eastern natural environments: Legacies and lessons*, 113:168–186.

Blaschke, T. (2010). Object based image analysis for remote sensing. *ISPRS Journal of Photogrammetry and Remote Sensing*, 65:2–16.

Bovolo, F. and Bruzzone, L. (2006). A novel theoretical framework for unsupervised change detection based on CVA in polar domain. *International Geoscience and Remote Sensing Symposium (IGARSS)*, 45(1):379–382.

Bovolo, F., Marchesi, S., and Bruzzone, L. (2012). A framework for automatic and unsupervised detection of multiple changes in Multitemporal Images. *IEEE Transactions on Geoscience and Remote Sensing*, 50(6):2196–2212.

Brooks, D. B. (2007). Fresh Water in the Middle East and NorthAfrica, Source of Conflict/Base for Cooperation. In Lipchin, C., Pallant, E., Saranga, D., and Amster, A., editors, *Integrated Water Resources Management and Security in the Middle East*, chapter 1, pages 33–64. Springer.

Bruzzone, L. and Prieto, D. F. (2000). Automatic Analysis of the Difference Image for Unsupervised Change Detection. *IEEE Geoscience and Remote Sensing*, 38(3):1171–1182.

Canty, M. J. (2014). *Image Analysis, Classification and Change Detection in Remote Sensing*. CRC Press, Taylor & Francis Group, third edition.

Canty, M. J. and Nielsen, A. A. (2006). Visualization and unsupervised classification of changes in multispectral satellite imagery. *International Journal of Remote Sensing*, 27(18):3961–3975.

Chander, G. and Markham, B. (2003). Revised Landsat-5 TM Radiometric Calibration Procedures and Postcalibration Dynamic Ranges. *IEEE Transactions on Geoscience and Remote Sensing*, 41(11):2674–2677.

Chang, Y. (1992). Developing Tasselled Cap Transformation for SPOT HRV Reflectance Data. *ISPRS Archive*, XXIX(B7):457–456.

Chen, J., Gong, P., He, C., Pu, R., and Shi, P. (2003). Land-Use/Land-Cover Change Detection Using Improved Change-Vector Analysis. *Photogrammetric Engineering & Remote Sensing*, 69(4):369–379.

Chen, Y.-h., Li, X.-b., Shi, P.-j., and Xie, F. (2001). The Change of NDVI Time Series Based on Change Vector Analysis in China. In *Info-tech and Info-net, 2001. Proceedings. ICII 2001 2001*, pages 127–132, Beijing. IEEE Xplore.

Collins, J. B. and Woodcock, C. E. (1994). Change detection using the Gramm-Schmidt transformation applied to mapping forest mortality. *Remote Sensing of Environment*, 50(December 1993):267–279.

Coppin, P., Lambin, E. F., Jonckheere, I., and Muys, B. (2004). Digital change detection methods in natural ecosystem monitoring: a review. *International Journal of Remote Sensing*, 25(9):1565–1596.

Cordova, C. E., Nowell, A., Bisson, M., Ames, C. J. H., Pokines, J., Chang, M., and Al-Nahar, M. (2013). Interglacial and glacial desert refugia and the Middle Paleolithic of the Azraq Oasis, Jordan. *Quaternary International*, 300:94–110.

Crist, E. and Cicone, R. (1984). A Physically-Based Transformation of Thematic Mapper Data - The TM Tasseled Cap. *IEEE Transactions on Geoscience and Remote Sensing*, GE-22(3):256–263.

Crist, E. and Kauth, R. (1986). The Tasseled Cap De-Mystified. *American Society for Photogrammetry and Remote Sensing*, 52(1):81–86.

Crist, E. P. (1985). A TM Tasseled Cap equivalent transformation for reflectance factor data. *Remote Sensing of Environment*, 17:301–306.

Davis, K. L. (2015). *The Expanding Nature of the Syrian Civil War: from Poor Policy to Regional Conflict (Unpublished Masters Thesis)*. PhD thesis, John Hopkins University, Baltimore, Maryland.

Dawelbait, M. A. A. and Morari, F. (2011). LANDSAT , Spectral Mixture Analysis and Change Vector Analysis to Monitor Land Cover Degradation in a Savanna Region in Sudan (1987-1999-2008). *International Journal of Water Resources and Arid Environments*, 1(5):366–377.

De Châtel, F. (2014a). The Role of Drought and Climate Change in the Syrian Uprising: Untangling the Triggers of the Revolution. *Middle Eastern Studies*, 50(4):521–535.

De Châtel, F. (2014b). *Vanishing Water Landscapes in the Middle East: Public Perceptions, Political Narratives and Traditional Beliefs Surrounding Water and Scarcity in an Arid Region*. PhD thesis, Radbouf University Nijmegen.

Demilecamps, C. (2010). *Farming In The Desert, Analysis of the agricultural situation in Azraq Basin. German-Jordanian Programme "Management of Water Resources"*. Deutsche Gesellschaft für Internationale Zusammenarbeit (GIZ) GmbH, Amman, Jordan.

Dottridge, J. and Abu Jaber, N. (1999). Groundwater resources and quality in northeastern Jordan; safe yield and sustainability. *Applied Geography*, 19:313–323.

Dubovyk, O., Menz, G., Conrad, C., Thonfeld, F., and Khamzina, A. (2013). Object-based identification of vegetation cover decline in irrigated agro-ecosystems in Uzbekistan. *Quaternary International*, 311:163–174.

Eastman, J. R. (1992). Change and time series analysis techniques: a review. pages 1–28.

Edwards, M. C., Wellens, J., and Al-Eisawi, D. (1999). Monitoring the grazing resources of the Badia region, Jordan, using remote sensing. *Applied Geography*, 19(4):385–398.

El-Naqa, A., Al-Momani, M., Kilani, S., and Hammouri, N. (2007). Groundwater deterioration of shallow groundwater aquifers due to overexploitation in northeast Jordan. *Clean-Soil Air Water*, 35(2):156–166.

FAO (2012). Joint Rapid Food Security Needs Assessment (JRFSNA) - Syrian Arab Republic, Report. (June):26.

Flores, S. E. and Yool, S. R. (2007). Sensitivity of change vector analysis to land cover change in an arid ecosystem. *International Journal of Remote Sensing*, 28(5):1069–1088.

Glantz, M. H. and Orlovsky, N. S. (1983). Desertification: a review of the concept. *Desertification Control Bulletin*, 9:15–22.

Gleick, P. H. (2014). Water, Drought, Climate Change, and Conflict in Syria. *Weather, Climate, and Society*, 6(3):331–340.

Goode, D. J., Senior, L. A., Subah, A., and Jaber, A. (2013). Groundwater-level trends and forecasts, and salinity trends, in the Azraq, Dead Sea, Hammad, Jordan Side Valleys, Yarmouk, and Zarqa groundwater basins, Jordan. Technical report, U.S. Geological Survey Open-File Report 2013-1061.

Green, J. (1995). Groundwater abstraction and plankton in the Druze pool of Azraq oasis, Jordan. *Freshwater Forum*, 5(3):157–160.

He, C., Zhao, Y., Tian, J., Shi, P., and Huang, Q. (2013). Improving change vector analysis by cross-correlogram spectral matching for accurate detection of land-cover conversion. *International Journal of Remote Sensing*, 34(4):1127–1145.

Higginbottom, T. P. and Symeonakis, E. (2014). Assessing land degradation and desertification using vegetation index data: Current frameworks and future directions. *Remote Sensing*, 6(10):9552–9575.

Hole, F. (2009). Drivers of unsustainable land use in the Semi-Arid Khabur River Basin, Syria. *Geographical Research*, 47(1):4–14.

Hole, F. and Smith, R. (2004). Arid land agriculture in Northeastern Syria, Will this be a tragedy of the commons? In Gutman, G., editor, *Land Change Science, Remote Sensing and Digital Image Processing 6*, pages 209–222. Springer Science+Business Media B.V.

Hole, F. and Zaitchik, B. F. (2007). Policies, plans, practice, and prospects: Irrigation in northeastern Syria. *Land Degradation and Development*, 18(2):133–152.

Hotelling, H. (1936). Relations Between Two Sets of Variates. 28(3/4):321–377.

Huang, C., Wylie, B., Yang, L., Homer, C., and Zylstra, G. (2002a). Derivation of a tasselled cap transformation based on Landsat 7 at-satellite reflectance. *International Journal of Remote Sensing*, 23(8):1741–1748.

Huang, C., Yang, L., Homer, C., Wylie, B., Vogelman, J., and De Felice, T. (2002b). At-satellite reflectance: a first order normalization of landsat 7 etm+ images. *US Department of Interior, USGS*.

Huete, A., Jackson, R., and Post, D. (1985). Spectral response of a plant canopy with different soil backgrounds. *Remote Sensing of Environment*, 17(1):37–53.

IUCN (2010). Azraq Oasis Restoration Project, Final Report - Study of salt fresh water intrusion in Azraq Basin, Jordan. Technical report.

Ivits, E., Lamb, A., Langar, F., Hemphill, S., and Koch, B. (2008). Orthogonal Transformation of Segmented SPOTGeographical Dependence of the Tasselled Cap Parameters. *Photogrammetric Engineering & Remote Sensing*, 74(11):1351–1364.

Jackson, R. (1983). Spectral indices in N-Space. *Remote Sensing of Environment*, 13(5):409–421.

Johnson, R. D. and Kasischke, E. S. (1998). Change vector analysis: A technique for the multispectral monitoring of land cover and condition. *International Journal of Remote Sensing*, 19(3):411–426.

Karnieli, A. and Dall'Olmo, G. (2003). Remote-sensing monitoring of desertification, phenology, and droughts. *Management of Environmental Quality: An International Journal*, 14(1):22–38.

Karnieli, A., Qin, Z., Wu, B., Panov, N., and Yan, F. (2014). Spatio-Temporal Dynamics of Land-Use and Land-Cover in the Mu Us Sandy Land, China, Using the Change Vector Analysis Technique. *Remote Sensing*, 6(10):9316–9339.

Kauth, R. and Thomas, G. (1976). The Tasselled Cap – A Graphic Description of the Spectral-Temporal Development of Agricultural Crops as Seen by Landsat. *LARS Symposia*.

Kelley, C. P., Mohtadi, S., Cane, M. A., Seager, R., and Kushnir, Y. (2015). Climate change in the Fertile Crescent and implications of the recent Syrian drought. *Proceedings of the National Academy of Sciences*, 112(11):3241–3246.

Kuzera, K., Rogan, J., and Eastman, J. (2005). Monitoring vegetation regeneration and deforestation using change vector analysis: Mt. St. Helens study area. *the Annual Conference Baltimore, ...*

Lambin, E. and a.H. Strahler (1994). Indicators of land-cover change for change-vector analysis in multitemporal space at coarse spatial scales. *International Journal of Remote Sensing*, 15(10):2099–2119.

Lambin, E. F. and Strahlers, A. H. (1994). Change-vector analysis in multitemporal space: A tool to detect and categorize land-cover change processes using high temporal-resolution satellite data. *Remote Sensing of Environment*, 48(2):231–244.

Lin, M. L., Chu, C. M., and Tsai, B. W. (2011). Drought risk assessment in western inner-mongolia. *International Journal of Environmental Research*, 5(1):139–148.

Liu, Q., Liu, G., Huang, C., and Xie, C. (2015). Comparison of tasselled cap transformations based on the selective bands of Landsat 8 OLI TOA reflectance images. *International Journal of Remote Sensing*, 36(2):417–441.

Lorena, R. B., dos Santos, J. R., Shimabukuro, Y. E., Brown, I. F., and Kux, H. J. H. (2002). A change vector analysis technique to monitor land use/land cover in sw brazilian amazon: acre state. *ISPRS Archives*, XXXIV(1):8.

Lu, D., Mausel, P., Brondizio, E., and Moran, E. (2004). Change detection techniques. *International Journal of Remote Sensing*, 25(12):2365–2407.

Malila, W. and Lafayette, W. (1980). Change Vector Analysis: An Approach for Detecting Forest Changes with Landsat. pages 326–335.

Markham, B. and Barker, J. (1986). Landsat mss and tm post-calibration dynamic ranges, exoatmospheric rflectances and at-satellite temperatures. *EOSAT Technical Notes*.

Mather, P. (2004). *Computer Processing of Remotely-Sensed Images - An Introduction*. Wiley.

Mc Nab, A.L., Karl, T.R. (1991). Climate and Droughts. In *National Water Summary 1988-89– Hydrologic Events and Floods and Droughts*. U.S. Geological Survey Water-Supply Paper.

Mesnil, A. and Habjoka, N. (2012). *The Azraq Dilemma, Past, Presnt and Future Groundwater Management. German-Jordanian Programme "Management of Water Resources"*. Deutsche Gesellschaft für Internationale Zusammenarbeit (GIZ) GmbH, Amman, Jordan.

Metternicht, G. I. and Zinck, J. A. (2003). Remote sensing of soil salinity: Potentials and constraints. *Remote Sensing of Environment*, 85(1):1–20.

Morales-Salinas, L. and Santibanez, F. (1998). I . Chapter 7 Monitoring Desertification Using Remote Sensing Techniques. In *Computer Tools for Sustainable Management of Arid and Antarctic Ecosystem*, chapter 7. IBM/ERP Program - Universidad de Chile.

Mouat, D., Lancaster, J., Wade, T., Wickham, J., Fox, C., Kepner, W., and Ball, T. (1997). Desertification evaluated using an integrated environmental assessment model. *Environmental Monitoring and Assessment*, 48(2):139–156.

Mountfort, G. (1965). *Portrait of A Desert, The Story of an Expedition to Jordan*. Collins, St James's Palace, London.

MRLC (2001). MRLC 2001 Image Processing Procedure. Multi-Resolution Land Characterization (MRLC) consortium Reports. Revised MAY 22, 2006.

National Research Council (1999). *Water for the Future*. National Academies Press, Washington, D.C.

Nelson, B. (1973). *Azraq Desert Oasis*. Allen Lane - Penguin Books, 21 John Street, London.

Neteler, M., Bowman, M. H., Landa, M., and Metz, M. (2012). GRASS GIS: A multi-purpose open source GIS. *Environmental Modelling and Software*, 31:124–130.

Nguyen, H. (1986). Agricultural Planning Policy and Variability in Syrian Cereal Pro-
duction. In Anderson, J. R. and Hazell, P. B. R., editors, *Variability in Grain Yields*,
chapter 5, pages 78–90. The Johns Hopkins University Press, Baltimore.

Nielsen, A. A., Conradsen, K., and Simpson, J. J. (1998). Multivariate Alteration Detection
(MAD) and MAF Postprocessing in Multispectral , Bitemporal Image Data : New
Approaches to Change Detection Studies. *Remote Sensing of Environment*, 64:1–19.

Nori, W., Elsiddig, E. N., and Niemeyer, I. (2008). DETECTION OF LAND COVER
CHANGES USING MULTI-TEMPORAL SATELLITE. *The International Archives of
the Photogrammetry, Remote Sensing and Spatial Information Sciences*, XXXVII:947–
952.

Nussbaum, S. and Menz, G. (2008). *Object-Based Image Analysis and Treaty Verification,
New Approaches in Remote Sensing - Applied to Nuclear Facilities in Iran*. Springer
Science+Business Media B.V.

Pallant, E. (2007). Introduction. In Lipchin, C., Pallant, E., Saranga, D., and Amster, A.,
editors, *Integrated Water Resources Management and Security in the Middle EastIntro-
duction*. Springer.

Palmer, A. R. and van Rooyen, A. F. (1998). Detecting vegetation change in the southern
Kalahari using Landsat TM data. *Journal of Arid Environments*, 39(2):143–153.

Pannenbecker, A. (2006). Identification of Desertification Indicators Using Bi-Temporal
Change detection. In Braun, M., editor, *Second Workshop of the EARSeL Special Interest
Group on Land Use and Land Cover - Proceedings*, number September, page 121.

Peel, M. C., Finlayson, B. L., and McMahon, T. A. (2007). Updated world map of the
Koppen-Geiger climate classification. *Meteorologische Zeitschrift*, 15:439–473.

Ramsar Convention (1987). RAMSAR Recommendation 3.8: Conservation of Azraq Ram-
sar site, Convention on Wetlands (Ramsar, Iran, 1971) 3rd Meeting of the Conference
of the Contracting Parties. Technical report, Regina, Canada.

Ramsar Convention (1990a). Ramsar Advisory Missions: Report No. 17, Azraq Oasis,
Jordan. Technical report.

Ramsar Convention (1990b). RAMSAR Recommendation 4.9.3: Azraq Oasis, Jordan,
Convention on Wetlands (Ramsar, Iran, 1971), 4th Meeting of the Conference of the
Contracting Parties. Technical report, Montreux, Switzerland.

Ramsar Convention (1998). Ramsar Information Sheet (RIS) on Ramsar Wetlands. Technical report.

Ramsar Convention (1999). Jordan National Report, 7th Meeting of the Conference of the Contracting Parties to the Convention on Wetlands (Ramsar, Iran, 1971). Technical report, San José, Costa Rica.

Sanchez Flores, E. and Yool, S. (2007). Sensitivity of change vector analysis to land cover change in an arid ecosystem. *International Journal of Remote Sensing*, 28(5):1069–1088.

Sardinha, R. M. A. (2008). Dryland Management and Combating Desertification Through Development. *Silva Lusitana*, 16(1):21–44.

Scates, M. D. (1968). Notes on the hydrobiology of Azraq Oasis Jordan. *Hydrobiologia*, 31(1):73–80.

Shafie, H., Seyed, M. H., and Amiri, I. (2012). Assessment of desertification trends in Sistan Plain , Iran using Rs and GIS. *International Journal of Forest, Soil and Erosion*, 2(April 2006):97–100.

Shuval, H. (2007). Virtual Water in the Water Resource Management of the Arid Middle East. In Shuval, H. and Dweik, H., editors, *Water Resources in the Middle East, Israel-Palestinian Water Issues - From Conflict to Cooperation*, chapter 3, pages 133–140. Springer.

Singh, A. (1989). Digital change detection techniques using remotely-sensed data. *International Journal of Remote Sensing*, 10(6):989–1003.

Singh, A., Garg, P. K., and Singh, S. (2012). A Change Vector Analysis technique for monitoring of vegetation regeneration and deforestation: A case tudy of Chiarapur and Shampur range: Haridwar Forest Division. *International Journal of Advanced Scentific and Technical Research*, 4(2):329–341.

Singh, S. and Talwar, R. (2014). A comparative study on change vector analysis. *Sadhana*, 39(December):1311–1331.

Siwe, R. N. and Koch, B. (2008). Change vector analysis to categorise land cover change processes using the tasselled cap as biophysical indicator. *Environmental monitoring and assessment*, 145(1-3):227–35.

Son, T. S., Lan, P. T., and Cu, P. V. (2009). Land Cover Change Analysis Using Change Vector Analysis Method in Duy Tien District , Ha Nam Province in Vietnam Land Cover Change Analysis Using Change Vector Analysis Method in Duy Tien District , Ha Nam Province in Vietnam. *7th FIG Regional Conference Spatial Data Serving People: Land Governance and the Environment - Building the Capacity*, (October 2009):19–22.

Sowers, J., Vengosh, A., and Weinthal, E. (2010). Climate change, water resources, and the politics of adaptation in the Middle East and North Africa. *Climatic Change*, 104:599–627.

Sui, H., Zhou, Q., Gong, J., and Ma, G. (2008). Processing of multitemporal data and change detection. In Chen, L. and Baltsavias, editors, *Advances in Photogrammetry, Remote Sensing and Spatial Information Sciences: 2008 ISPRS Congress Book*, pages 227–247. Taylor & Francis Group, London.

Switzer, P. and Green, A. A. (1984). Min/Max Autocorrelation Factors For Multivariate Spatial Imagery.

UN-ESCWA and BGR (2013). *Inventory of Shared Water Resources in Western Asia*. United Nations Economic and Social Commission for Western Asia; Bundesanstalt für Geowissenschaften und Rohstoffe, Beirut.

UNCCD (1994). United Nations Convention to Combat Desertification in those Countries Experiencing Serious Drought and/or Desertification, Particularly in Africa.

UNCCD (2008). UNCCD Factsheets. Technical report, United Nations Convention to Combat Desertification.

UNESCO (2012). *World Water Development Report Volume 4: Managing Water under Uncertainty and Risk*, volume 1.

UNHCR (2015). 2015 UNHCR country operations profile - Jordan.

UNICEF (2014). Annual Report 2014 Jordan Executive Summary.

Verón, S. R., Paruelo, J. M., and Oesterheld, M. (2006). Assessing desertification. *Journal of Arid Environments*, 66(4):751–763.

WAJ (2007). Water for Life Jordan's Water Strategy 2008-2022.

Weiss, E., Marsh, S. E., and Pfirman, E. S. (2001). Application of NOAA-AVHRR NDVI time-series data to assess changes in Saudi Arabia's rangelands. *International Journal of Remote Sensing*, 22(6):1005–1027.

WHO (2015). Jordan: Water is life.

World Bank (2007). *Making the most of scarcity accountability for better water management in the Middle East and North Africa*, volume 22.

World Bank (2016). *High and Dry - Climate Change, Water, and the Economy*.

Yarbrough, L. D. and Easson, G. (2005). Quickbird 2 tasseled cap transform coefficients: a comparison of derivation methods. *Pecora 16 Symposium 'Global Priorities in Land Remote Sensing'*, (1976).

Yarbrough, L. D., Easson, G., and Kuszmaul, J. S. (2012). Proposed workflow for improved Kauth-Thomas transform derivations. *Remote Sensing of Environment*, 124:810–818.

Zaitchik, B., Smith, R., and Hole, F. (2002). Spatial Analysis of Agricultural Land Use Changes in the Khabour River Basin of Northeastern Syria. volume Volume XXX.

Zanchetta, A., Bitelli, G., and Karnieli, A. (2015). Tasselled Cap transform for change detection in the drylands: findings for SPOT and Landsat satellites with FOSS tools. In Hadjimitsis, D. G., Themistocleous, K., Michaelides, S., and Papadavid, G., editors, *Proc. SPIE 9535, Third International Conference on Remote Sensing and Geoinformation of the Environment (RSCy2015)*.

Zanchetta, A., Bitelli, G., and Karnieli, A. (2016). Monitoring desertification by remote sensing using the Tasselled Cap transform for long-term change detection. *Natural Hazards*, 83:S223–227.

Zhang, L., Liao, M., Yang, L., and Lin, H. (2007). Remote Sensing Change Detection Based on Canonical Correlation Analysis and Contextual Bayes Decision.